FAKULTÄT FÜR MASCHINENWESEN

LEHRSTUHL FÜR AERODYNAMIK UND STRÖMUNGSMECHANIK

Numerical Modeling and Simulation of Cavitation Bubble Cloud with a Lagrangian–Eulerian Approach

Xiuxiu Lyu

Vollständiger Abdruck der von der Fakultät für Maschinenwesen der Technischen Universität München zur Erlangung des akademischen Grades eines

Doktor-Ingenieurs

genehmigten Dissertation.

Vorsitzender:		Prof. Dr.-Ing. Wolfgang Wall
Prüfer der Dissertation:	1.	Priv.-Doz. Dr.-Ing. Xiangyu Hu
	2.	Priv.-Doz. Dr. habil. Chaouki Habchi
	3.	Prof. Dr. Julija Zavadlav

Die Dissertation wurde am 15.07.2019 bei der Technischen Universität München eingereicht und durch die Fakultät für Maschinenwesen am 20.01.2020 angenommen.

Declaration

I hereby declare that except where specific reference is made to the work of others, the content of this dissertation is original and has not been submitted in whole or in part for consideration for any other degree or qualification in this, or any other university. This dissertation is my own work and contains nothing which is the outcome of work done in collaboration with others, except as specified in the text and Acknowledgments.

© **Xiuxiu Lyu** (xiuxiu.lyu@tum.de, lyuxx1989@hotmail.com)

All rights reserved. No part of this publication may be reproduced, modified, re-written, or distributed in any form or by any means, without the prior written permission of the author.

Xiuxiu Lyu

20.01.2020

Abstract

In this thesis, we model and simulate flow cavitation numerically with a Lagrangian–Eulerian (LE) coupling model, emphasizing an investigation of cavitation bubble cloud. This model comprises Eulerian and Lagrangian descriptions of cavitation fluid and dispersed gas/vapor bubbles, respectively, and an LE coupling scheme. While the Eulerian fluid is modeled as a compressible fluid, the cavitation bubbles are modeled with Lagrangian tracking, describing the bubbles' motion and radius dynamics. One- and two-way couplings between the Eulerian frame and the Lagrangian frame are introduced to investigate different problems relevant to flow cavitation. We propose a new scheme for the numerical simulation of homogeneous cavitation nucleation based on LE one-way coupling model. Furthermore, we develop LE two-way coupling model to simulate a cavitation bubble cloud interacting with a pressure wave and bubble cluster Rayleigh collapse.

In one-way coupling, only the bulk liquid's effect on the dispersed bubbles is considered, assuming that the bubbles move passively with the bulk liquid and that their volume is so small that we can ignore how they affect the carrier liquid. Because the cavitating nuclei are in the spatial scale of the micro- or nano-meter during homogeneous nucleation, we assume that one-way coupling is a justified treatment for modeling nucleation. Homogeneous cavitation nucleation occurs in pure liquid when the liquid is extracted due to a rapid pressure drop, which is reached through the underwater shock-bubble interaction in a microchannel. This work's novelty lies in the LE coupling model for numerical simulation of homogeneous cavitation nucleation and the Lagrangian tracking of each nucleus. The two-dimensional axisymmetric Eulerian equations are solved to compute shock-bubble interaction and fluid evolution. Nuclei are treated as dispersed particles, and their dynamics are modeled by the Rayleigh–Plesset (RP) equation. We apply the Poynting corrected nucleation theory (PCNT) to our homogeneous nucleation model, as it offers a more accurate nucleation rate with Poynting correction than classical nucleation theory (CNT) does. The normalized Gaussian kernel function is applied to model the vapor volume fraction, based on the size distribution of the dispersed nuclei. This treatment smooths the void fraction and diffuses the isolated sub-grid interfaces to avoid numerical oscillations.

Nuclei initialization is divided into three steps: bubble location initialization, bubble volume initialization, and state variables initialization. We conclude that homogeneous nucleation inside a microchannel can be separated into three stages: energy deposition stage, nuclei generation stage, and nuclei growth stage. A set of simulations with different initial shock amplitudes is presented to analyze how initial shock amplitude affects nuclei generation time; total nuclei number and nuclei size distribution at different stages and under different shock-amplitudes are also analyzed.

With cavitation bubbles expanding, their influence on the carrier liquid has to be accounted for by two-way coupling. In the second part of this work, the gas-liquid mixture is treated directly as a compressible fluid with pressure equilibrium. Specifically, we will consider an isobaric closure as it has better mathematical properties than an isothermal one. We assume that the bubbles barely influence the mixture's momentum or velocity, due to the large density ratio between liquid and gas. Thus, cavitation bubbles, carrier liquid, and mixture are assumed to share the same local velocity. We also assume that the bubbles' effect on the flow is introduced by variating the mixture density and the pressure field, due to their convection and mixing with the carried liquid. Bubble's compression and expansion are described by a modified RP equation, which considers the close-by flow properties, other than the flow properties at infinity, for each bubble. Several benchmark cases are simulated to validate our model, which we apply further to investigate how the bubble cloud affects the shape and propagation of a pressure wave when the pressure pulse travels through. In the end, we perform three-dimensional (3D) simulation of a vapor cloud's Rayleigh collapse and discuss the extreme pressure it induces in detail. The total bubble number's influence on the extreme collapse pressure and the size distribution of bubbles during the collapse are also analyzed.

Acknowledgements

I would like to express my sincere gratitude to all those who helped me during my Ph.D life.

I gratefully acknowledge Prof. Nikolaus A. Adams and PD Dr. Xiangyu Hu for their guidance and supervision. I thank them for their encouragement and inspiration in our weekly meetings and daily discussions.

My thanks go to Prof. Adams for his funding support for my last year and his revision of my draft paper. Without his patient instruction and expert guidance, the completion of this work would not have been possible.

Thank you to my supervisor, Dr. Hu, who has offered me valuable suggestions for academic study. Xiangyu has always been available for a discussion, which sped up our output a lot. He has extensive experience in numerical methods, and has offered many valuable ideas and insightful criticism. Especially in the last few months of thesis preparation, even I was in China, he still spent time every Tuesday for a discussion, and provided me with inspiring advice.

I also want to thank Dr. Chaouki Habchi and Prof. Julija Zavadlav for joining the examining committee of my thesis. It's a great honor that they could examine my thesis.

Grateful acknowledgment also goes to Prof. Fengming Li, supervisor of my master's thesis, for his consideration during my Ph.D study. Prof. Li has written me emails every several months to follow up on my study and life in Germany. I received a lot of encouragement from his side.

I acknowledge the scholarship from China Scholarship Council under No. 201406120010 and the funding from German Research Foundation (Deutsche Forschungsgemeinschaft) under the Transregio 40 project.

I am very grateful to many colleagues for their companion and cooperation at the institute. I would like to thank:

Angela Grygier, our secretary, who has helped me a lot and cared about my life in Germany.

Julie Piquee, my colleague and also my roommate. Without you, my life would never have been so colorful.

Dr. Lin Fu, for his help on the finite volume implementation and his guidance for doing research.

Yue Li, for her courage.

My officemates, Thomas Kaller and Antonio Di Giovanni, for their daily help and company. Especially, thank Thomas for his help of my draft proofreading and his encouragement.

Dr. Shucheng Pan, for our discussion and cooperation in bubble dynamics.

Massoud Rezavand, Chi Zhang, Jianhang Wang, Zhe Ji, and Yujie Zhu in our team for their support.

Raffaele Olmeda and Theresa Trummler for their care.

I would like to also thank my great friend, Ying Qi, for her company in my life in Munich.

In the end, I would like to express my gratitude to my family. Thank you to my beloved parents, Junlie Lyu and Lizhen Ding, for their unconditional love and encouragement. They have always helped me out of difficulties and supported me without any complaint.

Thank you to my husband, Zhao Li, for your support and love. A four-year long-distance relationship was difficult for both of us. He has always encouraged me every time I felt frustrated and waited for me in China with patience.

Table of contents

Abstract v

Acknowledgement vii

Nomenclature xiii

List of figures xv

1 Introduction 1

- 1.1 Background 1
- 1.2 Numerical simulation of cavitation bubbles 4
  - 1.2.1 Bubble dynamics 5
  - 1.2.2 Numerical models 5
- 1.3 Lagrangian-Eulerian model 7
- 1.4 Contribution and outline 8

2 Physical models 11

- 2.1 Bubble dynamics 11
  - 2.1.1 Rayleigh-Plesset equation 12
  - 2.1.2 Keller-Miksis equation 13
  - 2.1.3 Equation of bubble motion 14
- 2.2 Navier-Stokes equations 15
- 2.3 Equations of state 16
- 2.4 Gas volume fraction 17
- 2.5 Fluid-mixture pressure 19

2.6 Nucleation theory 20

2.6.1 Classical nucleation theory 20

2.6.2 Poynting correction nucleation theory 21

2.7 Summary of Lagrangian-Eulerian coupling model 22

3 Numerical models **23**

3.1 Spatial discretization 23

3.1.1 Finite difference reconstruction 24

3.1.2 Finite volume reconstruction 25

3.1.3 Weighted essentially non-oscillatory scheme 26

3.1.4 HLLC approximate Riemann solver 27

3.2 Time integration 28

3.2.1 Runge-Kutta scheme 28

3.2.2 Variable time-step numerical algorithm 28

3.3 Summary 31

4 Homogeneous cavitation nucleation in a microchannel **33**

4.1 Homogeneous nucleation 34

4.2 Homogeneous nucleation in microchannel 35

4.2.1 Nucleation rate calculation 35

4.2.2 Simulation set-up 35

4.3 Results and discussion 37

4.3.1 Method validation 37

4.3.2 Comparison between CNT and PCNT 39

4.3.3 Shock bubble induced homogeneous nucleation 40

4.3.4 Water pressure at homogeneous nucleation 46

4.3.5 Homogeneous nucleation under different shock amplitudes 49

4.4 Summary 49

5 The Lagrangian-Eulerian two-way coupling model **55**

5.1 Key points of LE model 56
    5.1.1 Volume fraction calculation 56
    5.1.2 Modified bubble dynamics 56
    5.1.3 Finite volume construction 57
    5.1.4 Time integration 57
5.2 Computing procedure 58
5.3 Validation 58
    5.3.1 Isolated bubble 58
    5.3.2 1D bubble advection 60
    5.3.3 Single bubble oscillating 61
5.4 Application of a pressure wave traveling trough a cylindrical bubble cloud 65
5.5 3D Rayleigh collapse of a bubble cloud 71
    5.5.1 Rayleigh collapse 71
    5.5.2 Results and discussions 72
5.6 Summary 75

6 Summary and conclusion **81**

References **85**

Nomenclature

Notation

1D	One-dimensional
2D	Two-dimensional
3D	Three-dimensional
CFD	Computational Fluid Dynamics
CFL	Courant-Friedrich-Lewy
CNT	Classical Nucleation Theory
DNS	Direct Numerical Simulation
ENO	Essentially Non-oscillatory
EOS	Equation of State
FD	Finite Difference
FV	Finite Volume
HLL	Harten-Lax-van Leer
HLLC	Harten-Lax-van Leer-Contact
HIFC	High-intensity Focused Ultrasound
LE	Lagrangian-Eulerian

LES	Large-eddy Simulation
LLF	Local Lax-Friedrichs
MD	Molecular Dynamics
NS	Navier–Stokes
ODE	Ordinary Differential Equation
PCNT	Poynting Corrected Nucleation Theory
PDE	Partial Differential Equation
PDF	Probability Density Function
RANS	Reynolds-averaged Navier–Stokes
Re	Reynolds Number
RK	Runge-Kutta
RP	Rayleigh-Plesset
SL	Sonoluminescence
SPH	Smoothed-particle Hydrodynamics
TVD	Total Variation Diminishing
VOF	Volume of Fluid
WENO	Weighted Essentially Non-oscillatory

List of figures

1.1 (a) Sketch of a cavitating water jet in a nozzle [90]; (b) erosion damages at the top part and the two sides of the injection hole [37, 38]. 2

1.2 Multi-scale phenomena involved in sheet cavitation [48]. 3

1.3 A gas bubble passes through a continuous pressure wave. At a low pressure, the gas bubble expands until an increase in sound-wave pressure results in its collapse, which triggers SL [67]. 4

1.4 Experimental results of the homogeneous nucleation induced from bubble-shock interactions: (a) snapshots of nuclei in a microchannel in Ref. [7]; (b) nucleation bubbles induced from interaction between a pair of bubbles in a microchannel in Ref. [91]. 5

1.5 Schematic of three interface types with respect to the computational grid: fully-resolved, under-resolved, and sub-grid dispersed interfaces. 6

2.1 Schematic of a spherical vapor/gas bubble in an infinite liquid at rest. 12

2.2 Illustration of bubble-fluid interface diffuse area. 18

3.1 Sketch of a cavitating water jet in a nozzle with a cavitating bubble passing through [90]. 30

3.2 Pressure profile along the cavitating nozzle in the test case. 30

3.3 Time change of the bubble radius when the bubble passes passively through the nozzle. 31

4.1 Schematic of the simulation set-up. The laser induced shock interacts with a free surface from distance. To save computational cost, we compute only the 2D-axissymetric computational domain (light-grey region) and interpolate the results into 3D. (*Reprinted with permission from Lyu et al. [70]. Copyright 2018, PHYSICAL REVIEW FLUIDS.*) 37

4.2 Sketch for bubble location initialization. The black circle indicates nucleation region, in which nuclei generate. At the end of each computational time step, we generate $\triangle N_{\text{nuclei}}$ nuclei, shown as red in the right figure. The location is a random selection, the probability of each computation cell is defined based on Eq. (4.4). (*Reprinted with permission from Lyu et al. [70]. Copyright 2018, PHYSICAL REVIEW FLUIDS.*) 38

4.3 Simulation results for the shock front and bubble-fluid interface locations with resolutions of $[256 \times 228]$, $[512 \times 256]$, $[1024 \times 512]$, and experimental results of Ref. [7]. (*Reprinted with permission from Lyu et al. [70]. Copyright 2018, PHYSICAL REVIEW FLUIDS.*) 39

4.4 Nucleation rate for water at room temperature and extreme negative pressure in CNT and PCNT. (a): nucleation rate of pressures from - 55 MPa to -100 MPa, when υ_l/υ_g ratio equals 0.01, 0.012, 0.015, 0.02, 0.05 and 0.1. (b): comparison of nucleation rate of CNT and PCNT with $\upsilon_l/\upsilon_g = 0.012$ and 0.015. (*Reprinted with permission from Lyu et al. [70]. Copyright 2018, PHYSICAL REVIEW FLUIDS.*) 41

4.5 Snapshots of the pressure field at different time instants after shock reflection at the free surface. White color indicates minimum (negative) pressure. (*Reprinted with permission from Lyu et al. [70]. Copyright 2018, PHYSICAL REVIEW FLUIDS.*) . . 42

4.6 Numerical simulation of homogeneous nucleation in comparison with the experimental results (Ando et al. 2012: Ref. [7]). The first line contains the results at 58 ns and the second row the results at 74 ns. Three numerical simulations with υ_l/υ_g being 0.0126, 0.0128, and 0.013 are shown. (*Reprinted with permission from Lyu et al. [70]. Copyright 2018, PHYSICAL REVIEW FLUIDS.*) 43

4.7 Nuclei in the nucleation region at different instances plotted with the background fluid pressure field. 3D vapor bubble distributions at each time instance are shown in the second row, with the color indicating the bulk fluid pressure at the each nucleus location. (*Reprinted with permission from Lyu et al. [70]. Copyright 2018, PHYSICAL REVIEW FLUIDS.*) 45

4.8 (a): Time history of the nuclei number with the indications of the three stages of a general homogeneous nucleation process. (b): Time history of the nuclei number in the shock-bubble interaction case, here, N_{max} is the number of the nuclei formed until the last stage of nucleation. (*Reprinted with permission from Lyu et al. [70]. Copyright 2018, PHYSICAL REVIEW FLUIDS.*) 46

4.9 The nuclei radius distributions and Weibull fits at 64 ns and 76 ns. Here, $R^* = R/R_{\text{mean}}$. At 64 ns, $R_{\text{mean}} = 2.10\mu$m, $\eta = 1.11$ and $\beta = 3.5$, and at 76 ns, $R_{\text{mean}} = 3.74\mu$m, $\eta = 1.06$ and $\beta = 7.3$. (*Reprinted with permission from Lyu et al. [70]. Copyright 2018, PHYSICAL REVIEW FLUIDS.*) 47

4.10 The fitted Weibull distributions for nuclei at different time seconds ranging from 64 ns to 84 ns. (*Reprinted with permission from Lyu et al. [70]. Copyright 2018, PHYSICAL REVIEW FLUIDS.*) 47

4.11 Time evolution of mean radius R_{mean}, scale η and shape β parameters. In general, mean radius and shape parameter increase with time. In reverse, scale parameter decreases with time increasing, but with a small change. (*Reprinted with permission from Lyu et al. [70]. Copyright 2018, PHYSICAL REVIEW FLUIDS.*) 48

4.12 Pressure evolution in the nucleation region along the distance from the gas bubble center at 58 ns, 60 ns, and 62 ns. (*Reprinted with permission from Lyu et al. [70]. Copyright 2018, PHYSICAL REVIEW FLUIDS.*) 48

4.13 Nuclei in the nucleation region at different instances plotted with the background fluid pressure field when the initial shock amplitude is 5.85 GPa. 3D vapor bubble distributions at each time instance are shown in the second row, with the color indicating the bulk fluid pressure at the each nucleus location. 50

4.14 Nuclei in the nucleation region at different instances plotted with the background fluid pressure field when the initial shock amplitude is 6.1 GPa. 3D vapor bubble distributions at each time instance are shown in the second row, with the color indicating the bulk fluid pressure at the each nucleus location. 51

4.15 Maximum of the nuclei number N_{max} increases when initial shock amplitude inside the gas bubble increases from 5.8 GPa to 6.1 GPa. (*Reprinted with permission from Lyu et al. [70]. Copyright 2018, PHYSICAL REVIEW FLUIDS.*) 52

4.16 Time dependencce of the dimensionless parameter $N_{\text{nuclei}}/N_{\text{max}}$ for different shock amplitudes. (*Reprinted with permission from Lyu et al. [70]. Copyright 2018, PHYSICAL REVIEW FLUIDS.*) 52

5.1 Progression of the dimensionless bubble size $R_* = R/R_{b0}$ of 1D simulation. Results of grid resolutions of 100 (dx = 4 R_{b0}) and 200 (dx = 2 R_{b0}) are compared with the analytical solution. 59

5.2 Temporal evolution of the dimensionless bubble size $R_* = R/R_{b0}$ excited by a single pressure wave in 3D simulation. Results of different resolutions ([64 x 32 x 32] and [32 x 16 x 16]) are compared with the analytical solution. 60

5.3 1D advection of the gas-gas interface. The solid line represents the initial fluid condition. At $t = 0.0$, the gas bubble is at the center of the computational domain. ∘: the results when the Lagrangian bubble reaches $x = 2.86$ at $t = 3.0$. 61

5.4 Liquid volume fraction α_l along the bubble radius for different resolutions. 62

5.5 Pressure wave induced from an oscillating gas bubble in the bulk fluid. The pressure field at $t^* = tf = 0.0, 1.0, 3.0$, and 5.0. 63

5.6 Pressure wave propagation induced from a continuous oscillating gas bubble at $t^* = tf = 0.0, 1.0, 3.0$, and 5.0. 64

5.7 Initial setup of the simulation of a pressure wave traveling through a bubble cloud. The radius of the bubble cloud is $A_0 = 2$ mm, and it has 200 bubbles with a random size distribution between 1 μm and 5 μm. The computation domain is $2L \times L$ (L = 10.24 mm). The distribution of the gas bubbles is visualized both by the volume fraction α_g and the Lagrangian spherical particles of the radius R. Four bubbles (bubbles A, B, C, and D), located at the centers of the four boxes, are marked for future reference. 66

5.8 The pressure fields induced by the bubble cluster when the bubble cluster interacts with a sinusoidal pulse. The initial state and the pressure fields at 1.0 μs, 2.5 μs, 3.5 μs, 4.5 μs, and 5.5 μs are shown. 67

5.9 Temporal evolution of the pressure at the bubble cloud center without (the dashed line) and with bubble cloud for two different resolutions. 68

5.10 Plots of α_g when the bubble cluster interacts with a sinusoidal pulse at 1.5 μs, 2.0 μs, 2.5 μs, 3.0 μs, 3.5 μs, and 4.5 μs. 69

5.11 Evolution of bubble radius R of Bubble A - D. 70

5.12 Schematic of setup of the bubble cloud's Rayleigh Collapse. A spherical bubble cloud with N_0 vapor bubbles is submerged; $A(t)$ indicates the bubble cloud's radius. 73

5.13 Snapshots of the collapsing process of a bubble cloud with N_0 = 200 vapor bubbles (at t = 0 μs, 6 μs, 9 μs, 12 μs, 14 μs, and 16 μs). The distribution of the vapor bubbles is visualized both by the iso-surfaces of the volume fraction $\alpha_g = 0.002$ ($\alpha_l = 0.998$) and the Lagrangian spherical particles of the radius R. Cut-sections of the high pressure area (higher than 10 atm) at the center of the bubble cloud are also plotted, which indicate that the cloud's collapse induced violent pressures. 74

5.14 Time change of the non-dimensional active bubble number N_b/N_0 (N_0 = 200) and the average gas fraction β/β_0, here $\beta = \Sigma_{V_c}\alpha_g/V_c$. 75

5.15 Snapshots of the vapor bubble cloud collapse process with N_0 = 300 vapor bubbles (t = 0 μs, 6 μs, 9 μs, 12 μs, 13 μs, and 14 μs). Distribution of the vapor bubbles is visualized both by the iso-surfaces of the volume fraction $\alpha_g = 0.002$ ($\alpha_l = 0.998$) and the Lagrangian spherical particles of the radius R. Cut-sections of the extreme pressure area (higher than 10 atm) at the center of the bubble cloud are also plotted, which indicate the cloud collapse induced violent pressure. 76

5.16 Snapshots of the vapor bubble cloud collapse process initially with N_0 = 400 vapor bubbles (t = 0 μs, 6 μs, 9 μs, 12 μs, 13 μs, and 14 μs). Distribution of the vapor bubbles is visualized both by the iso-surface of the volume fraction $\alpha_g = 0.002$ ($\alpha_l = 0.998$) and the Lagrangian spherical particles of the radius R. Slices of the high pressure area (higher than 10 atm) at the center of the bubble cloud are also plotted, which indicate the cloud collapse induced violent pressure. 77

5.17 Time change of the non-dimensional active bubble number N_b/N_0 (N_0 = 400) and the averaged gas fraction β/β_0 ($\beta = \Sigma_{V_c}\alpha_g/V_c$). 78

5.18 The bubble distributions (radii density bar graphs) of the bubbles' radii at t = 0 μs, 6 μs, 9 μs, 12 μs, 13 μs, and 14 μs. The first bar on the left indicates the density of the collapsed vapor bubbles. 79

Chapter 1

Introduction

1.1 Background

Dispersed flow is defined as the flow where one phase is dispersed in another continuous carrier phase. The dispersed phases are usually solid particles, fluid droplets, or gas bubbles. Typical examples of dispersed flows include solid particles suspended in gas or liquid, atomized droplets in gas, and bubbly flows with dispersed gas or vapor bubbles. Dispersed flows are of major importance for many industrial and medical applications, such as fluid mixing and cleaning, sonochemical processes, and drug- and gene- delivery strategies. The efficiencies of those processes strongly depend on the dispersed phases [14, 23, 25, 79, 102, 111].

In this thesis, we will investigate flow cavitation, with a focus on the dispersed cavitation bubble cloud. *Cavitation*, which is the formation of vapor cavities in liquids, occurs when a liquid is extracted due to a rapid drop in pressure. Cavitation causes damage in many engineering applications, including noise and component damage in devices such as propellers, liquid fuel injectors (Fig. 1.1), and turbines. The collapse of cavitation bubbles is considered as the main event contributing to the destructive influence of cavitation [61, 62, 108]. When a bubble collapses violently, a shock wave will form and destroy the surfaces of nearby equipment. Therefore, cavitation is usually undesirable, and engineering design processes should seek to avoid it. However, cavitation plays a positive role in many medical applications [23, 74, 104, 111]. Cavitation bubble clouds have been investigated in high-intensity focused ultrasound (HIFU) surgery as a means to increase treatment efficiency. In drug

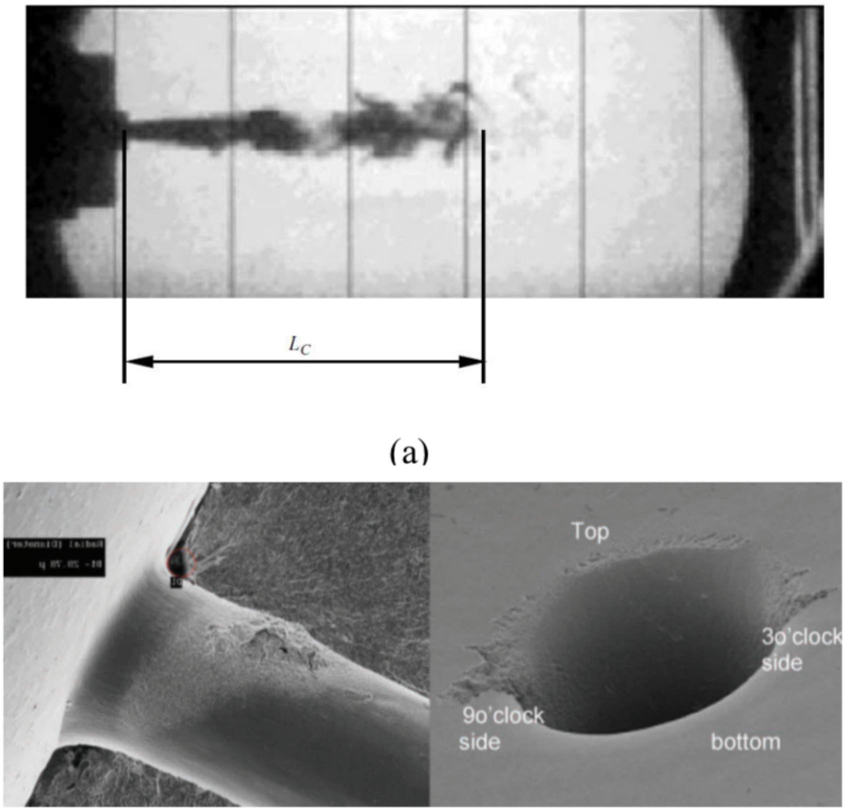

(a)

(b)

Fig. 1.1 (a) Sketch of a cavitating water jet in a nozzle [90]; (b) erosion damages at the top part and the two sides of the injection hole [37, 38].

delivery and gene therapy, microbubbles are introduced as vehicles that can be loaded and traced to a target site and then destroyed or caused to collapse to release a material/drug locally. Additional harm is prevented by keeping the drug from unrelated cells, blood clots, and tumors.

The presence of cavitation bubbles plays a fundamental role in cavitation's applications. In Fig. 1.2, cavitation bubbles with various spatial scales during sheet cavitation are shown. The sizes of different bubbles can vary greatly, ranging from several nanometers to several centimeters. The variety of cavitation bubble spatial scales increases the complexity of cavitation. At the same time, bubbles can convect, change dynamically in size, and collapse. Compared to the single bubble physics the complexity of a bubble cluster is even greater due to the bubble fission/coalescence and bubble-bubble interactions. As a result, difficulty of the numerical modeling and investigation of cavitation bubble cloud is increased.

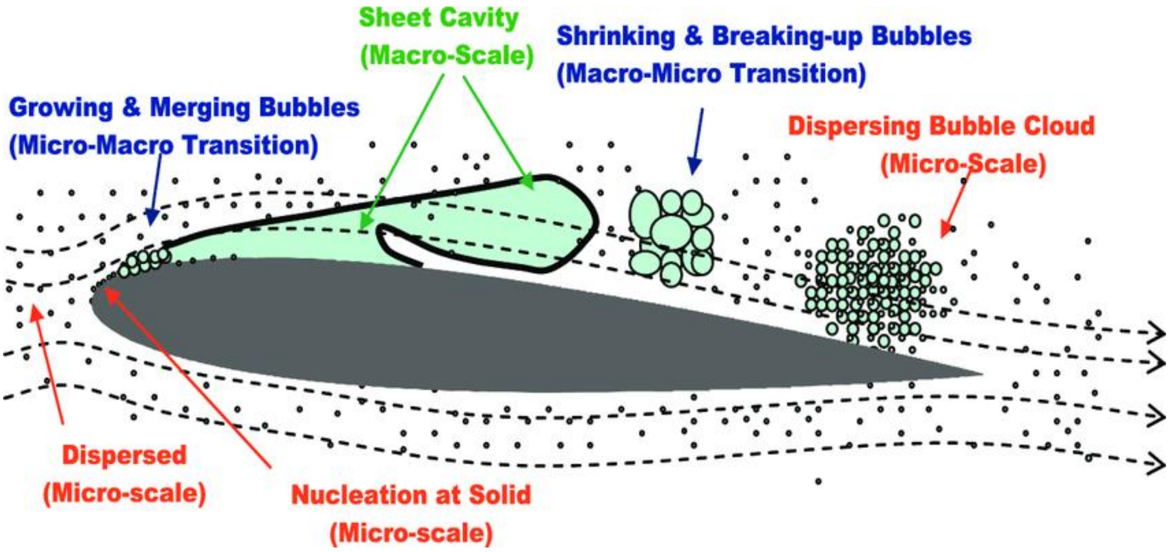
Sheet Cavity
(Macro-Scale)
Shrinking & Breaking-up Bubbles
(Macro-Micro Transition)
Growing & Merging Bubbles
(Micro-Macro Transition)
Dispersing Bubble Cloud
(Micro-Scale)
Dispersed
(Micro-scale)
Nucleation at Solid
(Micro-scale)

Fig. 1.2 Multi-scale phenomena involved in sheet cavitation [48].

Various phenomena related to a single cavitation bubble and bubble cloud have been studied in recent years. One such phenomenon, which occurs with acoustically driven gas bubbles, is light emission resulting from bubble collapse, which is called *sonoluminescence* (SL) [67]. The mechanism of SL induced by bubble oscillation is described in Fig. 1.3. At low pressures, the gas bubble expands dramatically until the increasing sound-wave pressure triggers its collapse. During this collapse, the recombination of electrons and ions results in light emission. *Bubble nucleation* [16, 26], which initializes liquid-to-vapor transitions, can be categorized into heterogeneous and homogeneous nucleation [89]. These differ according to where the nucleation occurs. The former emerges from surfaces in contact with two liquids, and the latter relies on purity in the bulk liquid [57, 60]. Shock-bubble interactions in a microchannel provide an ideal configuration for the formation of homogeneous nucleation. In Fig. 1.4, the experimental results of Ando et al. [7] and Quinto [91] are shown, by which the generation of homogeneous nuclei cloud induced by bubble-shock interactions in a microchannel was successfully photographed. In the studies of cavitation bubble clouds, the distribution of bubble sizes is a research focus [13, 64]. Hauptmann [45] studied the experimentally determined distributions of bubble sizes under pulsed ultrasound and determined the main mechanisms affecting the oscillating bubbles. Iida et al. [51] [52] experimentally estimated the sonochemical bubble size distribution and its number density with two different models. According to

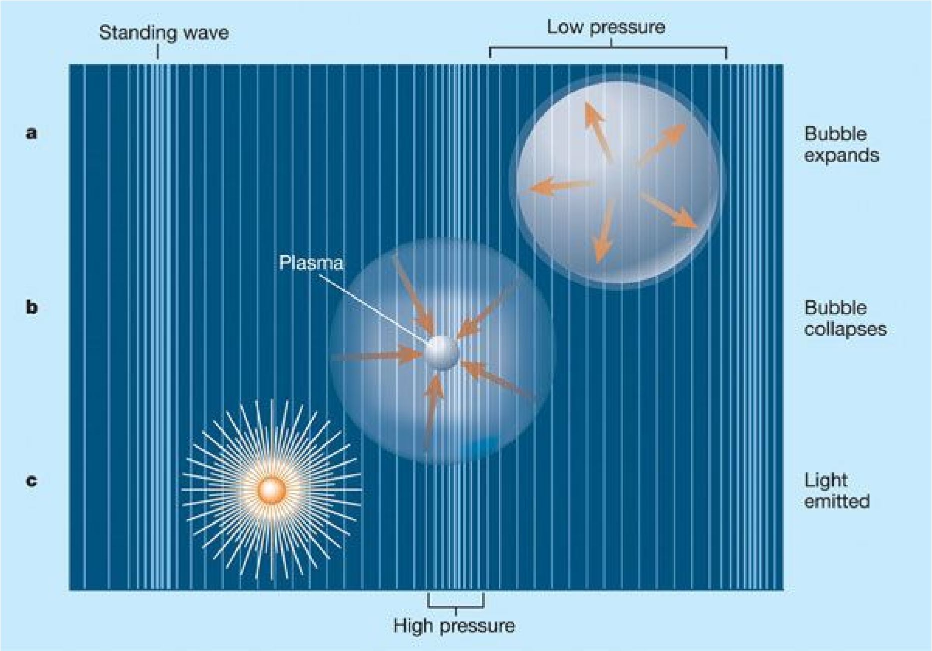

Fig. 1.3 A gas bubble passes through a continuous pressure wave. At a low pressure, the gas bubble expands until an increase in sound-wave pressure results in its collapse, which triggers SL [67].

their results, the size distribution can be well fitted on a graph using a Weibull distribution function. In Ref. [77], the Weibull distribution was also applied to describe the size distribution of small particles.

1.2 Numerical simulation of cavitation bubbles

Over the past decades, computational fluid dynamics (CFD) has become an indispensable tool in the engineering community, where it is widely used. Numerical simulations of fluid flow employ different physical models and offer the transient solution of fluid flow under different time and space scales, which can, in return, assist with experimental and theoretical investigations. Many problems relating to cavitation bubbles have been investigated numerically, such as shock wave propagation in bubbly flows [6, 28], bubbly flow turbulence [19, 31, 69], and bubble clouds in acoustic fields [36, 63]. To better understand the physics of cavitation bubbles, numerical models, which can model the cavitating flow and simultaneously provide the solution for bubble-fluid interfaces, are of great importance [56, 85, 113, 116].

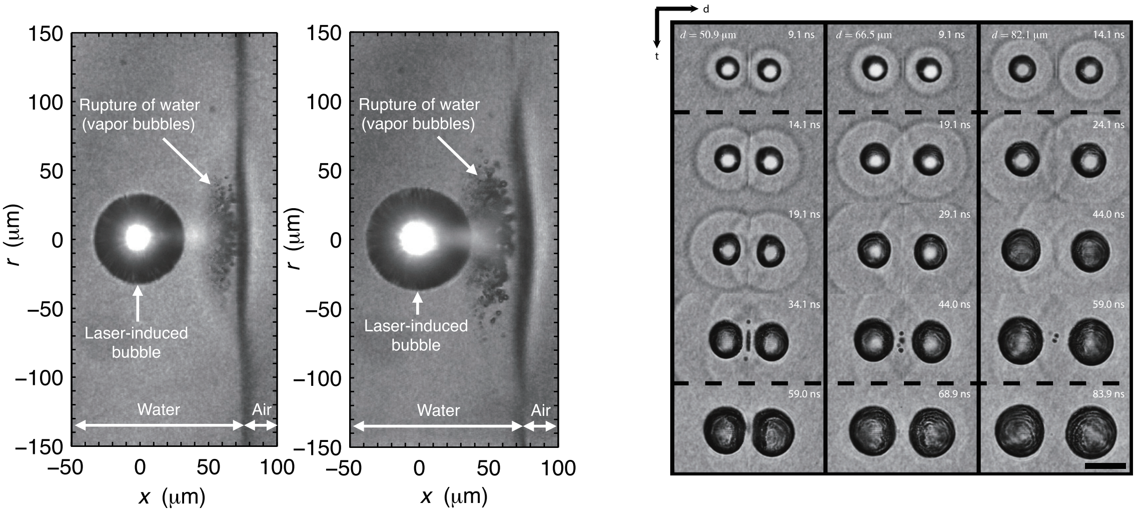
150
100
50
0
−50
−100
−150
r (μm)
Rupture of water (vapor bubbles)
Laser-induced bubble
Water
Air
−50
0
50
100
x (μm)
d
t
d = 50.9 μm
9.1 ns
d = 66.5 μm
9.1 ns
d = 82.1 μm
14.1 ns
14.1 ns
19.1 ns
24.1 ns
19.1 ns
29.1 ns
44.0 ns
34.1 ns
44.0 ns
59.0 ns
59.0 ns
68.9 ns
83.9 ns

(a) (b)

Fig. 1.4 Experimental results of the homogeneous nucleation induced from bubble-shock interactions: (a) snapshots of nuclei in a microchannel in Ref. [7]; (b) nucleation bubbles induced from interaction between a pair of bubbles in a microchannel in Ref. [91].

1.2.1 Bubble dynamics

Many works have been carried out analytically to study the mechanisms of vapor or gas bubbles [17]. The fundamental theoretical study of bubble dynamics was carried out by Rayleigh [93] and Plesset [86], who studied the mechanics and physics of the formation and collapse of a spherical bubble. They presented a comprehensive model describing the time history of a spherical bubble in a weakly compressible liquid. This model considers surface tension and viscous effects but ignores the mass/momentum exchange between gas bubbles and bulk fluid. Afterwards, many researchers extended this model to consider liquid compression [66, 88], mass transfer effects [78], and non-spherical bubble dynamics [62]. However, the classic RP equation remains at the core of analytical models ans is used in a wide range of applications involving hydrodynamic cavitation, acoustic cavitation, multi-phase bubbly flows, and underwater explosion bubbles.

1.2.2 Numerical models

Cavitation bubbles' polydispersity, which ranges from dilute to dense, results in a wide variety of gas volume fractions in computational grids, ranging from 10^{-10} to 10^{-1}. In general, gas-liquid

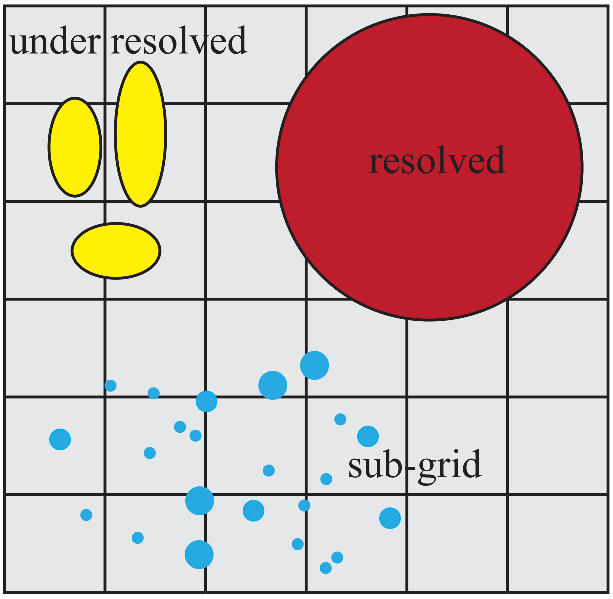

Fig. 1.5 Schematic of three interface types with respect to the computational grid: fully-resolved, under-resolved, and sub-grid dispersed interfaces.

interfaces can be separated into fully solved (resolved), under-resolved, and sub-grid interfaces with respect to grid size. A schematic of the three different interface types is plotted in Fig. 1.5. Different numerical models have been developed to track or resolve different gas-liquid interfaces. In this and next sections, we introduce three models which have been widely used to compute gas-liquid interfaces: the continuum model, the interface tracking model, and the LE model.

The continuum model solves Navier-Stokes (NS) equations for the fluid mixture in an Eulerian frame [4, 47, 81, 96]. Cavitation bubbles are represented by the gas volume fraction or the gas mass fraction in the Eulerian grids, which is derived based on the expression of mixture pressure or density in the equations of state (EOSs). This model is quite popular for Eulerian frame with lower gas volume fractions and weak bubble oscillations, which can ignore single bubble dynamics. A multicomponent flow problem with complex interfaces has been favorably simulated by the continuum model due to its simplicity and numerical stability [47].

To resolve and track the gas-liquid interfaces, interface-tracking models are proposed. Two most popular interface-tracking models are volume of fluid (VOF) method and level-set method. The VOF model solves volume fraction advection equations together with the Eulerian equations [41, 47]. The actual position of the interfaces is recovered at the end of each computational step by an interface reconstruction process. In the level set method introduced by Osher and Sethian [84], the interface is represented as a signed distance function. This approach is more suitable for single bubble simulations, as it treats the bubble and the fluid as two separated phases with a moving non-spherical interface. It is popularly applied with computational sharp-interface multi-phase flows [50, 62]. However, it has the drawback of a high computational cost when the complexity increases to 3D computation.

1.3 Lagrangian-Eulerian model

While there are many different methods of modeling resolved and under-resolved interfaces, such as those in Refs. [4, 47, 50, 62, 81, 96], in this thesis, we apply the LE coupling method to model the sub-grid bubble-fluid interfaces, which has been commonly applied in simulations of dispersed multi-phase flow. The LE model consists of Lagrangian dispersed bubble tracking, an Eulerian description of the carrier fluid, and an LE coupling scheme [24, 29, 105]. This model is favorable due to Lagrangian tracking, simple operation (even in 3D operation), and lower computational costs [24, 29]. Eulerian simulation is based on NS equations, Reynolds-averaged Navier-Stokes (RANS) equations, large eddy simulation (LES) [9, 112], or direct numerical simulation (DNS) [32, 39]. Subgrid bubbles are discretized into Lagrangian particles, which move dynamically according to bubble dynamics and motion equations. The physics of the bubble cloud, governing such aspects as bubble-liquid interactions, bubble-bubble interactions, bubble-wall interactions, and bubble-fluid mass transfers, can be simulated directly in the bubble dynamics equation. Note that the LE model has a higher computational cost when bubble-bubble interactions are taken into account inside bubble dynamics equation [24].

The LE model is widely used in the simulation of spray flow with droplet acceleration, evaporation, collision, coalescence, and breakup. Williams first studied spray droplets based on a Lagrangian description in Ref. [115]. Consequently, Amsden et al. [5] and O'Rourke [82, 83] applied the LE model to simulate spray flow in internal combustion engine applications. The LE model was then further developed to simulate flow cavitation with a focus on cavitation bubble cloud. In Ref. [24], Darmana et al. studied a new parallel algorithm for the LE model and applied it for the numerical simulation of dispersed gas-bubble flow. In Ref. [71], dynamics of a bubble cloud near a rigid wall was studied using a two-phase LE model. Fuster and Colonius [36] proposed a new simulation model for cavitating flow with which they solved volume-averaged Eulerian equations for the carrier liquid alongside Lagrangian tracking for each gas bubble. The motion of the gas bubbles was tracked with the velocity of the bulk fluid. A more accurate expression of bubble dynamics equation was derived based on potential flow theory. Their results showed that their method can capture the pressure disturbance induced in the liquid. Recently, Maeda and Colonius [73] proposed a new formulation for the pressure at infinity in the bubble dynamics equation. They determined the incoming acoustics and the pressure scattered by the bubbles. The resulting fluid pressure at the computational cells is assumed to be a combination of the fluid pressure and the pressure disturbance from each bubble.

LE coupling formulation can be divided into two branches: one-way and two-way coupling. In one-way coupling, only the influence of the carrier phase (the carrier fluid in flow cavitation) on the dispersed phase (cavitation bubbles) is considered (under the assumption that the small bubbles move passively with the carrier fluid and that the dilute gas void fraction is rather small), so we can ignore the influence of the dispersed phase on the carrier phase. Two-way coupling increases the complexity of the nonlinear behavior of the system by considering how the dispersed bubbles influence the carrier fluid. In two-way coupling, the advection of the gas volume fraction and the pressure closure of the gas-liquid mixture are the two main challenges and still open questions.

1.4 Contribution and outline

Most numerical investigations of cavitation focus on topics ranging from erosion due to cavitating flow to the collapse of cavitation bubble cloud; see, e.g., [2, 28, 75]. Numerical studies of homogeneous nucleation are quite scarce, and scholarly understanding of the homogeneous nucleation mechanism is still limited. Inspired by the experimental homogeneous nucleation investigation by Ando et al. [7], we simulate the underwater shock-bubble induced homogeneous nucleation process in a microchannel using the LE one-way coupling scheme. The simulation of bubble-shock interaction is carried out using a compressible multi-phase fluid solver. Dynamics of the dispersed nuclei is modeled in the Lagrangian frame, which describes the motion of each individual nucleus and its size variations driven by the bulk fluid. All nuclei are in the spatial scale of several micro- or nano-meters, so we assume their surface tension is great enough to maintain their spherical form. Bubble dynamics are modeled by the spherical bubble dynamics equation. A new scheme for the 3D simulation of homogeneous nucleation will be proposed by applying PCNT. The novelty of this work lies in the implementation of the LE coupling model for the numerical simulation of homogeneous cavitation nucleation in a microchannel and the Lagrangian tracking of each nucleus.

As the second achievement in this thesis, we develop the LE two-way coupling model by applying an isobaric closure, which is commonly applied in the simulation of multi-component problems. In general, closure laws are classified into two types: isobaric and isothermal. We will apply isobaric law, as it is preferable due to their mathematical properties (which are superior to those of isothermal law), including consistency and hyperbolicity [4]. We solve the cavitation fluid mixture directly in the Eulerian frame. Indeed, unlike EOSs in Refs. [24, 36, 71], which are applied using only bulk liquid pressure, we directly obtain the bubble-fluid mixture equilibrium pressure using the gas volume fraction. Tracking bubble locations and concentrations provides the gas volume fraction, which is modeled based on a normalized truncated Gaussian kernel function. The dispersed bubbles move passively with the bulk fluid, and their dynamics are described by a modified RP equation. The equilibrium pressure will consequently be applied to formulate the nearby flow properties in the modified RP equation, which allows the bubble dynamics to more physically model the fluid surrounding each bubble. After validating the model with several benchmark cases, we apply it to investigate two typical problems within a cavitation bubble cloud: the propagation of a pressure wave and Rayleigh collapse of a vapor bubble cloud.

The thesis is organized as follows:

- In **Chapter 2**, the physical models are reviewed. The governing equations of the LE model will be discussed.

- In **Chapter 3**, the numerical methods of spatial discretization and time integration in the LE coupling model's realization are introduced.

- In **Chapter 4**, we apply the one-way coupling LE method to simulate homogeneous nucleation in a microchannel, as induced by the underwater shock-bubble interaction.

- In **Chapter 5**, we apply the two-way coupling LE model. Some benchmark cases are simulated and investigated to validate our methods. In the end, simulation of a pressure wave passing through a bubble cluster and 3D simulation of Rayleigh collapse of a bubble cloud are performed.
- Conclusion and future work are provided in **Chapter 6**.

Chapter 2

Physical models

In this chapter, physical models considered for the numerical simulation of flow cavitation are introduced. The cavitating liquid is modeled as an Eulerian fluid and aligned with the cavitation bubbles modeled in a Lagrangian frame. Physical quantities of the dispersed bubbles are advanced by the bubble motion and dynamics equations, while the physical quantities of the Eulerian fluid are evolved based on the NS equations.

In the end, the one- and two-way Lagrangian–Eulerian coupling schemes are introduced and will be applied to simulate homogeneous cavitation nucleation in Chapter 4 and cavitation bubble cloud dynamics in Chapter 5, respectively.

2.1 Bubble dynamics

The dispersed bubbles' dynamics are investigated in a Lagrangian frame to dynamically describe the volume and motion of each individual bubble. A microbubble's behavior in an infinite domain of liquid at rest (in Fig.2.1) is modeled under the following assumptions:

- Because dispersed vapor/gas bubbles normally are extremely small (in the scale of nanometers or micrometers), the surface tension is large enough to maintain the bubble's spherical shape.
- Bubble fission and coalescence physics are not considered.
- Each bubble's mass m_b and temperature T_b remain the same.

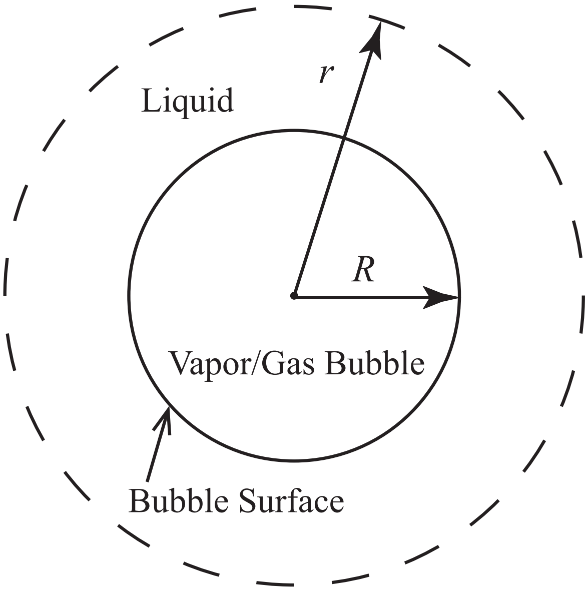

Fig. 2.1 Schematic of a spherical vapor/gas bubble in an infinite liquid at rest.

- The bulk fluid's temperature at infinity T_∞ stays constant.

2.1.1 Rayleigh-Plesset equation

The equation proposed by Rayleigh [93] and Plesset [86] has been widely used for bubble dynamics modeling in hydrodynamic cavitation, multi-phase bubbly flows, and underwater explosion bubbles. Based on the RP equation, dynamics of a spherical bubble surrounded by a weakly compressible liquid at infinite (Fig.2.1) can be expressed as

$$\rho\left[R\ddot{R}+\frac{3}{2}\left(\dot{R}\right)^2\right]=p_B-p_\infty-\frac{2S}{R}-\frac{4\mu}{R}\dot{R}, \tag{2.1}$$

where ρ is the density of the liquid, R is bubble radius, t is time, the dot denotes the substantial time derivative, S is surface tension, μ is viscosity, p_B is the pressure inside the bubble, and p_∞ is the far-field pressure of the surrounding fluid. Generally, a cavitation bubble contains vapor, whose pressure is labeled as p_v, and some quantity of contaminant gas, who has pressure p_{g0} at a reference bubble size R_0. When the temperature T_∞ is constant, p_v is considered constant. Pressure p_B inside the bubble has the following expression:

$$p_B = p_v + p_{g0}\left(\frac{R_0}{R}\right)^{3\kappa_g}, \tag{2.2}$$

where κ_g is approximately constant. $\kappa_g = 1$ models constant bubble temperature, and $\kappa_g = \gamma_g$ models adiabatic behavior, which is normally the ratio of specific heats for gas $\gamma_g = 1.4$.

Besides bubble growth and collapse process, the bubble can oscillate stably when the bubble reaches its equilibrium condition. For the given values of p_B and p_∞, the equilibrium radius R_e can be written as

$$R_e = \frac{2S}{p_B - p_\infty}. \tag{2.3}$$

The bubble under R_e in the liquid without viscous forces will oscillate with a resonance frequency, which is also the natural frequency ω_r of the bubble

$$\omega_r^2 = \frac{1}{\rho R_e^2}\left[3\kappa_g\left(p_\infty - p_B\right) + \frac{2S}{R_e}\left(3\kappa_g - 1\right)\right]. \tag{2.4}$$

2.1.2 Keller-Miksis equation

To model bubble growth and collapse, the Keller–Miksis equation proposed in Ref. [59] has also been widely used. This equation is derived for the large amplitude oscillations of bubble radius. To determine $R(t)$, the second-order, nonlinear ordinary differential equation (ODE) in term of the radius of a single, isolated bubble in an infinite weakly compressible flow is used:

$$\left(R\left(1-\frac{\dot{R}}{c}\right)\right)\ddot{R} + \frac{3}{2}\dot{R}^2\left(1-\frac{\dot{R}}{3c}\right) = \frac{p_n - p_\infty}{\rho}\left(1+\frac{\dot{R}}{c}\right) + \frac{R\dot{p}_n}{\rho c}, \tag{2.5}$$

$$p_n = p_B - \frac{4\mu\dot{R}}{R} - \frac{2S}{R}, \tag{2.6}$$

where p_n is the pressure at bubble-fluid interface and c is the speed of sound in the liquid:

$$c^2 = \frac{dp_l}{d\rho}, \tag{2.7}$$

where p_l is pressure of the carrier fluid.

2.1.3 Equation of bubble motion

The spherical bubbles can move either passively or actively (slip or no-slip) with the carrier fluid. When the bubbles move no-slip with the carrier fluid, there is no relative motion between the two phases; the velocity of each bubble is derived directly from the velocity of the carrier fluid. The position of each bubble $\mathbf{x}_b$ is tracked by

$$\frac{d\mathbf{x}_b}{dt} = \mathbf{u}(\mathbf{x}_b), \tag{2.8}$$

where b is the bubble index and $\mathbf{u}(\mathbf{x}_b)$ is the velocity of the carrier fluid at $\mathbf{x}_b$.

The slip motion also has been accounted for when the bubbles move actively with the carrier fluid. The slip motion equation for spherical microbubbles of a high Reynolds number (Re) was described by Sridhar and Katz [103] for studying spherical bubbles in a laminar vortex. Ford and Loth [34] applied the same equation to study liquid forces acting on bubbles in a turbulent free shear flow and in a turbulent boundary layer [33]. Considering buoyancy, fluid stress, and drag and lift forces, the slip motion equation of a spherical bubble can be written as

$$V_b\left(\rho_b + \frac{1}{2}\rho\right) d\mathbf{u}_b/dt = V_b\left(\rho_b - \rho\right)\mathbf{g} + V_b\rho\left[(1+C_A)D\mathbf{u}/Dt\right] + \mathbf{D} + \mathbf{L} \tag{2.9}$$

where $V_b = \frac{4}{3}\pi R^3$ is the bubble's volume; ρ_b is the bubble's density; $\mathbf{u}_b$ is the bubble velocity; $\mathbf{g}$ is gravitational vector; and C_A is the added mass coefficient [68]. The lift and drag forces can be written as

$$\mathbf{D} = \frac{1}{2}C_D\rho S_B|\left(\mathbf{u}_b - \mathbf{u}\right)|\left(\mathbf{u}_b - \mathbf{u}\right), \tag{2.10}$$

$$\mathbf{L} = \frac{1}{2}C_L\rho S_B|\left(\mathbf{u}_b - \mathbf{u}\right)|^2\left(\left(\mathbf{u}_b - \mathbf{u}\right)\times\omega_l\right)/|\left(\left(\mathbf{u}_b - \mathbf{u}\right)\times\omega_l\right)|, \tag{2.11}$$

where C_D is the quasi-steady drag coefficient, C_L is the quasi-steady lift coefficient, ω_l is the fluid local vorticity, and $S_B = \pi R^2$ is the bubble projected area. Results from Auton et at. in Ref. [12] show that the lift coefficient C_L is proportional to the local vorticity and $\mathbf{L}$ can be written as

$$\mathbf{L} = -\frac{1}{2}\rho V_b\left(\mathbf{u}_b - \mathbf{u}\right) \times \omega_l. \tag{2.12}$$

2.2 Navier-Stokes equations

The carrier fluid's dynamics are modeled in an Eulerian frame, of which the governing equations (i.e. NS equations) can be written as

$$\frac{\partial \rho}{\partial t} + \nabla \cdot (\rho \mathbf{u}) = 0, \tag{2.13}$$

$$\frac{\partial (\rho \mathbf{u})}{\partial t} + \nabla \cdot (\rho \mathbf{u}\mathbf{u} + p\delta) = \nabla \cdot \tau, \tag{2.14}$$

$$\frac{\partial E}{\partial t} + \nabla \cdot (\mathbf{u}(E + p)) = \nabla \cdot (\mathbf{u} \cdot \tau - \dot{q}), \tag{2.15}$$

where p is pressure of the Eulerian fluid, $E = \rho e + \frac{\rho \mathbf{u} \cdot \mathbf{u}}{2}$ is the total energy, $\dot{q} = -k\nabla T$ computes the heat flux, and δ is unit matrix. τ is viscous stress tensor, which follows the Stokes' hypothesis for a Newtonian fluid:

$$\tau = 2\mu \mathbf{S} - \frac{2}{3}\mu(\nabla \cdot \mathbf{u})\delta, \tag{2.16}$$

where $\mathbf{S}$ is the strain rate sensor defined as $\mathbf{S} = \frac{1}{2}(\nabla \mathbf{u} + (\nabla \mathbf{u})^T)$. Without considering the heat transfer and viscous effect, NS equations can be further written under hyperbolic conservation law:

$$\frac{\partial \mathbf{U}}{\partial t} + \nabla \cdot \mathbf{F}(\mathbf{U}) = \mathbf{0}, \tag{2.17}$$

where $\mathbf{U} = (\rho, \rho \mathbf{u}, E)^{\mathrm{T}}$ is vector of the conservative variables. These are comprised of density ρ, momentum $\rho \mathbf{u}$, and total energy $E = \rho e + \frac{\rho \mathbf{u} \cdot \mathbf{u}}{2}$, where ρe is the density times the internal energy for the fluid and $\mathbf{F} = (\rho \mathbf{u}, \rho \mathbf{u}\mathbf{u} + p\delta, \mathbf{u}(E + p))^{\mathrm{T}}$ represents the flux vector.

To save computational cost, an axisymmetric 3D configuration can be modeled by a 2D axisymmetric conservation law, assuming that there is no circumferential variation in the fluid. If the fluid is inviscid and compressible, the axisymmetric governing equation in its conservative form can be written as

$$\frac{\partial \mathbf{U}}{\partial t} + \nabla \cdot \mathbf{F}(\mathbf{U}) = \mathbf{Q}, \tag{2.18}$$

where the state vector $\mathbf{Q}$ represents the source term due to transformation to cylindrical coordinates. For an axisymmetric problem, we assume that the two coordinates are x-axis and z-axis. $\mathbf{U}$, $\mathbf{F}_x$, $\mathbf{F}_z$, and $\mathbf{Q}$ can be written as

$$\mathbf{U} = (\rho, \rho u, \rho w, E)^{\mathrm{T}}, \tag{2.19}$$

$$\mathbf{F}_x = \left(\rho u, \rho u^2 + p, \rho u w, (E+p)u\right)^{\mathrm{T}}, \tag{2.20}$$

$$\mathbf{F}_z = \left(\rho w, \rho u w, \rho w^2 + p, (E+p)w\right)^{\mathrm{T}}, \tag{2.21}$$

$$\mathbf{Q} = \frac{1}{x}\left(-\rho u, -\rho u^2, -\rho u w, (E+p)u\right)^{\mathrm{T}}. \tag{2.22}$$

2.3 Equations of state

To close the system of the Eulerian governing equations, pressure p can be defined by an EOS. This section introduces four widely used EOSs. For weakly compressible fluid, p can be defined as a function of density ρ by

$$p = p_0\left[\left(\frac{\rho}{\rho_0}\right)^{\gamma} - 1\right] + p_b, \tag{2.23}$$

where p_0, ρ_0, and p_b are reference pressure, reference density, and background pressure, respectively.

In Tait's EOS, assuming that the fluid's temperature is constant, p and E are functions of ρ only.

$$p = B\left(\frac{\rho}{\rho_0}\right)^{\gamma} - B + A, \tag{2.24}$$

$$E = \frac{1}{\gamma - 1}(p + B - A) + B - A + \frac{1}{2}\rho \boldsymbol{u}^2. \tag{2.25}$$

where B, A, and ρ_0 are constant parameters. We set $B = 3310$ bar, $A = 1$ bar, $\rho_0 = 10^3$ kg/m^3, and $\gamma_w = 7.15$ for water.

For gas-liquid mixture, the Mie-Gruneisen fluid EOS [94] has been widely applied in the multi-component five-equation model. The Mie-Gruneisen EOS for each fluid reads

$$p_i\left(\rho_i, e_i\right) = p_i^{ref} + \Gamma_i\left(\rho_i\right)\rho_i\left(e_i - e_i^{ref}\right), \tag{2.26}$$

where i equals l for liquid or g for gas and the coefficients $p^{ref} = \rho_0 c_0^2 \eta / \left(1 - s\eta^2\right)^2$, $\eta = 1 - \left(\rho_0/\rho\right)$, $\Gamma\left(\rho\right) = \Gamma_0 \rho_0/\rho$, $e^{ref} = 0.5 p^{ref}\eta/\rho_0$ and ρ_0, c_0, s, and Γ_0 are constant coefficients for each phase.

The stiffened-gas EOS, which is popular for gas-phase modeling, can be written as

$$p_i = \left(\gamma_i - 1\right)\rho_i e_i - \gamma_i B_i, \tag{2.27}$$

involving adiabatic exponent γ and reference pressure B_i for each fluid i. For gas bubbles, we take γ_g = 1.4 and B_g = 1 atm; for carrier water, γ_l = 5.5 and B_l = 492 atm.

2.4 Gas volume fraction

The key function of the LE coupling scheme is the formulation of the gas/vapor volume fraction α_g distribution derived from the size and location of instantaneous bubbles. A mapping function is required to calculate α_g, as it satisfies the criteria: it is a smooth function with a continuous first derivative; it has the absolute maximum value in the computational cell where the bubble center is located; it works only in a finite domain and outside the boundary its value is zero; and integral of the function over the entire domain is unity.

In this study, we apply the concept of kernel function which has been widely used in the smooth particle hydrodynamics (SPH) methodology [49, 76, 106, 107]. The sub-grid interface is allowed to diffuse on the computational cells around the bubble center within a kernel width, as is shown in Fig.2.2. In the limit of a vanishing smoothing length h, the radially symmetric smoothing kernel function W should reduce to a delta function as

$$\lim_{h\to 0} W(\mathbf{x} - \mathbf{x}_b, h) = \delta(\mathbf{x} - \mathbf{x}_b), \tag{2.28}$$

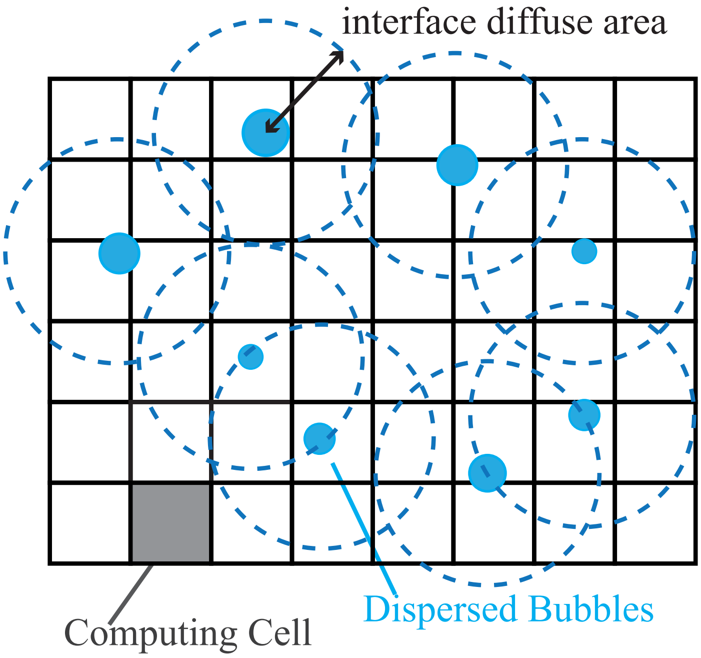

Fig. 2.2 Illustration of bubble-fluid interface diffuse area.

which gives an exact integral interpolation. The normalization condition

$$\int W(\mathbf{x}-\mathbf{x}_b,h)d\mathbf{x}=1, \tag{2.29}$$

where $d\mathbf{x}$ denotes the differential volume, is necessary for zero-order consistency. Examples of kernel functions include Gaussian kernel, cubic spline, and quartic spline [87].

In the bubbly flow simulation, we apply the Gaussian smoothing kernel function, with $\mathbf{x}_k$ and $\mathbf{x}_b$ as the 3D volume cell center location and bubble location, respectively. The Gaussian smoothing kernel function is written as

$$\zeta_\sigma\left(\mathbf{x}_k,\mathbf{x}_b\right)=\frac{1}{\left(\sigma\sqrt{2\pi}\right)^d}\mathbf{exp}\left(\left[-\frac{\left(\mathbf{x}_k-\mathbf{x}_b\right)^2}{2\sigma^2}\right]\right), \tag{2.30}$$

where d is dimension and σ is the kernel width. To save computational cost, the Gaussian kernel function can be replaced by a truncated Gaussian kernel function:

$$\zeta_\sigma(\mathbf{x}-\mathbf{x}_b) = \begin{cases} \dfrac{1}{\left(\sigma\sqrt{2\pi}\right)^d}\mathbf{exp}\left[-\dfrac{(\mathbf{x}-\mathbf{x}_b)^2}{2\sigma^2}\right],\ |\mathbf{x}_k-\mathbf{x}_b| \leq 3\sigma, \\ 0,\ |\mathbf{x}-\mathbf{x}_b| > 3\sigma, \end{cases} \tag{2.31}$$

where 3σ is the cut-off radius. To enforce mass conservation, the kernel function is normalized over the volume of integration by

$$\int_{V_{cv}} \zeta_\sigma(\mathbf{x}_k,\mathbf{x}_b)\,dV = 1, \tag{2.32}$$

Here, V_{cv} is the integration finite volume. Using the above formulations, α_g is calculated as

$$\begin{cases} \alpha_g(x_k) = \sum_{i=1}^{N_\mathrm{b}} R_{bi}\zeta_\sigma(x_k,x_b),\ \text{if } d=1; \\ \alpha_g(\mathbf{x}_k) = \sum_{i=1}^{N_\mathrm{b}} \pi {R_{bi}}^2\zeta_\sigma(\mathbf{x}_k,\mathbf{x}_b),\ \text{if } d=2; \\ \alpha_g(\mathbf{x}_k) = \sum_{i=1}^{N_\mathrm{b}} \dfrac{4}{3}\pi {R_{bi}}^3\zeta_\sigma(\mathbf{x}_k,\mathbf{x}_b),\ \text{if } d=3, \end{cases} \tag{2.33}$$

where N_b is the total number of the dispersed bubbles and R_{bi} is the radius of bubble i.

2.5 Fluid-mixture pressure

In the LE two-way coupling model, we also introduce liquid volume fraction α_l in the Eulerian frame to model how the gas bubbles affect the carrier fluid. α_l, mixture density ρ, and mixture internal energy ρe follow the following expression during gas-liquid mixing

$$\alpha_l + \alpha_g = 1, \tag{2.34}$$

$$\rho = \alpha_l\rho_l + \alpha_g\rho_g, \tag{2.35}$$

$$\rho e = \alpha_l(\rho e)_l + \alpha_g(\rho e)_g, \tag{2.36}$$

where subscripts l and g denote the carrier fluid and the gas bubbles, respectively.

We apply an isobaric closure to obtain the fluid-mixture equilibrium pressure p. To avoid numerical oscillation near the interfaces [4], such closure must have consistency properties: (a) the mixing of two fluids with the same pressure should keep a mechanical equilibrium and (b) the mixture pressure should degenerate correctly when one phase is vanishing. Here, we apply the stiffened-gas EOS to model p_l and p_g. Introducing $\xi_g = \frac{1}{\gamma_g - 1}$, $\xi_l = \frac{1}{\gamma_l - 1}$ and $\xi = \alpha_l \xi_l + \alpha_g \xi_g$, an implicit expression for p is given as [1, 96]

$$\rho e = p\xi + \alpha_l \gamma_l B_l \xi_l + \alpha_g \gamma_g B_g \xi_g, \tag{2.37}$$

which yields the equilibrium pressure

$$p = \frac{\rho e}{\xi} - \frac{1}{\xi}\left(\alpha_l \gamma_l B_l \xi_l + \alpha_g \gamma_g B_g \xi_g\right). \tag{2.38}$$

It is easy to discover that Eq. (2.38) satisfies the consistency properties. In addition, such pressure closure has been used to numerically model multicomponent flows with immiscible interface to obtain the fluid pressure [1].

2.6 Nucleation theory

2.6.1 Classical nucleation theory

CNT [58, 110] is typically applied to describe the nucleation rate in molecular dynamics (MD) simulations [8, 30]. According to CNT, a nucleus is spontaneously generated as a result of density fluctuations in the metastable liquid. MD simulations by Diemand et al. [30] agree with CNT at moderate negative pressure; however, CNT underestimates the nucleation rate at large negative pressure. As such, several alternative theories [27, 97, 98, 114] have been proposed to model the nucleation rate.

According to nucleation theory (see e.g. [35]), the nucleation rate J, which determines the average number of nuclei formed in a unit volume of the metastable fluid per unit time, is given by

$$J = J_0 n_0 \exp\left(-\frac{\triangle G}{k_B T}\right), \tag{2.39}$$

where J_0 is a prefactor, n_0 is the liquid molecule number density, ΔG is the free energy of nucleus formation, k_B is the Boltzmann constant, and T is the temperature. In CNT [16], formation free energy is

$$\triangle G_{\mathrm{CNT}} = \frac{16\pi S^3}{3\left(p_v - p\right)^2}. \tag{2.40}$$

The CNT nucleation rate has the expression

$$J_{\mathrm{CNT}} = \sqrt{\frac{2S}{\pi M}} n_0 \exp\left[-\frac{16\pi S^3}{3k_B T\left(p_v - p\right)^2}\right], \tag{2.41}$$

resulting in the prefactor $J_{0,\mathrm{CNT}} = \sqrt{\frac{2S}{\pi M}}$, where M is the molecular mass of water. The critical size of the bubble $R_{c,\mathrm{CNT}}$ is defined as the radius, at which clustering molecules are in a meta-stable equilibrium and a nucleus grows; it is expressed as

$$R_{c,\mathrm{CNT}} = \frac{2S}{p_v - p}. \tag{2.42}$$

2.6.2 Poynting correction nucleation theory

Blander and Katz [16] derived expressions of higher accuracy for the critical radius and the nucleation rate. This Poynting correction nucleation theory (PCNT) gives

$$R_{c,\mathrm{PCNT}} = \frac{2S}{\left(p_e - p\right)\delta}, \tag{2.43}$$

$$J = \sqrt{\frac{2S}{\pi M}} n_0 \exp\left[-\frac{16\pi S^3}{3k_B T\left(p_e - p\right)^2 \delta^2}\right], \tag{2.44}$$

where p_e is the equilibrium vapor pressure of the liquid. The Poynting correction factor is

$$\delta = 1 - \frac{\upsilon_l}{\upsilon_g} + \frac{p_e - p}{2p_v}\left(\frac{\upsilon_l}{\upsilon_g}\right)^2, \tag{2.45}$$

where υ_g is the molecular volume of gas and υ_l is the molecular volume of the liquid. The ratio υ_l/υ_g is assumed to be constant when T is constant. A comparison between the nucleation rate of CNT and PCNT under different p and υ_l/υ_g is discussed in Sec.4.3.2.

2.7 Summary of Lagrangian-Eulerian coupling model

In the Eulerian framework, NS equations in conservative form work as the governing equations, with a pressure closure to close the system. For each individual bubble, the radius and position change follow spherical bubble dynamics equation and bubble motion equation, respectively. The transfers of mass, moment, and energy between the dispersed and continuous phases are defined in an LE coupling scheme.

LE one-way coupling is applied in the realization of homogeneous cavitation nucleation and only considers the carrier fluid's influence on the cavitation nuclei. The 2D axisymmetric two-phase Euler equations are solved to compute shock gas bubble and bulk fluid evolution in the microchannel, applying a sharp and conservative interface model in Ref. [42, 50]. As a nucleation model, we apply the modified classical formula proposed by Blander and Katz [16]. Bubble dynamics are modeled by the spherical bubble dynamics, where the volume change of individual bubbles is determined by the pressure inside the bubble and the surrounding flow properties. A detailed description of the homogeneous cavitation nucleation scheme's realization will be given in Chapter 4.

To further consider the influence of the dispersed cavitation bubbles on the carrier fluid, LE two-way coupling is applied. Cavitating fluid mixture is assumed a homogeneous, compressible fluid by which the conservation law is solved for the fluid mixture instead of the carrier fluid. We assume that the bubbles have barely significant influence on the momentum or velocity of the mixture, due to the large density ratio between liquid and gas [18]. Thus, the bubble, carrier fluid, and mixture are assumed to share the velocity field. However, cavitation bubbles still affect the convection of the mixture by influencing the density and the pressure field. The mixture density is defined using the gas volume fraction. By tracking the bubbles' locations and solving their dynamics equations, the instantaneous gas volume fraction is derived based on the projection from the discrete bubbles to the carrier fluid [72]. To close the Eulerian system, the isobaric closure for multi-component problem is applied to describe the equilibrium pressure [4]. The close-by flow properties will be considered to model the bubble dynamics for the bubble cloud simulation in Chapter 5. We will apply this model in Chapter 5 to simulate typical problems within cavitation bubble cloud.

Chapter 3

Numerical models

In this chapter, the numerical methods of spatial discretizaion and time integration for LE model's realization are introduced. The spatial discretization of one-dimensional (1D) hyperbolic conservation law is introduced in both the finite difference (FD) and finite volume (FV) frameworks. The classical weighted essentially non-oscillatory scheme (WENO) scheme for spatial discretization and Runge-Kutta (RK) method for time integration for solving hyperbolic conservation law will be introduced. To well resolve the bubble dynamics equation especially the bubble collapse and rebound process, a variable time-step algorithm is also applied.

3.1 Spatial discretization

We describe the spatial discretization of hyperbolic conservation law in Eq. (2.17). For simplicity, the 1D hyperbolic conservation law of the conservative values **q** can be written as

$$\frac{\partial \mathbf{q}}{\partial t}+\frac{\partial}{\partial x}\mathbf{f}(\mathbf{q})=\mathbf{0}, \tag{3.1}$$

where $\mathbf{q}(x,t)=(\rho,\rho u,E)^{\mathrm{T}}$ and $\mathbf{f}(\mathbf{q})=(\rho u,\rho u^2+p,u(E+p))^{\mathrm{T}}$. The spatial discretization of Eq. (3.1) is made on a uniform mesh, with a computational cell i written as $\left[x_{i-1/2},x_{i+1/2}\right]$. A system of ordinary differential equations (ODEs) inside all grids is formed:

$$\frac{d\mathbf{q}_i}{dt}=-\frac{\partial \mathbf{f}}{\partial x}|_{x=x_i}\,, \qquad i=0,\cdots,n \tag{3.2}$$

Eq. (3.2) can be further discretized by a FD or a FV formula in a semi-discrete form.

3.1.1 Finite difference reconstruction

Eq. (3.2) can be discretized under FD framework as

$$\frac{d\mathbf{q}_i}{dt} = -\frac{1}{\Delta x}\left(\mathbf{h}_{i+1/2} - \mathbf{h}_{i-1/2}\right), \tag{3.3}$$

where the primitive function $\mathbf{h}(x)$ is implicitly defined by

$$\mathbf{f}(x) = \frac{1}{\Delta x}\int_{x_{i-1/2}}^{x_{i+1/2}} \mathbf{h}(\xi)d\xi. \tag{3.4}$$

We introduce $\widehat{\mathbf{f}}_{i\pm1/2} \approx \mathbf{h}_{i\pm1/2}$, which are reconstructed from flux $\mathbf{f}_i$ at the cell centers. After this, Eq. (3.3) is further approximated as

$$\frac{d\mathbf{q}_i}{dt} \approx -\frac{1}{\Delta x}(\widehat{\mathbf{f}}_{i+1/2} - \widehat{\mathbf{f}}_{i-1/2}), \tag{3.5}$$

where $\widehat{\mathbf{f}}_{i\pm1/2}$ is assembled by a convex combination of r candidate stencil fluxes

$$\widehat{\mathbf{f}}_{i+1/2} = \sum_{k=0}^{r-1} w_k \mathbf{f}_k. \tag{3.6}$$

The key point for FD is to reconstruct the flux $\mathbf{f}$ at the cell interface $i+1/2$ such that high-order accuracy is restored in smooth regions and monotonicity is preserved near discontinuities.

In the conservative FD frame, the discretization needs to be done in the characteristic space to avoid numerical oscillations induced by the interaction between different characteristic waves [54]. $\mathbf{q}$ and $\mathbf{f}$ are first projected into the characteristic space by using the left eigenvectors [95]. The projected fluxes are then split by flux splitting scheme to compute the correct upwind numerical flux. At last, the inviscid flux in the physical space can be obtained by a reverse projection by using the right eigenvectors.

3.1.2 Finite volume reconstruction

In FV reconstruction, we define $\widetilde{\mathbf{q}}_i$ as

$$\widetilde{\mathbf{q}}_i = \frac{1}{\Delta x_i}\int_{x_{i-1/2}}^{x_{i+1/2}} \mathbf{q}_i dx,\ \Delta x_i = x_{i+1/2} - x_{i-1/2}, \tag{3.7}$$

so $\widetilde{\mathbf{q}}_i$ is the cell averaging of $\mathbf{q}_i$, and also one approximation of $\mathbf{q}_i$ at the cell center. The conservation law Eq. (3.1) in the computational cell i can be formulated as

$$\frac{d\widetilde{\mathbf{q}}_i}{dt} = -\frac{1}{\Delta x}(\mathbf{f}_{i+1/2} - \mathbf{f}_{i-1/2}), \tag{3.8}$$

where $\mathbf{f}_{i\pm1/2}$ is the approximated flux at the cell edge $i \pm 1/2$. The cell average value $\widetilde{\mathbf{q}}_i$ is applied further to do the reconstruction of on each cell edge $\mathbf{q}_{i+1/2}$. The procedure uses the cell averaged values in the neighboring cells $\widetilde{\mathbf{q}}_{i-k}$, ..., $\widetilde{\mathbf{q}}_{i+l}$ (such cell table is defined as the stencil of the reconstruction). In FV reconstruction, it is also required to be high-order accurate if $\mathbf{q}$ is smooth in the stencil and to be essentially non-oscillatory (ENO) near discontinuities. Same as in the FD reconstruction, the FV reconstruction is also often performed in the characteristic space. The variables are first locally decomposed onto the characteristic field and then reconstructed, afterwards they are projected back to the physical filed. Indeed, $\widetilde{\mathbf{q}}_i$ is reconstructed on the left and right sides of each cell to formulate $\mathbf{q}^L_{i+1/2}$ and $\mathbf{q}^R_{i+1/2}$. An approximate Riemann problem is demanded to reconstruct the correct upwind flux.

Normally in the FV reconstruction, the conservative variables $\widetilde{\mathbf{q}}_i$ are reconstructed to derive the conservative values of $\mathbf{q}^{\mathrm{L}}_{i+1/2}$ and $\mathbf{q}^{\mathrm{R}}_{i+1/2}$. However, in the problem of the LE approach where isolated subgrid interfaces exit (the interfaces between sub-grid bubbles and the carrier fluid), there will be numerical oscillation in $p_{i+1/2}$ if it is derived by the total energy $E_{i+1/2}$ and $\xi_{i+1/2}$ at cell edges in Eq. (2.38). After reconstructing the total energy $E_{i+1/2}$ and $\xi_{i+1/2}$ in the stencil, the pressure equilibrium will not be maintained, as $\xi = \alpha_l\xi_l + \alpha_g\xi_g$ is function of the isolated volume fraction, which is formulated based on the Lagrangian calculation. A FD reconstruction makes the problem worse because the fluxes in the stencil are applied to do the interpolation. Therefore, instead of the conservative variables $\widetilde{\mathbf{q}}_i$, the primitive variables are reconstructed to better maintain the pressure equilibrium [55]. Thus in our realization, at each time step, we first build the cell-average primitive variables $\widetilde{\mathbf{o}}_i = (\widetilde{\rho}_i, \widetilde{u}_i, \widetilde{p}_i, \xi_i)$ from $\widetilde{\mathbf{q}}$ and α_g by

$$\widetilde{\rho}_i = \widetilde{\mathbf{q}}_i(1), \tag{3.9}$$

$$\widetilde{u}_i = \widetilde{\mathbf{q}}_i(2)/\widetilde{\mathbf{q}}_i(1), \tag{3.10}$$

$$\widetilde{p}_i = \frac{\widetilde{\mathbf{q}}_i(3) - \widetilde{\rho}_i \widetilde{u}_i^2}{\xi} - \frac{1}{\xi}\left(\alpha_{li}\gamma_l B_l \xi_l + \alpha_{gi}\gamma_g B_g \xi_g\right), \tag{3.11}$$

$$\xi_i = \alpha_{li}\xi_l + \alpha_{gi}\xi_g. \tag{3.12}$$

Then we use $\widetilde{\mathbf{o}}_i$ to do the reconstruction to get the left and right states of $\mathbf{o}_i$ (i.e. $\mathbf{o}^{\mathrm{L}}_{i+1/2}$ and $\mathbf{o}^{\mathrm{R}}_{i+1/2}$). In the end, $\mathbf{o}^{\mathrm{L}}_{i+1/2}$ and $\mathbf{o}^{\mathrm{R}}_{i+1/2}$ are applied to build the conservative values $\mathbf{q}^{\mathrm{L}}_{i+1/2}$ and $\mathbf{q}^{\mathrm{R}}_{i+1/2}$ and the flux vectors $\mathbf{f}^{\mathrm{L}}_{i+1/2}$ and $\mathbf{f}^{\mathrm{R}}_{i+1/2}$.

3.1.3 Weighted essentially non-oscillatory scheme

In consideration that high-order accuracy is restored in smooth regions while monotonicity is preserved near discontinuities, the key point in FD method is to reconstruct the flux $\mathbf{f}$ at the cell interface $i+1/2$. Also, in the FV method, the key point is to reconstruct the cell average value to get the left and right value of $\mathbf{q}_{i+1/2}$ of the Riemann problem.

Second order accuracy can be reached by using limiters in FV method [65]. ENO scheme reconstruction [101] is realized based on adaptive stencils. We can choose the optimal stencil to get the high-order accuracy and ENO. After that, WENO reconstruction [53] is developed which applies a combination of all the candidate stencils. WENO scheme enforces the ENO property near discontinuities while restore the high-order accuracy in smooth region. The weights in WENO reconstruction are defined to be nonlinearly adaptive and normalized by α_k as

$$w_k = \frac{\alpha_k}{\sum_{k=0}^{r-1}\alpha_k}, \; \alpha_k = \frac{d_k}{(\beta_k + \varepsilon)^2}, \tag{3.13}$$

where d_k denotes the optimal weight and is optimized to generate $(2r-1)$-th order upwind scheme with $(2r-1)$-point full stencil. For the five-point WENO schemes, the overall fifth-order accuracy is achieved with $d_0 = 0.1, d_1 = 0.6$, and $d_2 = 0.3$. ε is a small value to prevent denominator to be zero [20].

3.1.4 HLLC approximate Riemann solver

To compute the numerical flux $\mathbf{f}_{i+1/2}$, approximate Riemann solvers are presented to solve the Riemann problem at each cell edges. The most well known approximate Riemann solvers are HLL Riemann solver [43, 44] proposed by Harten, Lax, and van Leer and HLLC Riemann solver [109] proposed by Toro, Spruce and Speares. In our simulation, the HLLC Riemann solver is applied which satisfies automatically the entropy condition. Also the HLLC Riemann solver restores the contact waves that are ignored in HLL Riemann solver and gives better resolutions of the contact discontinuities. The HLLC solver resolves discontinuities sharply, and isolated shock waves and contacts exactly. Given the left and right states, the HLLC Riemann solver also preserves positivity [15]. Here, the HLLC flux can be written as

$$\mathbf{f}^{\mathrm{HLLC}} = \frac{1+\mathrm{sign}\,(b_*)}{2}\left[\mathbf{f}^{\mathrm{L}} + b_-\left(\mathbf{q}^{*\mathrm{L}} - \mathbf{q}^{\mathrm{L}}\right)\right] + \frac{1-\mathrm{sign}\,(b_*)}{2}\left[\mathbf{f}^{\mathrm{R}} + b_+\left(\mathbf{q}^{*\mathrm{R}} - \mathbf{q}^{\mathrm{R}}\right)\right], \tag{3.14}$$

where the $\mathbf{q}^*$ state is defined as

$$\mathbf{q}^{*k} = \rho_k\left(\frac{b_k - u_k}{u_k - b_*}\right)\begin{bmatrix} 1 \\ u_* \\ v_k \\ w_k \\ \dfrac{E_k}{\rho_k} + (b_* - u_k)\left[b_* + \dfrac{p_k}{\rho_k\,(b_k - u_k)}\right] \end{bmatrix}, \tag{3.15}$$

where $k = \mathrm{L}$, R. The smallest b_{L} and the other with the largest wave speed b_{R} are given as

$$b_L = \min\Big((u-c)^{\mathrm{ROE}}, u_{\mathrm{L}} - c_{\mathrm{L}}\Big),\, b_r = \min\Big((u+c)^{\mathrm{ROE}}, u_{\mathrm{R}} + c_{\mathrm{R}}\Big), \tag{3.16}$$

The wave speed b_{-} and b_{+} [15]

$$b_{-} = \min\left(0, b_{\mathrm{L}}\right), b_{+} = \min\left(0, b_{\mathrm{R}}\right). \tag{3.17}$$

The intermediate speed b_{*} is

$$b_{*} = \frac{p_{\mathrm{R}} - p_{\mathrm{L}} + \rho_{\mathrm{L}} u_{\mathrm{L}} \left(b_{\mathrm{L}} - u_{\mathrm{L}}\right) - \rho_{\mathrm{R}} u_{\mathrm{R}} \left(b_{\mathrm{R}} - u_{\mathrm{R}}\right)}{\rho_{\mathrm{L}} \left(b_{\mathrm{L}} - u_{\mathrm{L}}\right) - \rho_{\mathrm{R}} \left(b_{\mathrm{R}} - u_{\mathrm{R}}\right)}. \tag{3.18}$$

3.2 Time integration

3.2.1 Runge-Kutta scheme

To advance the conservative variables in time, a temporal integration is necessary. While implicit methods require large time step, explicit methods, e.g. the RK method [99][40], are popular for resolving the transient flows. For the ODEs derived from the conservation law (i.e. Eq. (3.1)), a second-order RK method is given as

$$\begin{aligned} \mathbf{q}^{(1)} &= \mathbf{q}^{n} + \mathbf{f}(\mathbf{q}^{n}, t_{n})\Delta t/2, \\ \mathbf{q}^{n+1} &= \mathbf{q}^{n} + \mathbf{f}(\mathbf{q}^{(1)}, t_{n} + \Delta t/2)\Delta t \end{aligned}, \tag{3.19}$$

where $\Delta t = t_{n+1} - t_{n}$ is the single time step. The choice of Δt depends on the constraint by a Courant-Friedrich-Lewy (CFL) condition [22]. The dimensionless CFL number is defined as the physical wave speed to the grid speed. The maximum CFL number in 1D simulation can be written as

$$\mathrm{CFL} = \Delta t \max_{i} \left\{ \frac{|u_{i}| + (c_{\mathrm{L}})_{i}}{\delta x_{i}} \right\}, \tag{3.20}$$

and CFL constraint is given by $0 < \mathrm{CFL} < 1$.

3.2.2 Variable time-step numerical algorithm

Given the pressure and velocity data from the Eulerian grids, behaviors of the cavitation bubbles are studied by solving the modified RP equation in Eq. (2.1). Difficulty of the solution of the RP equation lies to present successfully the collapse and rebound stages, even when a bubble has the minimum size and the rate of change of R is extremely large. When R becomes incorrect, negative, or unstable, it will lead an unsuccessful volume fraction computation in the Eulerian frame. The variable time-step numerical algorithm [3] is applied to solve this difficulty. In the variable time-step numerical algorithm, the Rayleigh-Plesset equation is rearranged as

$$\frac{\mathrm{d}^2 R}{\mathrm{d}t^2} = s,\ R(t_0) = R_0, \tag{3.21}$$

here,

$$\frac{\mathrm{d}s}{\mathrm{d}t} = -\frac{3}{2}s^2 + \frac{p_B - p_\infty - 2S/R}{\rho R} - \frac{4\mu s}{\rho R^2},\ s(t_o) = \dot{R}_0. \tag{3.22}$$

In the adaptive time step algorithm, the time step of the Lagrangian computation is related to the ratio of the bubble size. We define the time step for each bubble as $\Delta tb = tb_{n+1} - tb_n$. A criterion is set to ensure that the rate of R_n is numerically controllable in each time step. The criteria is applied as flows:

- if $\mid \Delta R_n \mid / R_n < 0.02$, $\Delta tb_{n+1} = \Delta tb_n$;
- if $\mid \Delta R_n \mid / R_n > 0.02$ and $\Delta R_n < 0$, $\Delta tb_{n+1} = \Delta tb_n / 1.3$;
- if $\mid \Delta R_n \mid / R_n > 0.02$ and $\Delta R_n > 0$, $\Delta tb_{n+1} = 1.3 \Delta tb_n$.

Variable time step algorithm is quite necessary to solve bubble dynamics equations if there is a wide range of pressure values and variations. Thus in our simulation, the time step Δtb is much smaller than the required CFL condition in Eulerian simulation. In each big time step Δt, bubbles variables are updated for several times until the integration of Δtb reaches Δt.

We reproduce the results of a test case where a gas bubble flows passively through a convergent-divergent nozzle as shown in Fig. 3.1. We assume a gas bubble is in water with the properties at the constant temperature of 300 K. We set ρ_l = 996 kg/m^3, μ = 0.798 e-3 Pa s, surface tension S = 0.072 N/m, and vapor pressure $p_v = 4240$ Pa. Using the profile of the pressure as p_∞ in Fig. 3.2, the solution in Fig. 3.3 is derived. The pressure profile drops from a maximum value of 120 kPa to a minimum value of -10 kPa and afterwards recovers back to the value of 120 kPa. The extreme collapse stage of bubble history is captured.

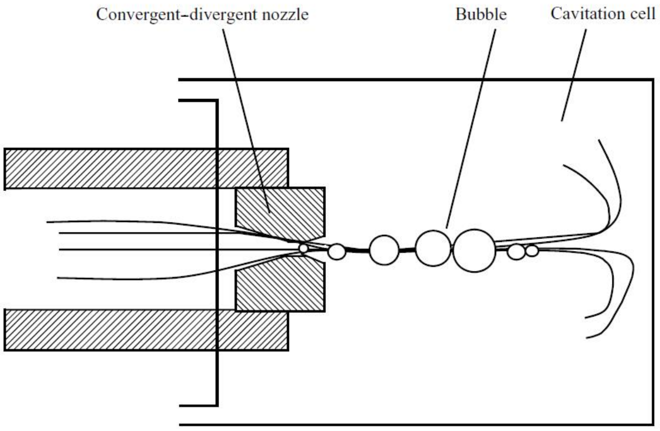
Convergent–divergent nozzle
Bubble
Cavitation cell

Fig. 3.1 Sketch of a cavitating water jet in a nozzle with a cavitating bubble passing through [90].

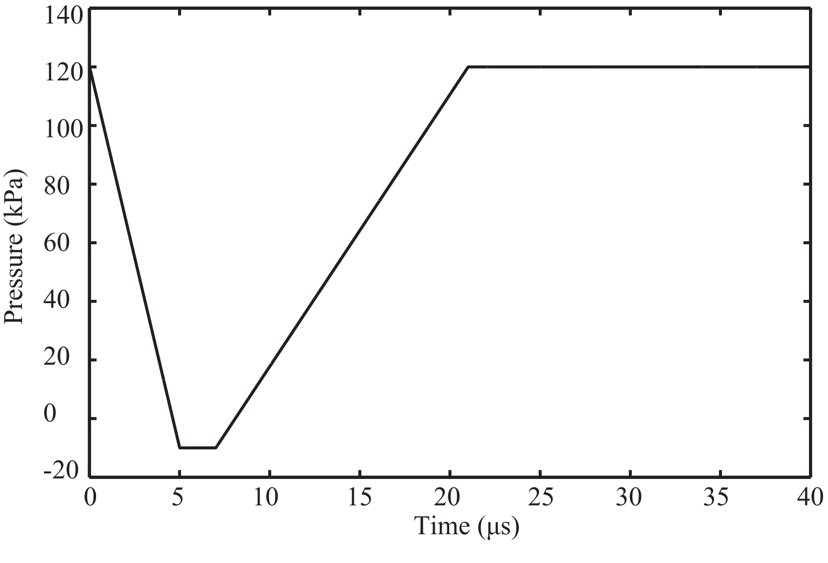

Fig. 3.2 Pressure profile along the cavitating nozzle in the test case.

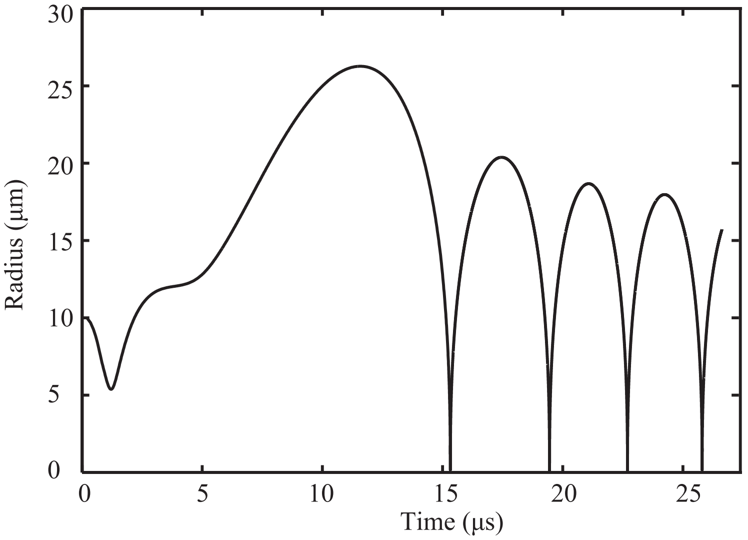

Fig. 3.3 Time change of the bubble radius when the bubble passes passively through the nozzle.

3.3 Summary

In this chapter, we reviewed the fundamental numerical methods of spatial discretization and time integration in our simulations for flow cavitation. Specially, in the LE two-way coupling model, we solve the hyperbolic conservation law in the Eulerian frame and apply the FV reconstruction to suppress the numerical oscillation that is generated at the subgrid interfaces between dispersed bubbles and the carrier fluid. Indeed, instead of the conservative variables, the primitive variables are reconstructed to better maintain the pressure equilibrium. The high-order accurate shock-capturing scheme (the fifth-order WENO) is capable to capture the discontinuity when shock exits and HLLC approximate Riemann solver for flux calculation are implemented. Second-order RK method is applied in the Eulerian calculation. The extreme collapse and rebound cycles of bubbles are captured by solving the Rayleigh-Plesset equation through the variable time-step algorithm.

Chapter 4

Homogeneous cavitation nucleation in a microchannel

The physics of nucleation in water is an important issue in many areas, ranging from biomedical to engineering applications. We simulate the underwater shock-bubble interaction induced homogeneous nucleation process in a microchannel to gain a better understanding of the mechanism of homogeneous cavitation nucleation inside water.

We use an Eulerian method, coupled with Lagrangian tracking of nuclei. The liquid expands due to the reflected shock and homogeneous cavitation nuclei are generated. We solve the 2D axisymmetric two-phase Euler equations to compute shock gas bubble and bulk fluid evolution in the microchannel, applying a sharp and conservative interface model in Ref. [42, 50]. The dynamics of dispersed vapor nuclei is coupled with the surrounding fluid in a Lagrangian frame, describing the location and size variation of each nucleus. As nucleation model, we apply the modified classical formula proposed by Blander and Katz [16], which gives a more accurate nucleation rate than the classical nucleation theory. The novelty of this chapter lies in the Eulerian-Lagrangian coupling model for the numerical simulation of homogeneous cavitation nucleation in a microchannel and a Lagrangian tracking of each nucleus. Our results reproduce nuclei distributions at different stages of homogeneous nucleation and are in good agreement with experimental results. We obtain numerical data for the negative pressure that water can sustain under the process of homogeneous nucleation. An energy transformation description for the homogeneous nucleation inside a microchannel flow is derived and analyzed in detail.

The results in this chapter have partially been published in Ref. [70].

4.1 Homogeneous nucleation

Homogeneous cavitation nucleation initializes the liquid-to-vapor transition, which is characterized by the purity in the liquid. It is different from heterogeneous nucleation with respect to where nucleation occurs. The heterogeneous nucleation emerges from surfaces in contact with two phases, while the homogeneous nucleation takes place in a bulk liquid without impurities [57, 60].

Shock-bubble interaction in a microchannel is an idealized configuration for the formation of homogeneous nucleation. After passing the gas bubble, the shock is reflected at a free-surface as expansion wave, which expands the liquid. When the pressure becomes sufficiently small (negative), homogeneous nucleation occurs [92]. The time scale of these processes is typically on the order of nanoseconds. The volume of the liquid inside the channel is sufficiently small so that we can assume that the liquid maintains purity during this time. Ando et al. [7] and Quinto [91] successfully photographed the generation of the bubble nuclei cloud induced by the bubble-shock interaction in a microchannel. However, the detailed nucleation process can hardly be detected even with high-resolution cameras.

Several researchers investigated the negative pressure that water can sustain at nucleation using various experimental techniques [11, 21, 46]. Due to variations of water purity and different water volumes, the measured negative-pressure data are quite scattered. The majority of numerical investigations focuses on topics ranging from the erosion due to cavitation to the collapse of cavitation bubble clouds. Numerical studies of homogeneous nucleation are quite scarce, and the understanding of the homogeneous nucleation mechanism is still limited.

4.2 Homogeneous nucleation in microchannel

4.2.1 Nucleation rate calculation

We note that in the simulation of homogeneous nucleation the liquid pressure p is modified using the void fraction derived from the bubble size and location distributions. Using the Gaussian kernel function in Sec. 2.4, the volume fraction of the nuclei in every Eulerian grid can be calculated as

$$\alpha_g\left(\mathbf{x}_k\right) = \sum_{i=1}^{N_{\text{nuclei}}} \frac{4}{3}\pi {R_i}^3 \zeta_\sigma. \tag{4.1}$$

The volume fraction occupied by the nuclei in the volume k is α_g and the liquid volume fraction is $\alpha_l = 1-\alpha_g$. We derive the liquid density ρ_l for all Eulerian cells as $\rho \approx \rho_l \alpha_l$, neglecting the bubble mass effects. We use Eq. (2.24) to compute the liquid pressure p corresponding to ρ_l for the nucleation rate in Eq. (2.44),

$$p = B\left(\frac{\rho_l}{\rho_0}\right)^{\gamma_w} - B + A. \tag{4.2}$$

We define $J_{i,j,k}$ as the time-dependent nucleation rate in a 3D computation cell with index $\{i,j,k\}$, which is the PCNT nucleation rate at each grid. The total number of nuclei generated during all steps is

$$N_{\text{nuclei}} = \sum_n \sum_{i,j,k} J_{i,j,k} \triangle_{i,j,k} \triangle t_n, \tag{4.3}$$

where n is the index of the time step and $\triangle_{i,j,k}$ is the cell volume in a Cartesian grid. When $N_{\text{nuclei}} > 1$, a nucleus is generated with the critical radius in a randomly chosen cell. The probability of cell $\{i,j,k\}$ being selected as the location of the nucleus at its formation is

$$P_{i,j,k} = \frac{J_{i,j,k}}{\sum_{i,j,k} J_{i,j,k}}. \tag{4.4}$$

4.2.2 Simulation set-up

A schematic of the microchannel and simulation set-up is shown in Fig. 4.1. To save computational time, we consider a 2D axisymmetric to 3D interpolation configuration. This configuration is not an inherent property of the Eulerian-Lagrangian model but rather a computational bootstrap to accelerate validation computations. The bulk flow is computed from a 2D axisymmetric formulation of the conservative laws. The Euler equations need to be coupled with the equation of state to close the system. As introduced in Sec. 2.3, for an ideal gas, the pressure is determined by the EOS of ideal gas; for water, we employ Tait's EOS. The flow field is fully interpolated to the 3D configuration for the homogeneous nucleation computation.

The bulk flow dominates bubble motion, whereas the bubble volume is mapped to the Eulerian frame for the calculation of volume fraction and nucleation rate. We justify the one-way coupling for homogeneous nucleation given that the small nuclei move passively with the bulk flow. The main steps of the homogeneous nucleation simulation in a microchannel are:

- Eulerian computation. Compute the bulk flow evolution by the adaptive multi-resolution method for multi-phase flows [42, 50] on 2D axisymmetric cells and interpolate the flow fields to 3D cells.
- Bubble growth simulation. Update the nuclei positions, velocities and radii by Eq. (2.1) and Eq. (2.8).
- Nucleation rate calculation. Compute the vapor void fraction in each 3D computation cell by Eq. (4.1), derive the modified nucleation rate by Eq. (2.44) and integrate the nucleation rate to get the total number of nuclei by Eq. (4.3) .
- Bubble initialization. The bubble initialization can be subdivided into three parts: bubble location initialization, bubble volume initialization and state variables initialization. A sketch for the bubble location initialization is show in Fig. 4.2. We mark the fluid region which has negative pressure as nucleation region where a new nucleus can be generated. We compute at each time step $\triangle N_{\text{nuclei}} = \sum_{i,j,k} J_{i,j,k} \triangle_{i,j,k} \triangle t_n$, the increment of N_{nuclei}. At the end of each time step, if $\triangle N_{\text{nuclei}} \geqslant 1$, $\triangle N_{\text{nuclei}}$ nuclei are initialized at random locations inside the nucleation region. This is done based on the probability distribution inside the selected computational cells in Eq. (4.4). The initial bubble radius is set to the critical radius (Eq. (2.43)), and the initial velocity at the bubble surface is zero. The initial bubble pressure is set to the vapor pressure, here 4230 Pa. The vapor temperature is considered to be constant and the same as in the liquid.

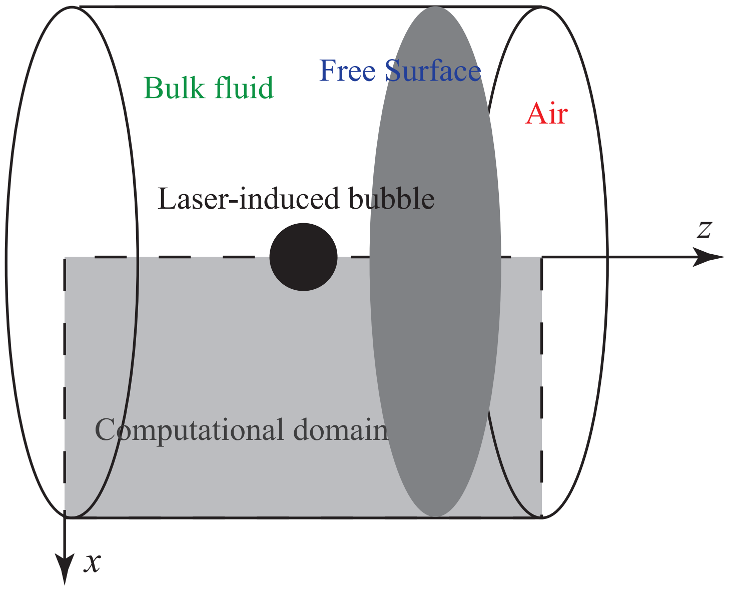

Fig. 4.1 Schematic of the simulation set-up. The laser induced shock interacts with a free surface from distance. To save computational cost, we compute only the 2D-axissymetric computational domain (light-grey region) and interpolate the results into 3D. (*Reprinted with permission from Lyu et al. [70]. Copyright 2018, PHYSICAL REVIEW FLUIDS.*)

We apply the variable time-step numerical method in Ref. [3] for solving the non-linear second-order RP equation to compute bubble growth, collapse and rebound. The evolution equations of the bulk flow are discretized with the fifth-order WENO method [53] and the second-order TVD RK scheme [100]. All computations are carried out with a CFL number of 0.3.

4.3 Results and discussion

4.3.1 Method validation

For validating our method, we consider a simplified configuration without interactions with boundaries and free surfaces. As shown in Fig. 4.1, the 2D-axisymmetric domain is 400 μm $\times$ 200 μm with the finest mesh being $[1024 \times 512]$. A gas bubble is generated initially with a radius of $8\mu m$ and centered at $(200\ \mu m, 0\ \mu m)$ and an initial pressure of 6 GPa. The time evolution of shock front and bubble-fluid interface at different resolutions are compared with experimental results of Ref. [7]

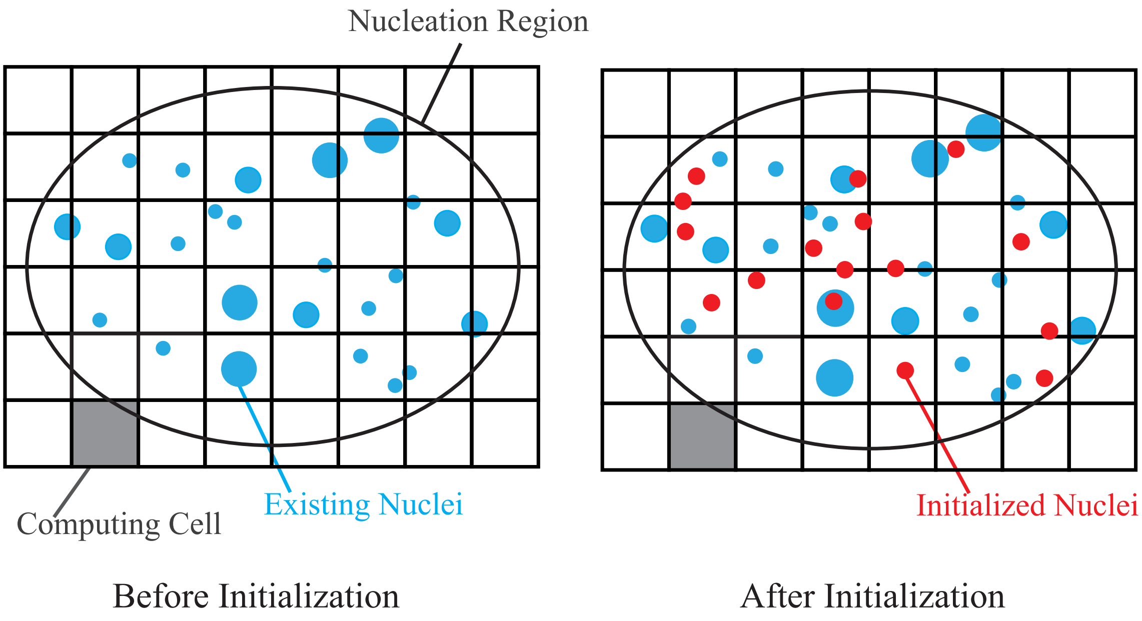
Nucleation Region
Computing Cell
Existing Nuclei
Initialized Nuclei
Before Initialization
After Initialization

Fig. 4.2 Sketch for bubble location initialization. The black circle indicates nucleation region, in which nuclei generate. At the end of each computational time step, we generate $\triangle N_{\text{nuclei}}$ nuclei, shown as red in the right figure. The location is a random selection, the probability of each computation cell is defined based on Eq. (4.4). (*Reprinted with permission from Lyu et al. [70]. Copyright 2018, PHYSICAL REVIEW FLUIDS.*)

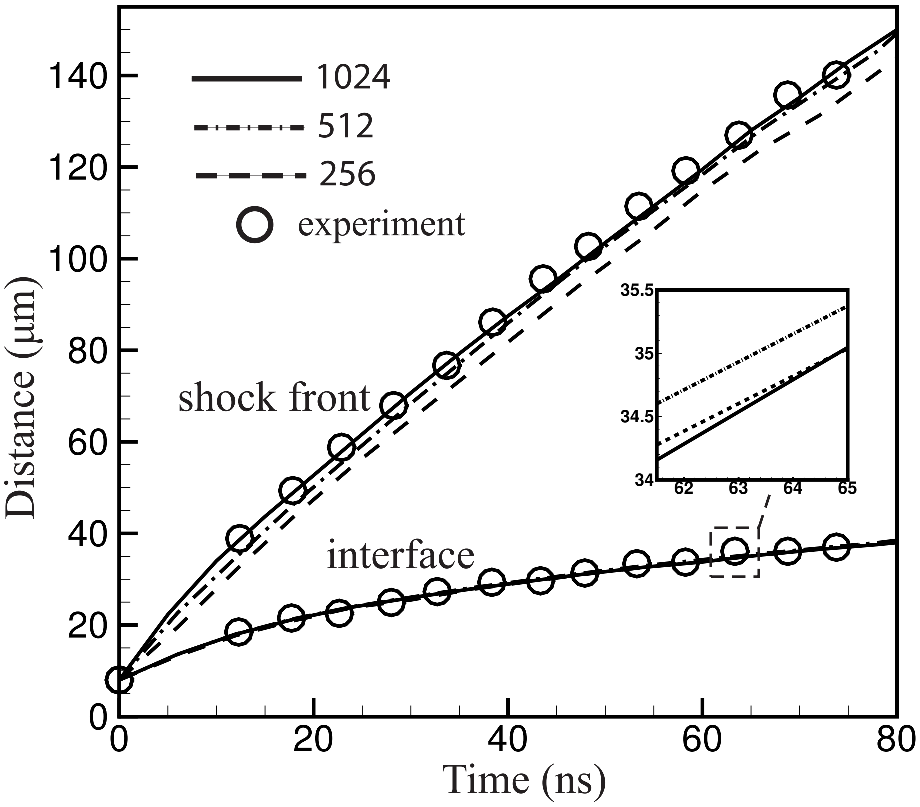

Fig. 4.3 Simulation results for the shock front and bubble-fluid interface locations with resolutions of [256 × 228], [512 × 256], [1024 × 512], and experimental results of Ref. [7]. (*Reprinted with permission from Lyu et al. [70]. Copyright 2018, PHYSICAL REVIEW FLUIDS.*)

in Fig. 4.3. We conclude, that our results agree well with the experimental results. Fig. 4.3 also illustrates the convergence of our method for different resolutions.

4.3.2 Comparison between CNT and PCNT

First, we compare the nucleation rate under extreme negative pressure between CNT and PCNT. In Fig. 4.4 (a), the nucleation rate for water at room temperature and pressures varying from -55 MPa to -100 MPa are shown, when the ratio υ_l/υ_g ratio equals to 0.01, 0.012, 0.015, 0.02, 0.05 and 0.1. We can see from Fig. 4.4 (a), that with increasing negative pressure the nucleation rate J increases. Based on the experimental observations of Ref. [7] and our simulation results in Fig. 4.5, the nucleation pressure is estimated to be around -70 ± 10 MPa. Based on this estimation, we can see that $0.012 \leq \upsilon_l/\upsilon_g \leq 0.015$ for water at room temperature. In Fig. 4.4 (b), the nucleation rate of CNT and PCNT with $\upsilon_l/\upsilon_g = 0.012$ and 0.015 from - 60 MPa to -160 MPa are presented. For extremely large negative pressure homogeneous nucleation, CNT strongly underestimates the nucleation rate by several orders of magnitudes compared to PCNT. This observation agrees well with the conclusion of Ref. [30].

4.3.3 Shock bubble induced homogeneous nucleation

We analyze also in detail the numerical simulation of homogeneous nucleation in the microchannel. We interpolate the values from the 2D-axisymmetric cells into the 3D cells and calculate $J_{i,j,k}$ for each cell. The 2D-axisymmetric domain is $400\mu\text{m} \times 200\mu\text{m}$ with the finest resolution $[1024 \times 512]$. An ideal-gas bubble is placed initially at $(200\mu\text{m}, 0\mu\text{m})$ with a radius of 8μm and an initial pressure of 6 GPa within water at $p_\infty = 1$ bar. The gas bubble at center represents the laser induced vapor region, through which a spherical shock wave expands. The shock eventually interacts with the free surface in the distance, which is 75μm away from the gas-bubble center.

Fig. 4.5 presents pressure snapshots at six different time instances (between 38 ns and 74 ns) after shock reflection at the free surface. The shock front reaches the interface at around 34 ns, afterwards the shock is reflected at the free surface and a negative pressure region (we mark this region as the nucleation region) forms between the reflected shock front and the free surface. Inside this region, homogeneous nuclei are generated, when the energy of the meta-stable water reaches the nucleation barrier. At 62 ns, the reflected shock front reaches the gas bubble-liquid interface. Between 68 ns and 74 ns, the minimum pressure inside the nucleation region decreases due to this second reflection, which indicates the final stage of the homogeneous nuclei generation. During the whole process, the minimum pressure inside water have reached roughly -80 MPa. Under this condition we estimate the nuclei to be generated. We compare simulated nuclei locations and distributions at 58 ns and 74 ns with the experimental observations in Ref. [7]. We perform numerical simulation for homogeneous nucleation with $0.012 \leq \upsilon_l/\upsilon_g \leq 0.015$. In Fig. 4.6, side views of the 3D nuclei cloud at 58 ns (first row) and 74 ns (second row) with $\upsilon_l/\upsilon_g = 0.0126, 0.0128, 0.013$ are shown together with experimental results. The comparison shows that bubble-fluid interface, nuclei

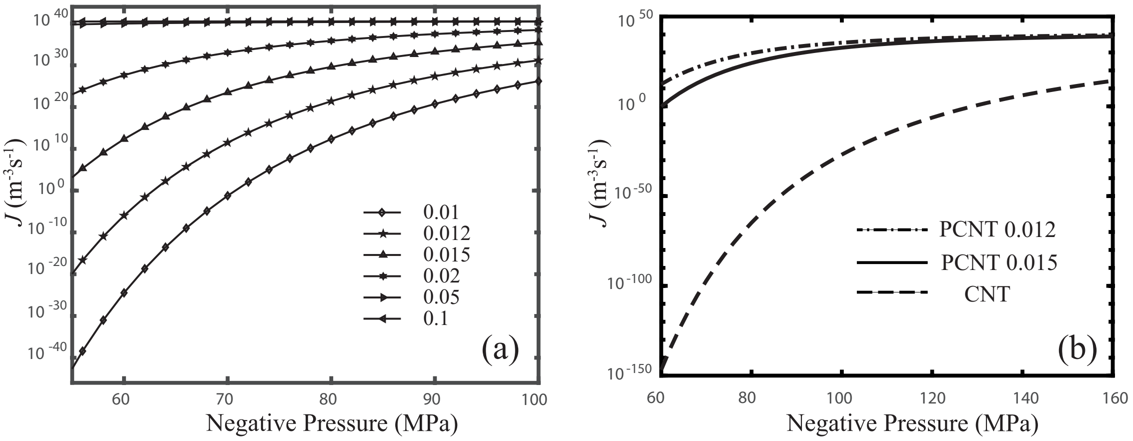

Fig. 4.4 Nucleation rate for water at room temperature and extreme negative pressure in CNT and PCNT. (a): nucleation rate of pressures from - 55 MPa to -100 MPa, when υ_l/υ_g ratio equals 0.01, 0.012, 0.015, 0.02, 0.05 and 0.1. (b): comparison of nucleation rate of CNT and PCNT with $\upsilon_l/\upsilon_g = 0.012$ and 0.015. (*Reprinted with permission from Lyu et al. [70]. Copyright 2018, PHYSICAL REVIEW FLUIDS.*)

locations and nuclei distributions in our simulation correspond well to the experiments. We believe that minor differences in nuclei density are due to experimental uncertainty. We see that υ_l/υ_g in the PCNT method influences both nuclei population and locations. When $\upsilon_l/\upsilon_g = 0.00128$, the nuclei population fits better with the experimental observations. Hence, we apply $\upsilon_l/\upsilon_g = 0.0128$ for the further simulations with different initial shock intensities.

Fig. 4.7 shows the locations of 3D homogeneous nuclei at different time instances. Details of the 3D nuclei distributions are visualized in the second row of Fig. 4.7 with the color indicating fluid pressure at the nuclei location. Between 50 ns and 54 ns, only few nuclei have formed. Afterwards, nuclei number increases significantly. Size of each nucleus also expands as pressure inside the nucleation region kept negative until around 70 ns, when the expansion wave reaches the bubble-fluid interface. Fig. 4.8 shows the evolution of the total nuclei number N_{nuclei} varying with time. As shown in Fig. 4.8 (a), we identify three main stages of the homogeneous nucleation process: the energy deposition stage, the nuclei generation stage, and the nuclei growth stage. At the first stage internal energy is deposited in the nucleation region by the shock. The shock is reflected as expansion wave, which generates large negative pressures in the nucleation region. During the second stage, we see an exponential increase in the number of the nuclei. Finally, a steady state is reached, where the

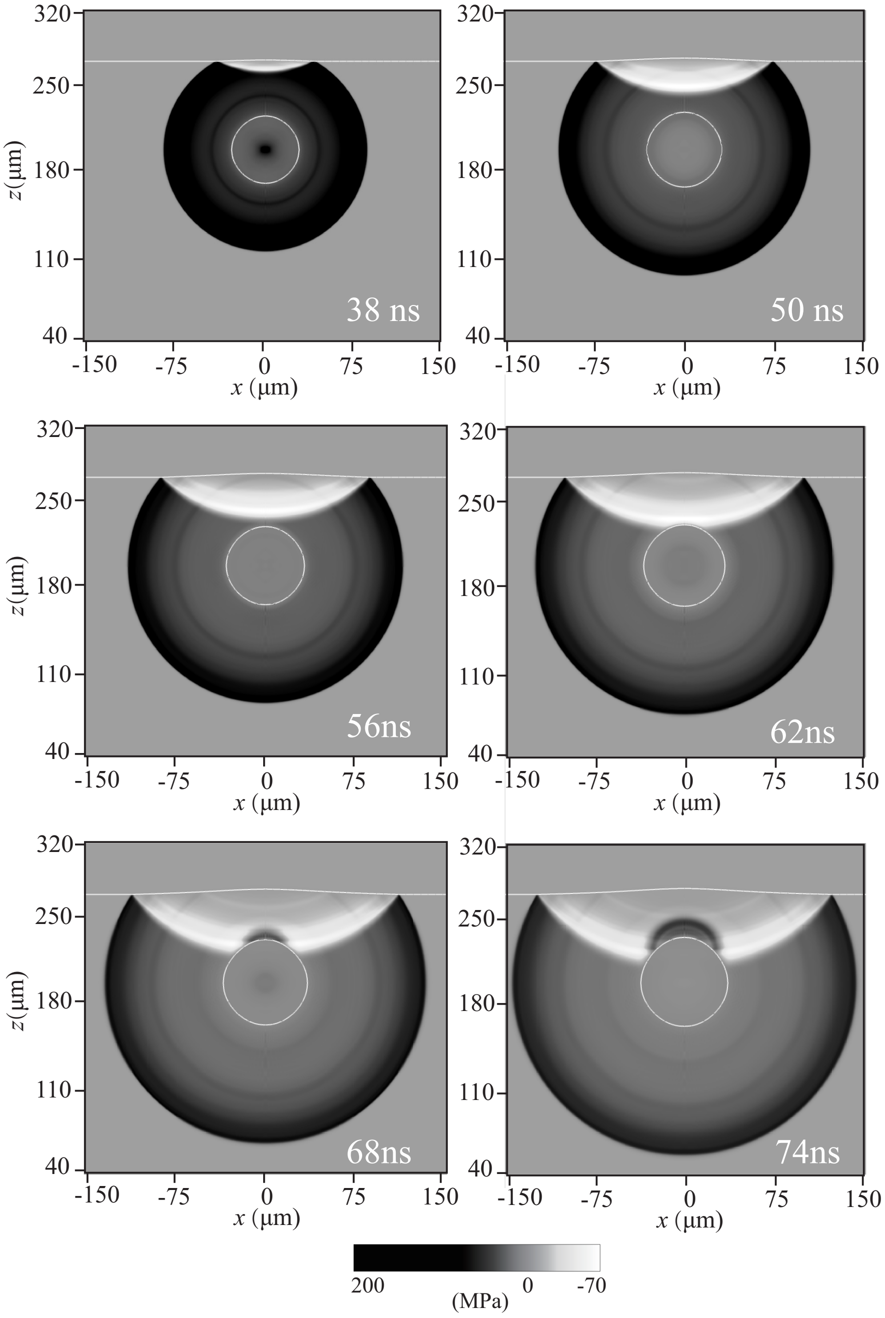

Fig. 4.5 Snapshots of the pressure field at different time instants after shock reflection at the free surface. White color indicates minimum (negative) pressure. (*Reprinted with permission from Lyu et al. [70]. Copyright 2018, PHYSICAL REVIEW FLUIDS.*)

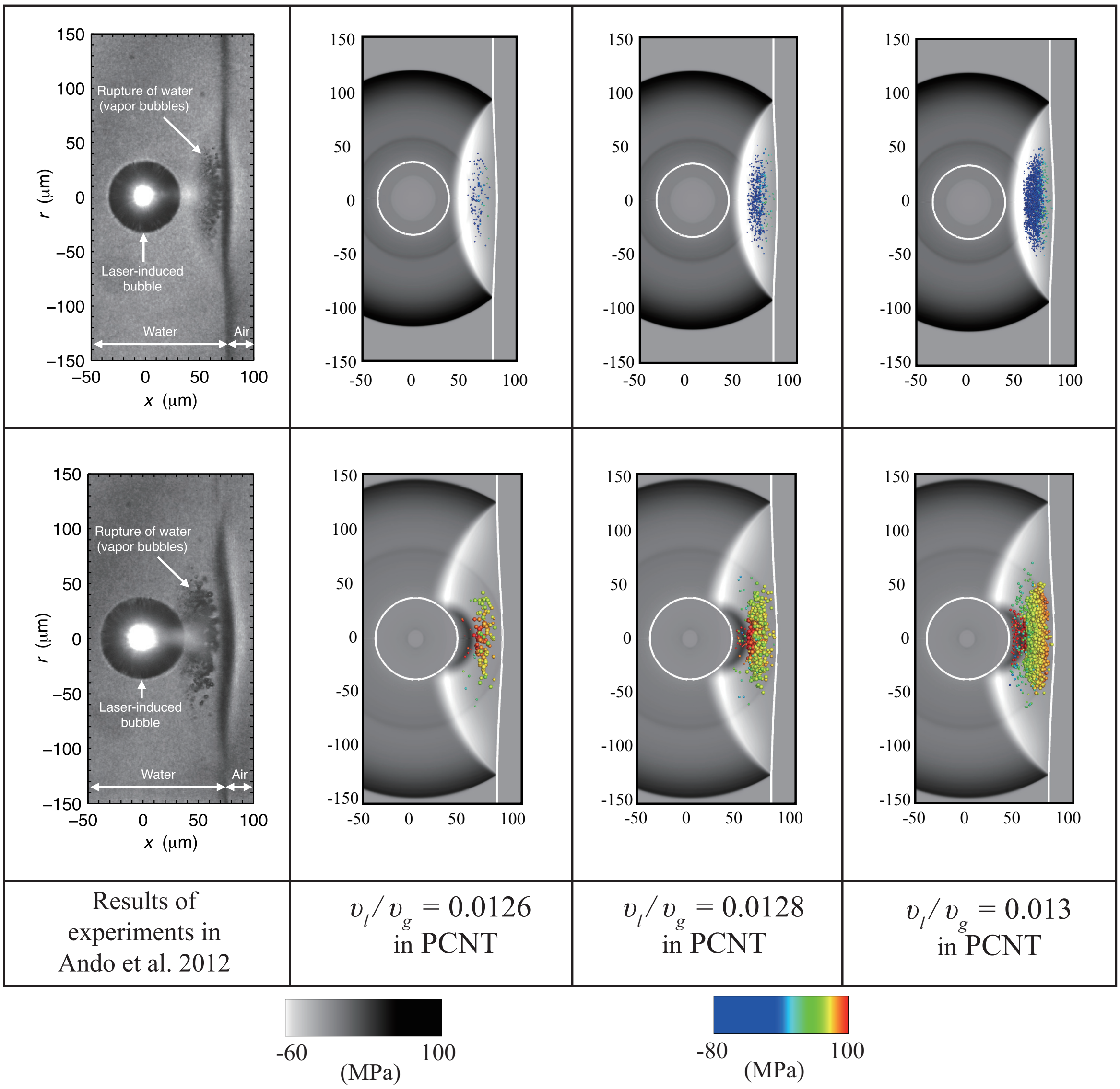

Fig. 4.6 Numerical simulation of homogeneous nucleation in comparison with the experimental results (Ando et al. 2012: Ref. [7]). The first line contains the results at 58 ns and the second row the results at 74 ns. Three numerical simulations with υ_l/υ_g being 0.0126, 0.0128, and 0.013 are shown. (*Reprinted with permission from Lyu et al. [70]. Copyright 2018, PHYSICAL REVIEW FLUIDS.*)

nuclei number saturates. The time evolution of the total nuclei number of the shock-bubble interaction induced homogeneous nucleation is presented in Fig. 4.8 (b). We see that there are two increments of the nuclei number at around 48 ns and 62 ns. From Eq. (2.44), the nucleation rate increases when the negative pressure decreases. These increments are a result of the maximum nucleation rate when the negative pressure approaches the minimum in the whole process.

We discuss the homogeneous nucleation mechanism of the three stages with respect to energy transformation. At the second stage, the driving force for nucleation is the energy derived from the inertial and potential energy of the shock. The contribution of shock energy and the expansion wave from the reflected shock induce phase transition. The third stage is the vapor volume growing stage. The rate of the continuous growth is typically controlled by the energy transfer to the nucleation region. The total growth rate of homogeneous nucleation induced by shock reflection is the deposition rate, which we can say is the driving force, and the growth rate which results from the pressure difference between the vapor and fluid pressure.

Fig. 4.9 shows the nuclei distribution at two different time instances (64 ns and 76 ns), after the nuclei number reaches the maximum value. The nuclei cluster distribution evolves with time. We fit the nuclei size distribution with a 2-parameter Weibull probability density function (PDF) which can be expressed as

$$f(R^*) = \frac{\beta}{\eta}\left(\frac{R^*}{\eta}\right)^{\beta} e^{-\left(\frac{R^*}{\eta}\right)^{\beta}}, \tag{4.5}$$

where $R^* = R/R_{\text{mean}}$. R_{mean} is the mean radius of nuclei, η is the scale parameter, and β is the shape parameter. At 64ns, the bubble radii mainly are distributed between 0 and 1.0μm, as most of the bubbles in the nucleation region are newly generated. With $R_{mean} = 2.10\mu$m, the nuclei distribution fits well a Weibull distribution with $\eta = 1.11$ and $\beta = 3.5$. At 76ns, the end stage of homogeneous nucleation, the bubble radii mainly are between 0.9μm and 3.0μm. R_{mean} equals 3.74μm. The distribution fits well with a pdf with $\eta = 1.06$ and $\beta = 7.3$.

The nuclei distribution fits well with the Weilbull distribution. Fitting results at six time instants (between 64 ns and 84 ns) are plotted together in Fig. 4.10. At the same time, time evolution of the mean radius, scale and shape parameters in PDF fitting are shown in Fig. 4.11. In general, the PDF

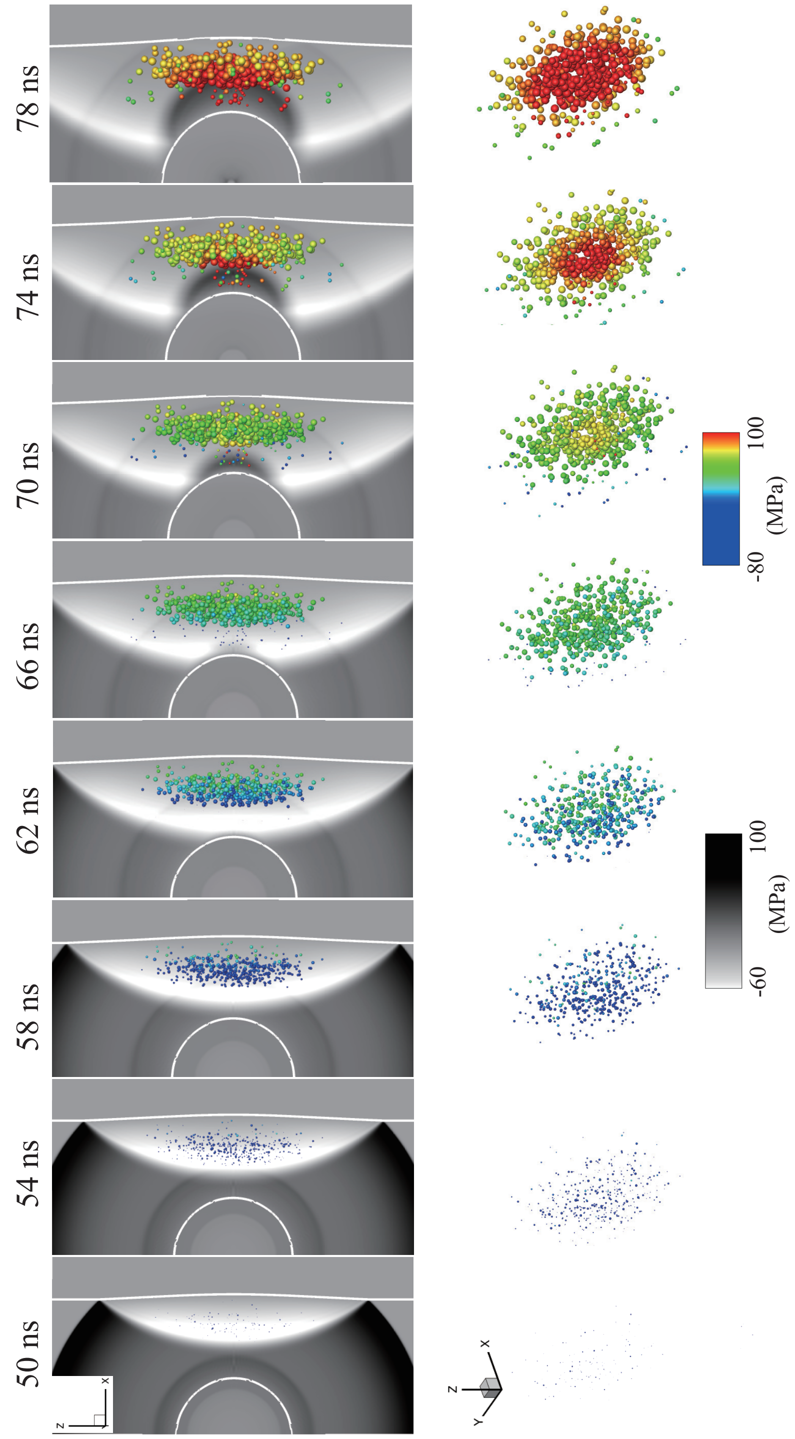

Fig. 4.7 Nuclei in the nucleation region at different instances plotted with the background fluid pressure field. 3D vapor bubble distributions at each time instance are shown in the second row, with the color indicating the bulk fluid pressure at the each nucleus location. (*Reprinted with permission from Lyu et al. [70]. Copyright 2018, PHYSICAL REVIEW FLUIDS.*)

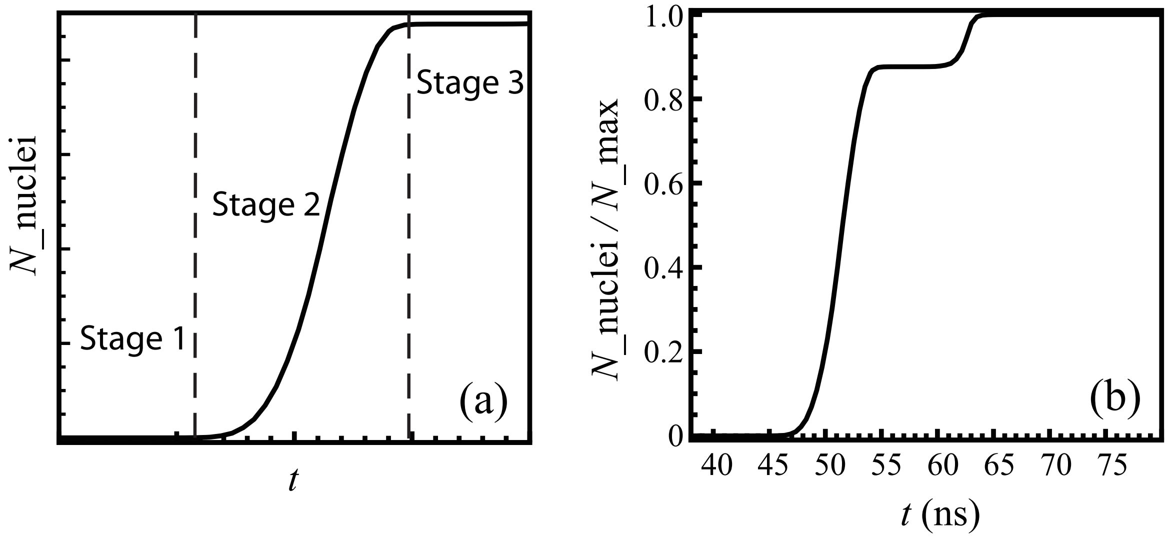

Fig. 4.8 (a): Time history of the nuclei number with the indications of the three stages of a general homogeneous nucleation process. (b): Time history of the nuclei number in the shock-bubble interaction case, here, N_{max} is the number of the nuclei formed until the last stage of nucleation. (*Reprinted with permission from Lyu et al. [70]. Copyright 2018, PHYSICAL REVIEW FLUIDS.*)

varies with time. Mean radius, scale and shape parameters of the Weibull PDF change with time increasing. Only the scale parameter η changes weakly.

4.3.4 Water pressure at homogeneous nucleation

In this section, we analyze the negative pressure threshold in water where homogeneous nucleation takes place. Experimental results are quite scattered. The cavitation threshold ranges from -16 MPa to -140 MPa due to different temperatures and volumes of the water samples. A summary of the experimental results can be found in Ref. [46]. Fig. 4.12 shows the pressure evolution along the symmetry axis at times 58 ns, 60 ns and 62 ns of the shock-bubble induced homogeneous nucleation during which negative pressure reaches the threshold and induces the nuclei cluster growth in population. At 58 ns, when only few new homogeneous nuclei are generated, the minimum pressure is around -72.8 MPa. Afterwards, at around 60 ns, there is an obvious increase of the nuclei population. We observe the absolute minimum pressure during nucleation, about -76.0 MPa, which we say is the negative pressure threshold. Subsequently, at 62 ns, the minimum pressure inside the nucleation region is about -73.6 MPa, at this time, the homogeneous nucleation reaches the steady state.

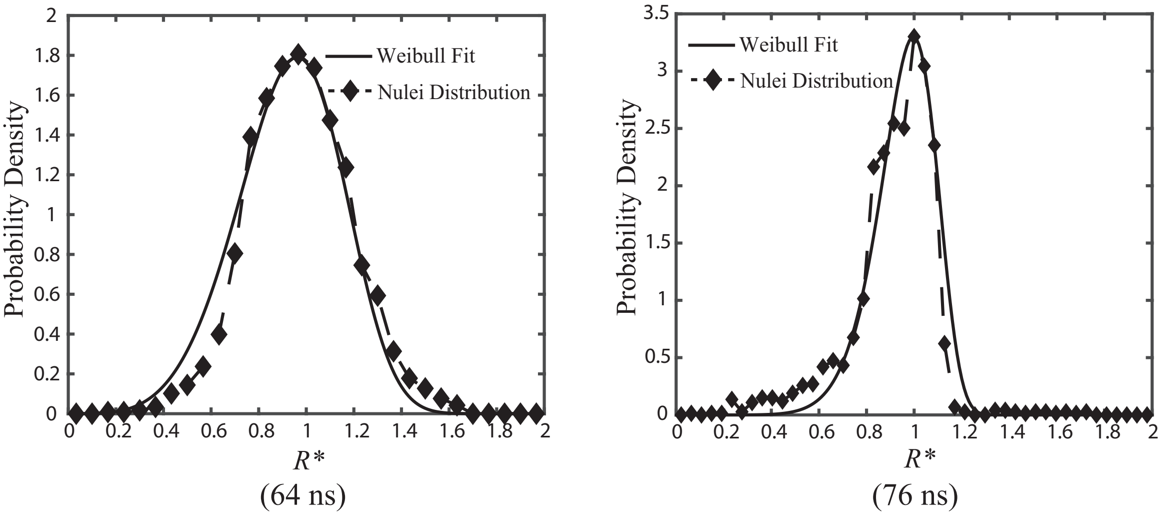

(64 ns) (76 ns)

Fig. 4.9 The nuclei radius distributions and Weibull fits at 64 ns and 76 ns. Here, $R^* = R/R_{\text{mean}}$. At 64 ns, $R_{\text{mean}} = 2.10\mu$m, $\eta = 1.11$ and $\beta = 3.5$, and at 76 ns, $R_{\text{mean}} = 3.74\mu$m, $\eta = 1.06$ and $\beta = 7.3$. (*Reprinted with permission from Lyu et al. [70]. Copyright 2018, PHYSICAL REVIEW FLUIDS.*)

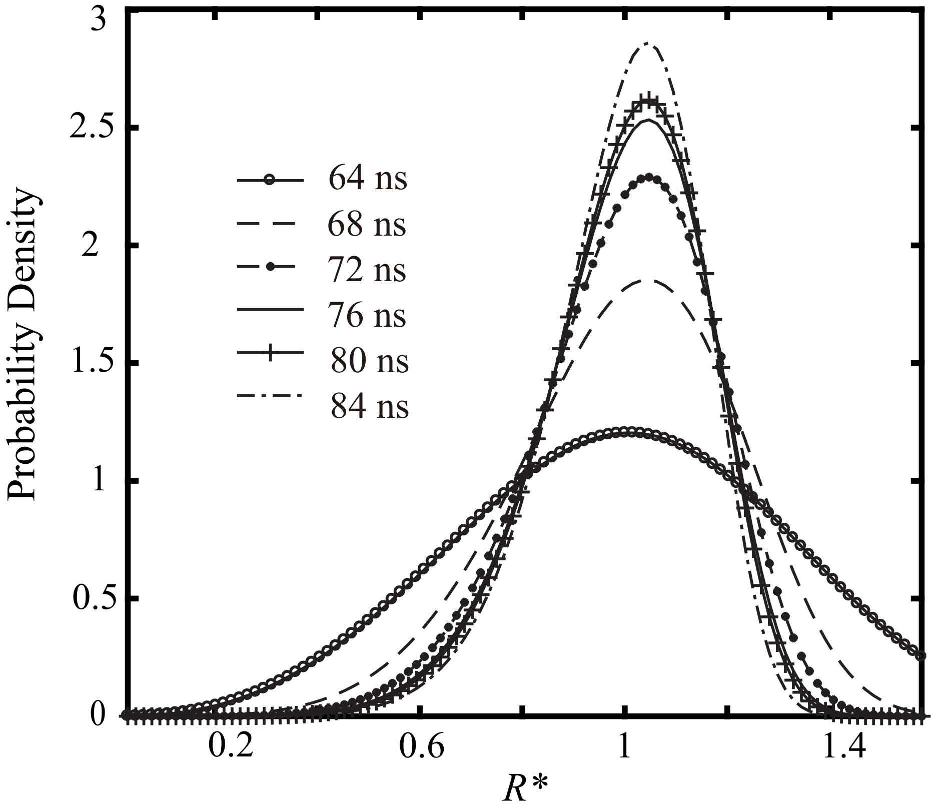

Fig. 4.10 The fitted Weibull distributions for nuclei at different time seconds ranging from 64 ns to 84 ns. (*Reprinted with permission from Lyu et al. [70]. Copyright 2018, PHYSICAL REVIEW FLUIDS.*)

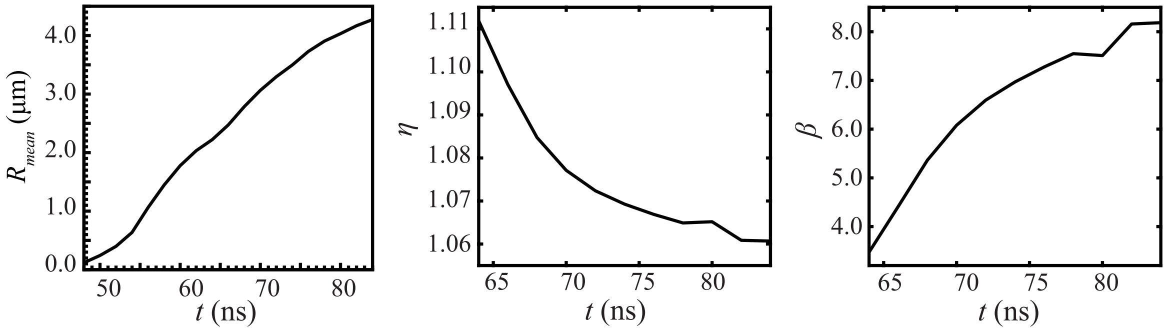

Fig. 4.11 Time evolution of mean radius R_{mean}, scale η and shape β parameters. In general, mean radius and shape parameter increase with time. In reverse, scale parameter decreases with time increasing, but with a small change. (*Reprinted with permission from Lyu et al. [70]. Copyright 2018, PHYSICAL REVIEW FLUIDS.*)

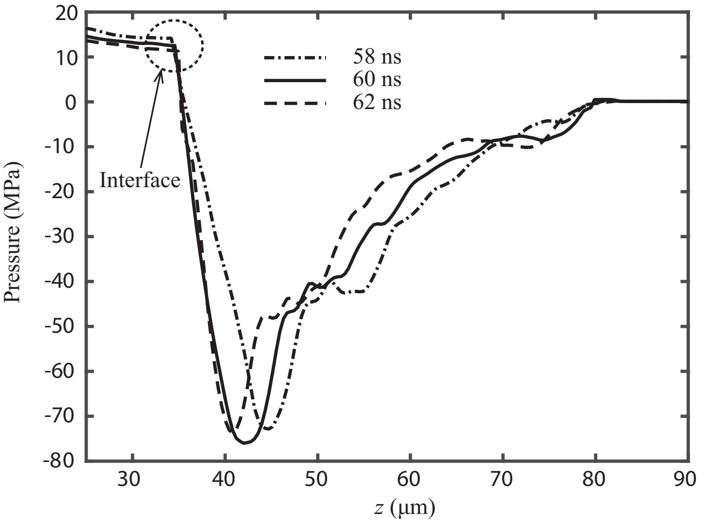

Fig. 4.12 Pressure evolution in the nucleation region along the distance from the gas bubble center at 58 ns, 60 ns, and 62 ns. (*Reprinted with permission from Lyu et al. [70]. Copyright 2018, PHYSICAL REVIEW FLUIDS.*)

4.3.5 Homogeneous nucleation under different shock amplitudes

To understand the influence of the initial shock amplitude, which represents different initial energy input, on the process of homogeneous nucleation, we present in this section a set of simulations with different initial shock amplitudes inside the center gas bubble. The set-up is the same as is Sec. 4.2. The controlled variable is the initial pressure inside the gas bubble, which we set in the range from 5.8 GPa to 6.1 GPa. Nuclei in the nucleation region at different instances are plotted with the background fluid pressure field when the initial shock amplitudes are 5.85 GPa and 6.1 GPa are plotted in Fig. 4.13 and Fig. 4.14, respectively. Fig. 4.15 shows that the maximum number of nuclei $N_{\max}$ increases non-linearly when initial shock intensity increases. For shock intensity of 5.8 GPa, $N_{\max} = 62$. For smaller shock intensities, only few nuclei are generated. For shock intensity of 6.1 GPa, $N_{\max} = 1305$. To detect at which time the nuclei population starts to increase exponentially, time progression of the non-dimensional parameter $N_{\text{nuclei}}/N_{\max}$ for shock intensities of 5.8 GPa, 5.9 GPa, 6.0 GPa and 6.1 GPa is presented in Fig. 4.16. From Fig. 4.16, we see that N_{nuclei} increases at the same time instant for shocks with different intensities. We conclude that the initial shock amplitude influences mainly the maximum nuclei number. For the nucleation time, there is almost no effect.

4.4 Summary

In this chapter, the LE one-way coupling framework was introduced to a sharp-interface multiphase fluid model for numerical simulation of homogeneous cavitation nucleation in microchannel, describing simultaneously the dynamics of continuous fluid and dispersed vapor bubbles. A modified classical nucleation theory in Ref. [16] was applied to model homogeneous nucleation induced by the shock-bubble interaction in the microchannel. The main conclusions are as follows: homogeneous nucleation inside a microchannel can be separated into three stages: energy deposition stage, nuclei generation stage, and nuclei growth stage. The modified classical nucleation theory predicts a homogeneous nucleation rate which is in good agreement with the experiment. Homogeneous nucleation is a result of the negative pressure induced deposition rate and growth rate. The nuclei cluster distributions fit well with a 2-parameter Weibull probability density function. The absolute minimum pressure during nucleation in a microchannel is about -76.0 MPa. A set of simulations

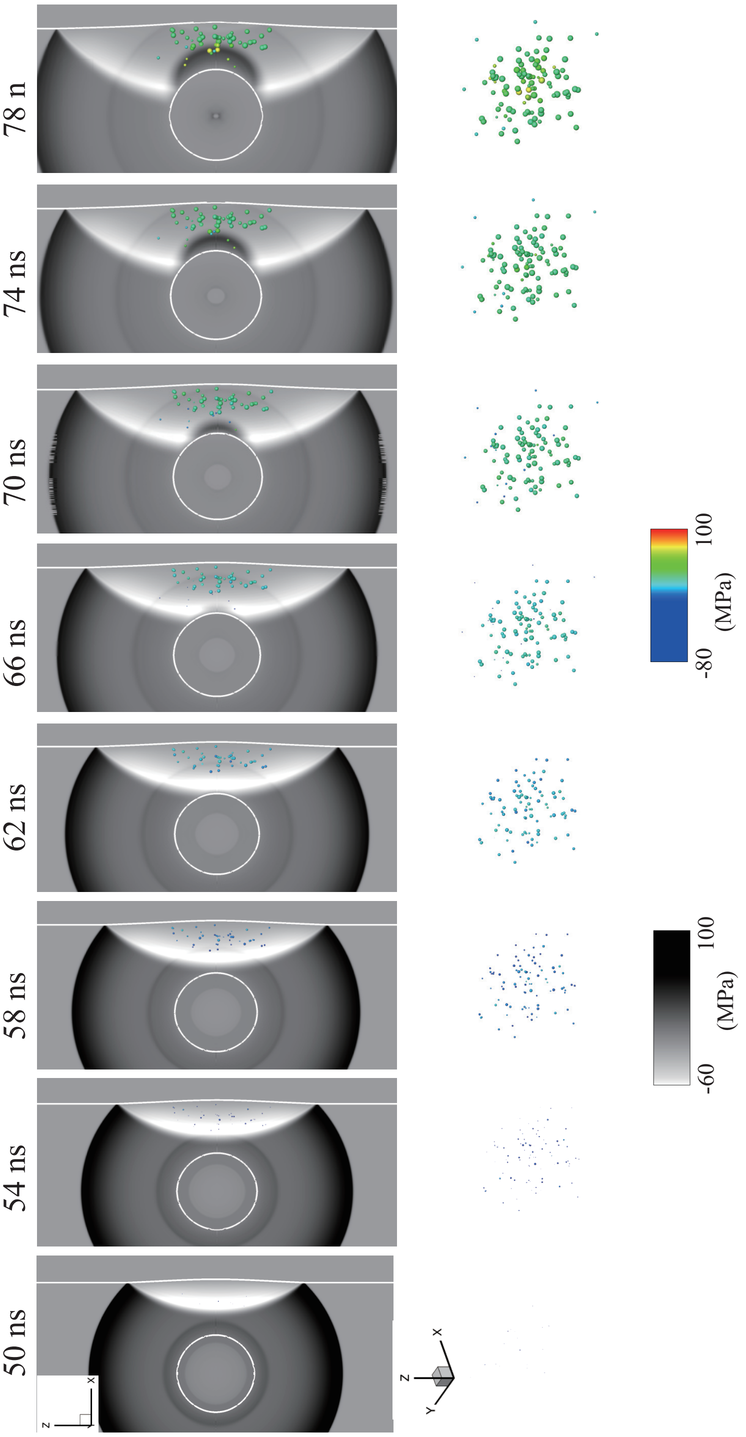

Fig. 4.13 Nuclei in the nucleation region at different instances plotted with the background fluid pressure field when the initial shock amplitude is 5.85 GPa. 3D vapor bubble distributions at each time instance are shown in the second row, with the color indicating the bulk fluid pressure at the each nucleus location.

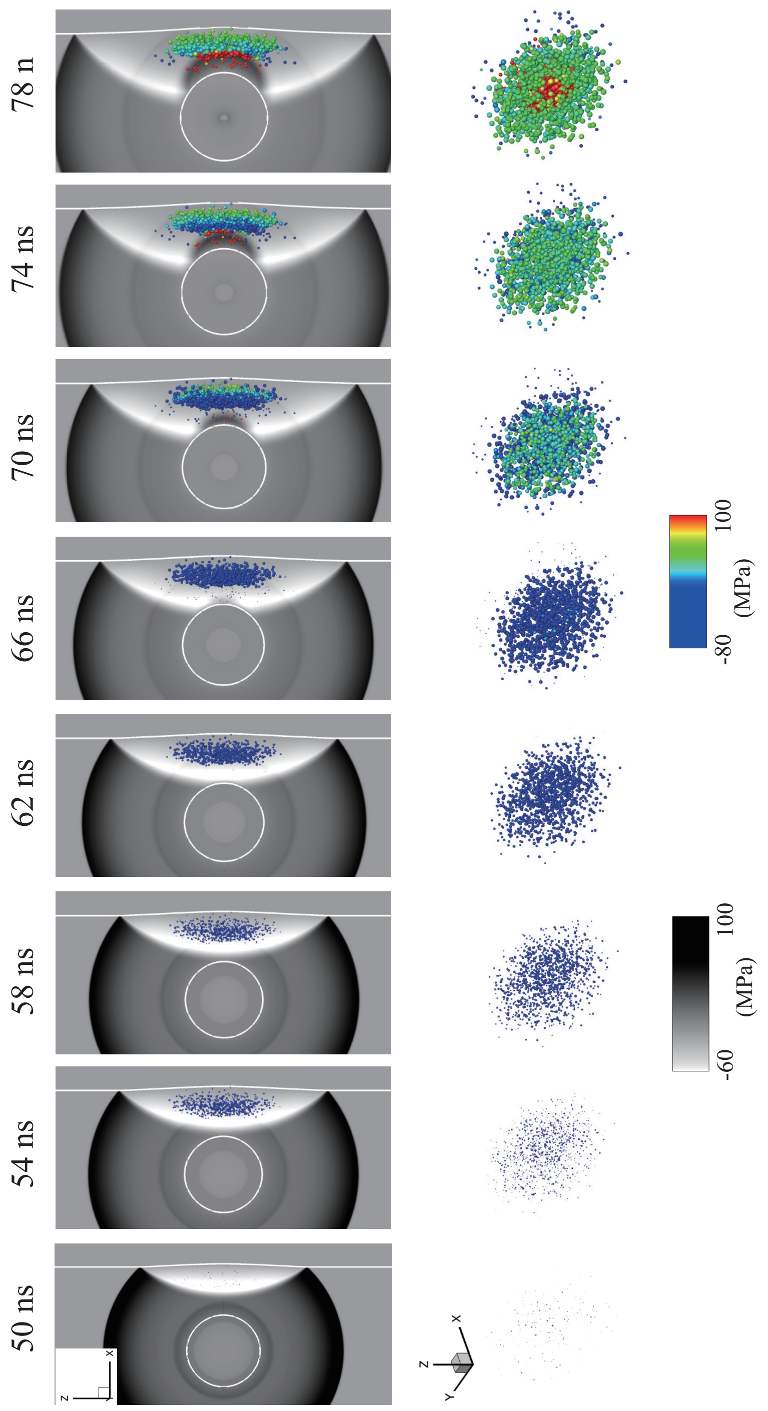

Fig. 4.14 Nuclei in the nucleation region at different instances plotted with the background fluid pressure field when the initial shock amplitude is 6.1 GPa. 3D vapor bubble distributions at each time instance are shown in the second row, with the color indicating the bulk fluid pressure at the each nucleus location.

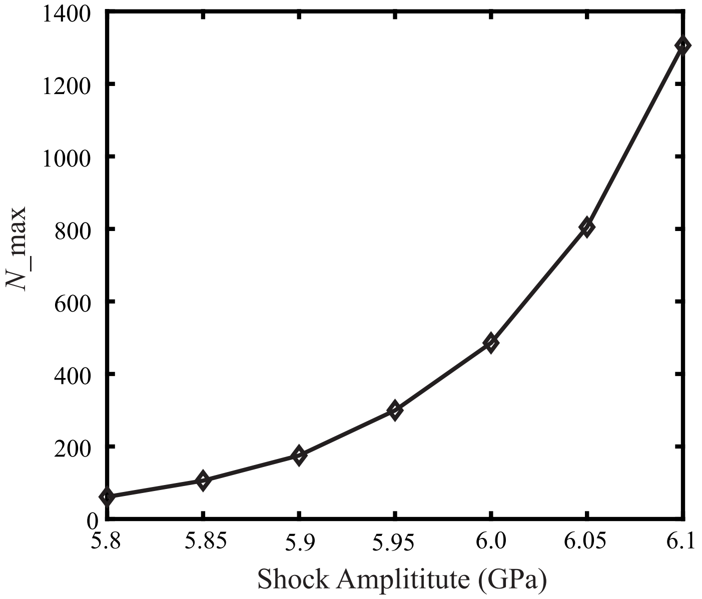

Fig. 4.15 Maximum of the nuclei number $N_{\max}$ increases when initial shock amplitude inside the gas bubble increases from 5.8 GPa to 6.1 GPa. (*Reprinted with permission from Lyu et al. [70]. Copyright 2018, PHYSICAL REVIEW FLUIDS.*)

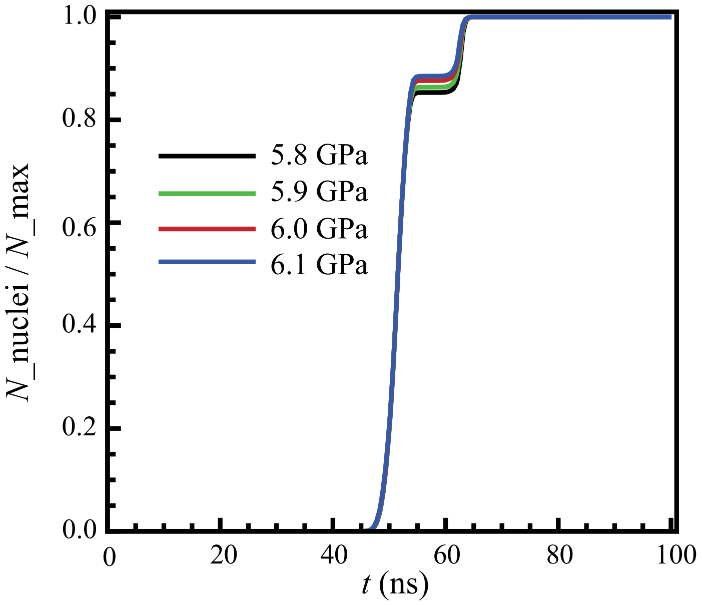

Fig. 4.16 Time dependencce of the dimensionless parameter $N_{\text{nuclei}}/N_{\max}$ for different shock amplitudes. (*Reprinted with permission from Lyu et al. [70]. Copyright 2018, PHYSICAL REVIEW FLUIDS.*)

with different initial shock amplitudes was presented, through which we find that shock intensities have no significant influence on the time instant when nuclei are generated.

Chapter 5

The Lagrangian-Eulerian two-way coupling model

Collapsing bubbles play an important role in the applications of underwater explosions, ultrasonic cleaning, and non-invasive biomedical processes. For example, in the application of shock-wave lithotripsy, the collapse of caviation bubbles plays the dominant role for fragmenting kidney or gall stones. After the interaction with shock waves induced from cavitation bubble collapse, the stone or tissue generates acoustic signals which induces rather complex acoustic pressure field. Those acoustic signals propagate to the cavitation bubbles and induce bubble vibrating dynamically. The whole process results in the complex pressure field, comprising the shock wave and acoustic pressure disturbances, which is hardly detected and distinguished experimentally. Meanwhile, the detailed collapse dynamics of bubble clusters has been poorly investigated in experiments, as the length scale and the time scale during the collapse and the bubble oscillation could hardly be detected due to measurement limitations.

In this chapter, we validate the LE two-way coupling model with several benchmark cases and further apply it to investigate a bubble cloud's influence on a sinusoidal pressure wave when the pressure pulse travels through the bubble cloud. In the end, we perform a 3D simulation of the Rayleigh collapse of a bubble cloud and analyze, in detail, the extreme pressure induced by the violent collapse of bubbles and the size distribution of bubbles during the collapse.

5.1 Key points of LE model

In the LE two-way coupling model, it is assumed that the cavitating fluid mixture is a homogeneous compressible fluid in the Eulerian frame. At the same time, each individual bubble in the cavitation bubble cloud is modeled using Lagrangian discrete tracking. The fluid mixture evolves according to the conservation law stated in Eq. (2.17). We assume that the bubbles do not significantly influence the momentum or the velocity of the mixture, due to the large density ratio between liquid and gas [18]. Thus, the bubble, the carrier liquid, and the mixture are assumed to share the local velocity. However, the bubbles still affect the convection of the mixture because they influence the local density and the pressure field of the Eulerian fluid, as described in Sec. 2.4 and Sec. 2.5.

5.1.1 Volume fraction calculation

We apply the truncated Gaussian distribution function in Sec. 2.4 to calculate the gas volume fraction in mapping the dispersed particles to the Eulerian grids. Note that bubbles may become several times larger than their initial sizes, so a constant kernel width σ will not meet the requirement that the gas volume fraction is sufficiently smooth at each time step. To ensure that the interfaces are fully diffused in neighbor cells and to avoid a negative volume fraction, σ should be larger than both the grid size and the maximum bubble radius, i.e.,

$$\sigma > \max\left(\max\left(R_{bi}\right), \mathrm{d}x\right), \tag{5.1}$$

where dx is the grid size at the finest level of the multi-resolution mesh [42]. The restriction that the distance between bubbles should be characteristically large is not addressed, which means that the diffuse areas within the kernel widths of different bubbles are allowed to overlap. Thus, this model can only resolve a pressure wave if its length is greater than σ. Pressure waves shorter than σ will be merged.

5.1.2 Modified bubble dynamics

In the classical RP equation (Eq. (2.1)), the radius R of a spherical bubble is determined by the pressure inside bubble (p_B) and the infinity flow properties (p_∞ and ρ_∞). However, due to the existence of a bubble cloud rather than a single, for the RP equation, the reference ρ and p of the surrounding liquid at infinity should not be defined as the ρ_∞ and p_∞ to model bubble cloud dynamics. To obtain the ρ_∞ and p_∞ in Eq. (2.1), we define the fluid surrounding each bubble as the fluid mixture inside a limited volume V_s, which encloses the bubble and is larger than the kernel support area. V_s is marked by $|\mathbf{x}_k - \mathbf{x}_{bi}| \leq 6\sigma$. For bubble i, ρ_∞ and p_∞ have the expression

$$\begin{aligned} p_\infty &= \frac{1}{V_s} \int_{V_s} p \mathrm{d}V, \\ \rho_\infty &= \frac{1}{V_s} \int_{V_s} \rho \mathrm{d}V, \end{aligned} \tag{5.2}$$

respectively.

5.1.3 Finite volume construction

In FV reconstruction, a high degree of accuracy is required for a variable to be smooth in the stencil and to be essentially non-oscillatory near discontinuities. In this chapter, the Eulerian equations are solved using the fifth-order WENO reconstruction [53].

In most cases of FV reconstruction, the conservative variables $\mathbf{U}$ are reconstructed to derive the conservative values of $\mathbf{U}^{\mathrm{L}}$ and $\mathbf{U}^{\mathrm{R}}$ at cell edges. However, when using the LE model to tack the isolated interfaces, this reconstruction is problematic because the numerical oscillation introduced in the pressure which is calculated from the total energy E and ξ, which means that the pressure equilibrium will not be maintained. Therefore, instead of applying the conservative variables $\mathbf{U}$, the primitive variables are reconstructed to better maintain the pressure equilibrium [55]. As a result, in this realization, we first build the primitive variables $\mathbf{O} = (\rho, u, v, w, p, 1/(\xi))$ based on the description in Sec. 3.1.2 then use $\mathbf{O}_i$ to reconstruct the left state $\mathbf{O}^{\mathrm{L}}_{i+1/2}$ and the right state $\mathbf{O}^{\mathrm{R}}_{i+1/2}$. In the end, $\mathbf{O}^{\mathrm{L}}_{i+1/2}$ and $\mathbf{O}^{\mathrm{R}}_{i+1/2}$ are applied to build the conservative values $\mathbf{U}^{\mathrm{L}}_{i+1/2}$ and $\mathbf{U}^{\mathrm{R}}_{i+1/2}$ and the flux vectors $\mathbf{F}^{\mathrm{L}}_{i+1/2}$ and $\mathbf{F}^{\mathrm{R}}_{i+1/2}$.

5.1.4 Time integration

The second-order RK scheme is applied for the Eulerian time integration. The time-step $\Delta t = t_{n+1} - t_n$ in the Eulerian frame of reference depends on the CFL conditions [22]. The dimensionless CFL number is defined as the physical wave speed to the grid wave speed. All computations in this chapter are carried out with a CFL number of 0.6.

In the Lagrangian frame, when bubble radius R becomes incorrect, negative, or unstable, it will lead to an unsuccessful volume fraction computation in the Eulerian frame. The variable time-step numerical algorithm [3] is applied to solve this difficulty.

5.2 Computing procedure

The overall computing procedure of the LE two-way coupling model can be briefly summarized as follows:

- Lagrangian computation. Update the gas bubbles positions $\mathbf{x}_b$ and radii R. $\dot{\mathbf{x}}_b$ is directly derived from the velocity field $\mathbf{u}$ of the mixture. The radius R is updated using Eq. (2.1). The p_∞ and ρ_∞ in Eq. (2.1) are derived using Eq. (5.2).
- Update the volume fraction in each computation cell using Eq. (2.33).
- Eulerian computation. Compute the temporal evolution of the fluid mixture using the adaptive multi-resolution method [42, 50]. The isobaric pressure closure in Eq. (2.38) is applied to derive the equilibrium pressure p.

5.3 Validation

5.3.1 Isolated bubble

As a validation of this method, we reproduce the results which have been published in Ref. [36, 73]. A single gas bubble inside water is excited by a pressure wave towards the bubble center. The pressure wave follows

$$p_l = \begin{cases} p_0 + \triangle p \sin(2\pi f t),\, 0 \le tf < 1, \\ p_0,\, tf \ge 1, \end{cases} \tag{5.3}$$

where p_0 = 1 atm, $\triangle p$ = 2 atm, and f = 150 kHz. The bubble's initial radius is R_{b0} = 50 μm and the bubble's pressure p_B is initially in equilibrium with p_0. This case is simulated in both 1D and 3D. In

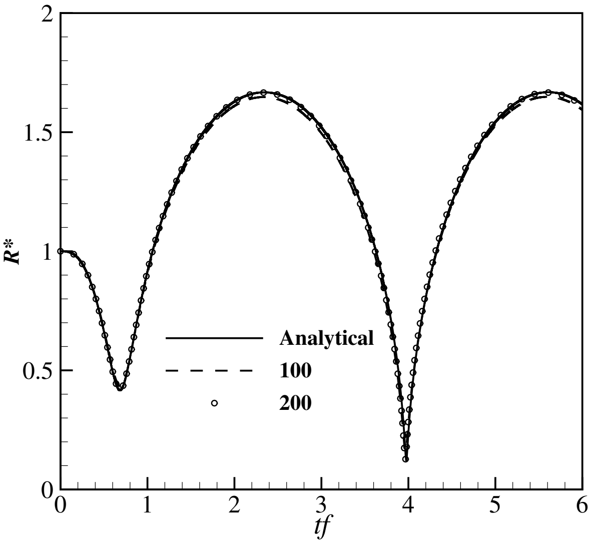

Fig. 5.1 Progression of the dimensionless bubble size $R_* = R/R_{b0}$ of 1D simulation. Results of grid resolutions of 100 (dx = 4 R_{b0}) and 200 (dx = 2 R_{b0}) are compared with the analytical solution.

the 1D simulation, the domain is 20 mm and the grid size dx is $4R_{b0}$ or $2R_{b0}$. The width of the kernel support is initialized as $6R_{b0}$. The results for two simulations using different grid sizes as well as their analytical solutions are plotted in Fig. 5.1. It is clear that the results agree with the analytical solutions for both the amplitude of the bubble's radius and the bubble's frequency. In the 3D simulation, the domain is 20 mm × 10 mm × 10 mm with two grid setups ([64 × 32 × 32] or [32 × 16 × 16]). A spherical bubble with identical initial conditions is placed at the center of the computational domain. The time evolutions of the dimensionless parameter R^* for two different meshes and the analytical solution are shown in Fig. 5.2. Compared to the results in Ref. [36], which use the resolution [100 × 50 × 50], our model efficiently solves the bubble radius time history with a coarse resolution of only [64 × 32 × 32]. Since our model applies the isobaric closure and the modified RP equation, it calculates with sufficient accuracy the pressure and the density field surrounding the bubbles, even using a coarse resolution.

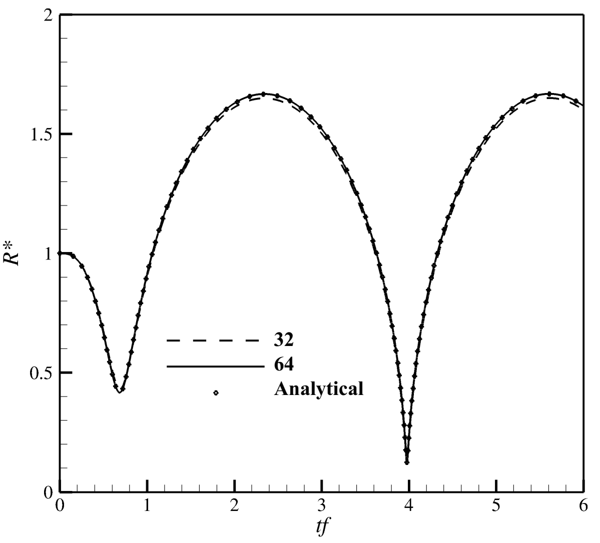

Fig. 5.2 Temporal evolution of the dimensionless bubble size $R_* = R/R_{b0}$ excited by a single pressure wave in 3D simulation. Results of different resolutions ([64 x 32 x 32] and [32 x 16 x 16]) are compared with the analytical solution.

5.3.2 1D bubble advection

When a gas bubble streams with the same speed as the carrier fluid under no-slip motion, the exact solution to this problem is the advection of the volume fraction and mixture density at a constant speed. The numerical model should also preserve, to a high degree, the constant pressure and velocity profile along the streamline. In the dispersed Lagrangian model, there is an inconsistency between the volume fraction α_g and the mixture pressure p if the interface is advected. This is because the volume fraction is derived directly from the bubbles' sizes and locations. Indeed, the numerical oscillation induced from this inconsistency cannot be completely removed.

We consider one gas bubble inside another phase with the initial states

$$\begin{cases} (\rho, u_0, p_0, \gamma)_{\mathrm{E}}^{\mathrm{T}} = (1.0, 0.1, 1.0, 1.4)^{\mathrm{T}}, \\ (\rho, u_0, p_0, \gamma)_{\mathrm{L}}^{\mathrm{T}} = (10.0, 0.1, 1.0, 1.6)^{\mathrm{T}}, \end{cases} \tag{5.4}$$

where the subscripts E and L denote Eulerian phase and Lagrangian phase, respectively. Dimensional units are given using 1 atm and 0.1 mm. The length of the computational domain is 5.12 with a finest

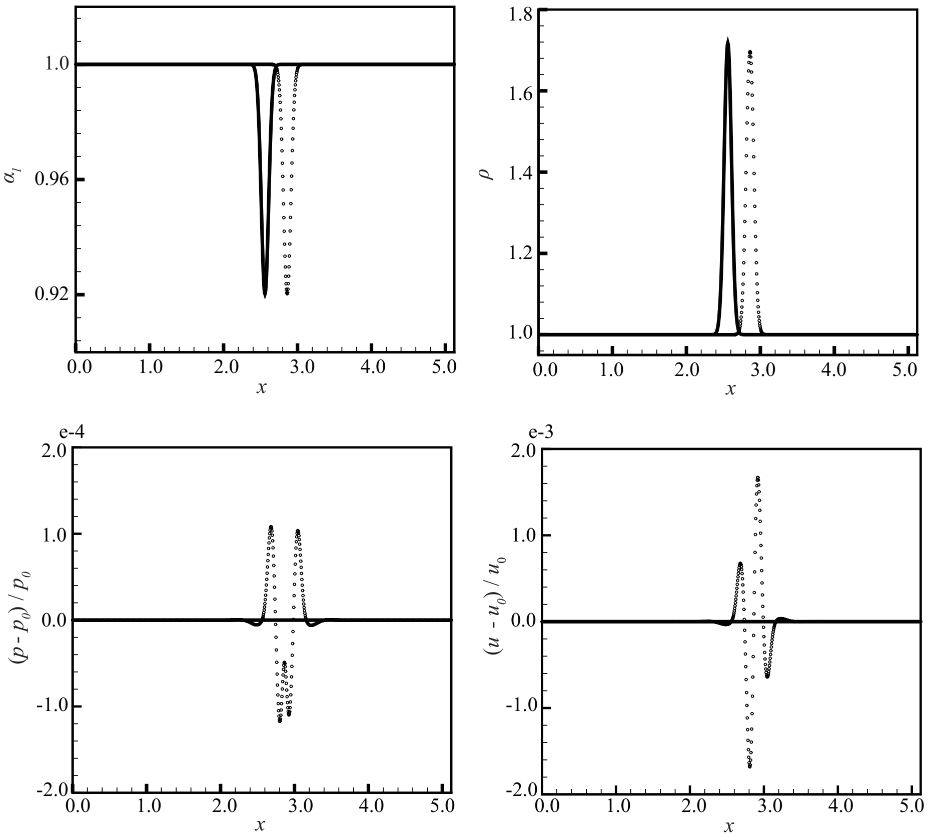

Fig. 5.3 1D advection of the gas-gas interface. The solid line represents the initial fluid condition. At $t = 0.0$, the gas bubble is at the center of the computational domain. ○: the results when the Lagrangian bubble reaches $x = 2.86$ at $t = 3.0$.

resolution of 1024. The initial Lagrangian bubble is placed at the domain center, which has an initial diameter of 0.02. The kernel width is initialized as $\sigma = 0.03$. In Fig. 5.3, the volume fraction α_l, mixture density ρ, pressure difference $(p - p_0)/p_0$, and velocity difference $(u - u_0)/u_0$ at $t = 0$ and $t = 3.0$ are shown. A numerical peak emerges after the first time-step and propagates afterwards. The normalized magnitude of the pressure and the velocity oscillation has been limited to the order of 10^{-4} and 10^{-3}, respectively. This is taken to be acceptable for later simulations.

5.3.3 Single bubble oscillating

Next, we consider a single gas bubble's oscillation in water. The bubble actively oscillates at $R = R_0(1 - \varepsilon \sin 2\pi\omega t)$, where ε is the perturbation magnitude and ω is the frequency. We set $R_0 = 100\ \mu\text{m}$, $\varepsilon = 0.1$, and $\omega = 100\,\text{kHz}$. The 1D dimension length is $L = 300R_0$. The bubble

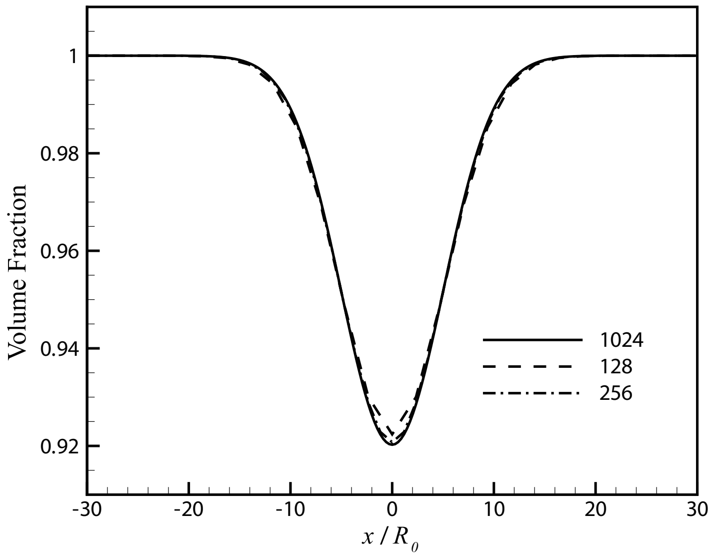

Fig. 5.4 Liquid volume fraction α_l along the bubble radius for different resolutions.

is initially located at the center of the domain. The width of the support in the Gaussian kernel is initialized as $\sigma = 6.0R_0$. Fig. 5.4 indicates the volume fraction α_l along the radial axial under three different resolutions (128, 256, and 1024). The resolution of 1024 is used for later simulations.

The bubble actively oscillates for half-period $0.5tf$; after oscillation, the volume of the bubble returns to its initial radius and remains still. In Fig. 5.5, the pressure wave along the radius axis at $t^* = tf = 0.5, 1.0, 3.0$, and 5.0 are given. The bulk fluid is first expanded, then compressed, due to the vibration of the bubble. As a result, there is a first-negative second-positive pressure wave which propagates along the radius axis. Fig. 5.6 indicates the pressure waves along the radius axis at $t^* = tf = 0.5, 1.0, 3.0$, and 5.0 of the second case, in which the bubble oscillates without pause. Pressure amplitude and frequency of the continuous pressure wave induced by the bubble's oscillation are also well resolved.

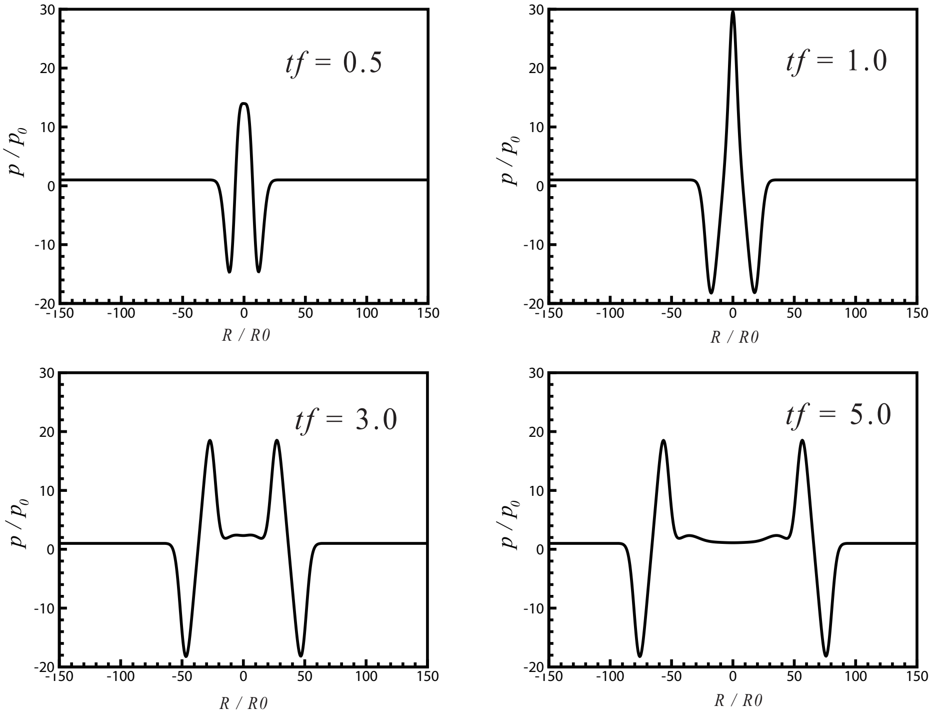

Fig. 5.5 Pressure wave induced from an oscillating gas bubble in the bulk fluid. The pressure field at $t^* = tf = 0.0, 1.0, 3.0$, and 5.0.

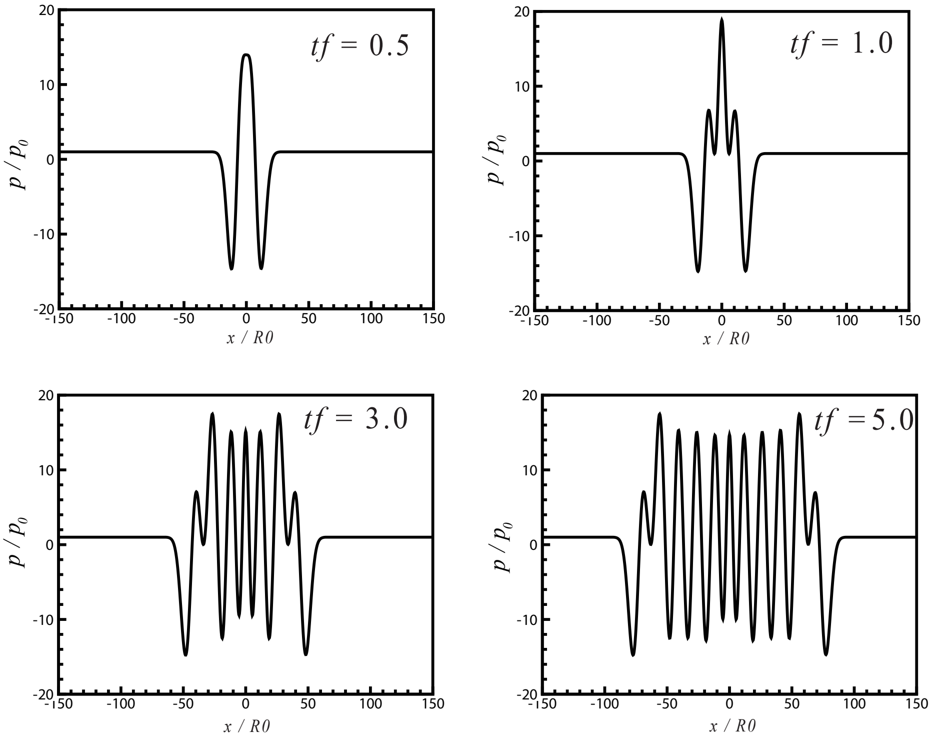

Fig. 5.6 Pressure wave propagation induced from a continuous oscillating gas bubble at $t^* = tf = 0.0, 1.0, 3.0$, and 5.0.

5.4 Application of a pressure wave traveling trough a cylindrical bubble cloud

The interaction between a cavitation bubble cloud and a pressure wave is important for many biomedical and chemical applications [80]. To better understand the transformation of a pressure wave as it passes through a bubble cloud and to analyze the acoustic pressure oscillation induced by the bubble cluster, a 2D cylindrical bubble cloud interacting with a sinusoidal pressure pulse in the fluid will be simulated. In the research from Ref. [36], the bulk fluid has low nuclei concentration, with the gas volume fraction in the order of 10^{-5} and 10^{-4}. Under the lower gas volume fraction, the shape of the pressure wave was only slightly disturbed by the dispersed bubbles [10]. In our simulation, the average gas volume fraction is larger, in the order of 10^{-3}.

As shown in Fig. 5.7, the bubble cloud, with a radius of $A_0 = 2$ mm, contains 200 gas bubbles with a random radius distribution between 1 μm and 5 μm. The sinusoidal pressure wave moving from left to right is initialized using $p = p_0 + \Delta p \sin\left(2\pi \frac{x - x_0}{\lambda}\right)$, with a wave length of $\lambda = 0.5A_0$ and a wave amplitude of $\Delta p = 15$ atm, with pressure at infinity $p_0 = 1.0$ atm. The negative pressure reaches the bubble cloud first, inducing the bubbles to expand. The initial velocity is set to zero m/s. The computational domain of $2L \times L$ ($L = 10.24$ mm) has the finest resolution of [2048 x 1024]. The kernel width for each gas bubble is initialized as $\sigma = 3.0\,\mathrm{d}x$, where d$x$ is the finest grid size. Four bubbles are marked: Bubble A (on the left side), Bubble B (on the bottom), Bubble C (at the center of the bubble cloud), and Bubble D (on the right side). They are used to analyze the influence of the pressure wave on the bubbles at different locations in the cloud.

At $t = 0$, the center of the bubble cloud is at ($0.5L$, $0.78L$) and the center of the pressure wave is at $x_0 = 0.34\,L$. The initial distribution of the gas fraction α_g, ranging from 0.0 to 0.003, is plotted with a gray scale contour in Fig. 5.7. Then, the pressure wave propagates from left to right and interacts with the bubble cluster. The pressure fields of p at 1.0 μs, 2.5 μs, 3.5 μs, 4.5 μs, and 5.5 μs are shown in Fig. 5.8. It is clear that the pressure wave reaches the bubble cluster boundary and is reflected by the cloud boundary. When the fluid has a low gas volume fraction, the shape of the pressure wave is almost unaffected [36]. In our results, the pressure wave is partially reflected, and the rest of the wave

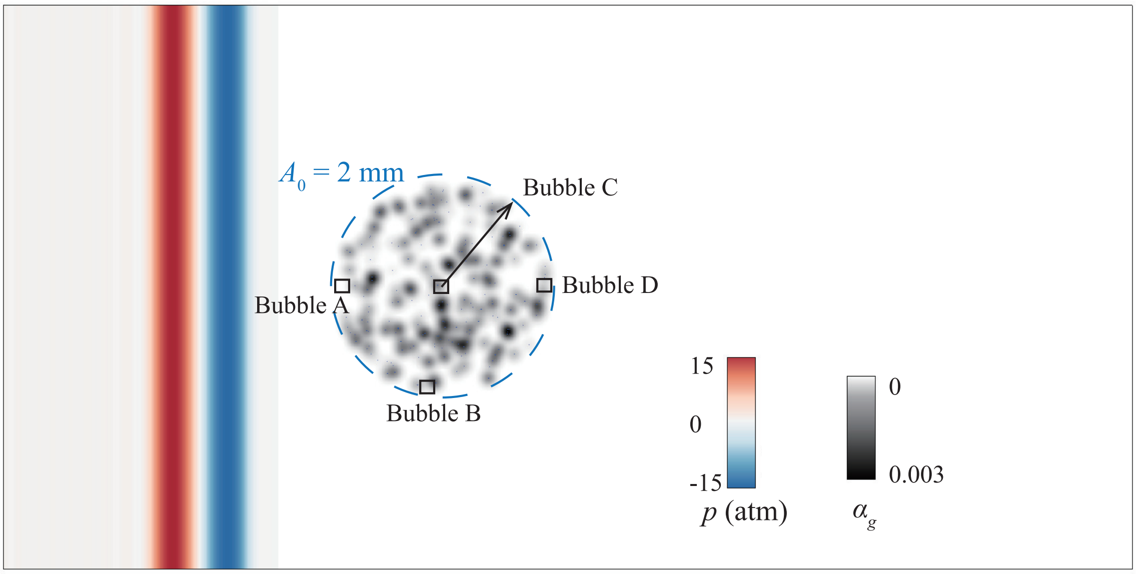
$A_0 = 2$ mm
Bubble C
Bubble D
Bubble A
Bubble B
15
0
-15
p (atm)
0
0.003
α_g

Fig. 5.7 Initial setup of the simulation of a pressure wave traveling through a bubble cloud. The radius of the bubble cloud is $A_0 = 2$ mm, and it has 200 bubbles with a random size distribution between 1 μm and 5 μm. The computation domain is $2L \times L$ ($L = 10.24$ mm). The distribution of the gas bubbles is visualized both by the volume fraction α_g and the Lagrangian spherical particles of the radius R. Four bubbles (bubbles A, B, C, and D), located at the centers of the four boxes, are marked for future reference.

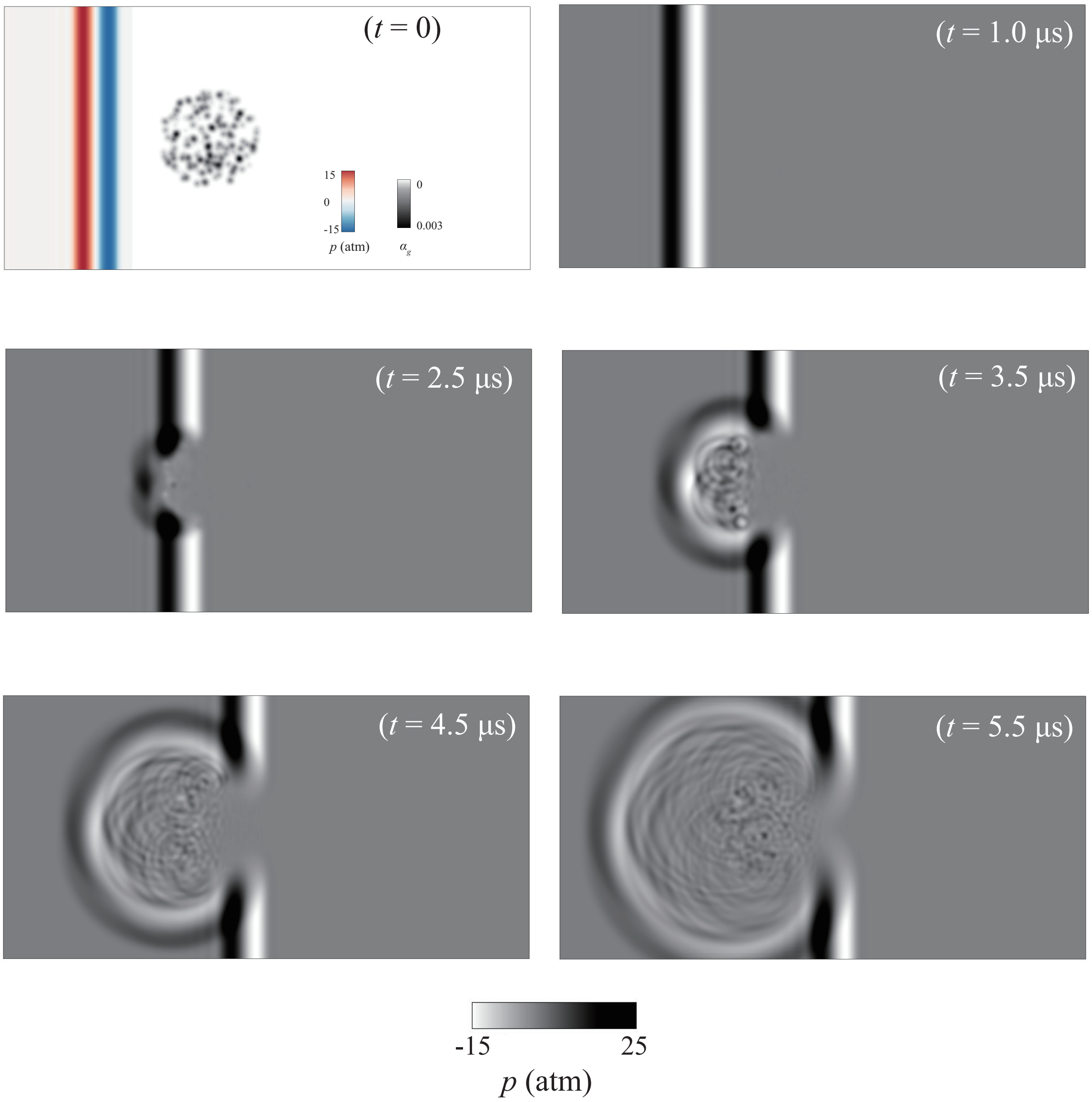

Fig. 5.8 The pressure fields induced by the bubble cluster when the bubble cluster interacts with a sinusoidal pulse. The initial state and the pressure fields at 1.0 μs, 2.5 μs, 3.5 μs, 4.5 μs, and 5.5 μs are shown.

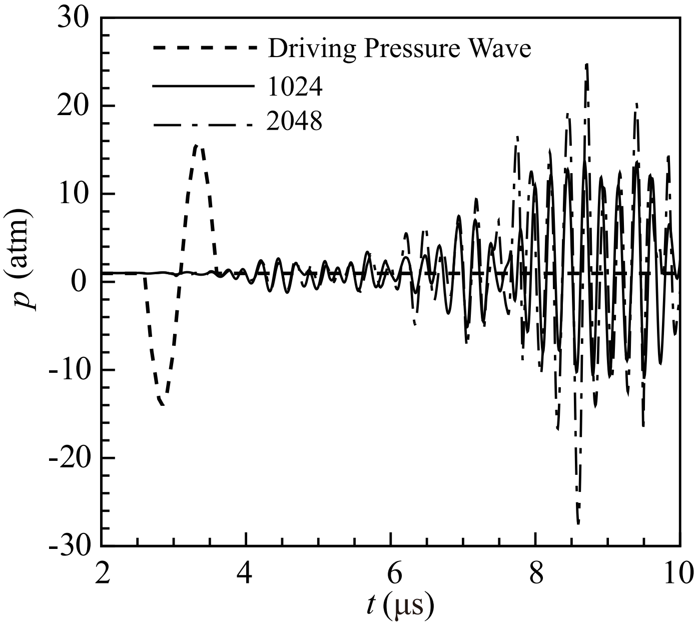

Fig. 5.9 Temporal evolution of the pressure at the bubble cloud center without (the dashed line) and with bubble cloud for two different resolutions.

travels through the cluster. The bubbles vibrate when the pressure arrives and the bubbles before the pressure wave remain in equilibrium with the bulk fluid.

As shown in Fig. 5.8, the pressure pulse inside the bulk fluid induces the bubbles' vibration; in turn, the vibration of the gas bubbles induces the pressure disturbance in the bulk fluid. The pressure p evolution at the cloud's center is plotted in Fig. 5.9. The results are shown according to two different resolutions on the x-axis. The driving pressure wave propagation in the liquid that does not have bubbles is also plotted. With a higher resolution of 2048 in x-axis, the amplitude of the pressure wave is increased, but the frequency of the pressure wave is already accurately solved in a resolution of 1024. Due to the bubbles' oscillation and the bubble-bubble interactions, the pressure at the cloud's center can reach an amplitude of 30 atm.

Meanwhile, in Fig. 5.10, the α_g at 1.5 μs, 2.0 μs, 2.5 μs, 3.0 μs, 3.5 μs, and 4.5 μs are plotted. A larger gas volume fraction should be achieved when the bubbles are approached by negative pressure, since the bubbles would expand. Instead, overpressurization compresses the bubbles, indicating a smaller value of α_g. As the pressure wave is partially reflected at the cluster's boundary, there is no major change in the volume fraction at the cloud's center. To better understand the pressure wave's

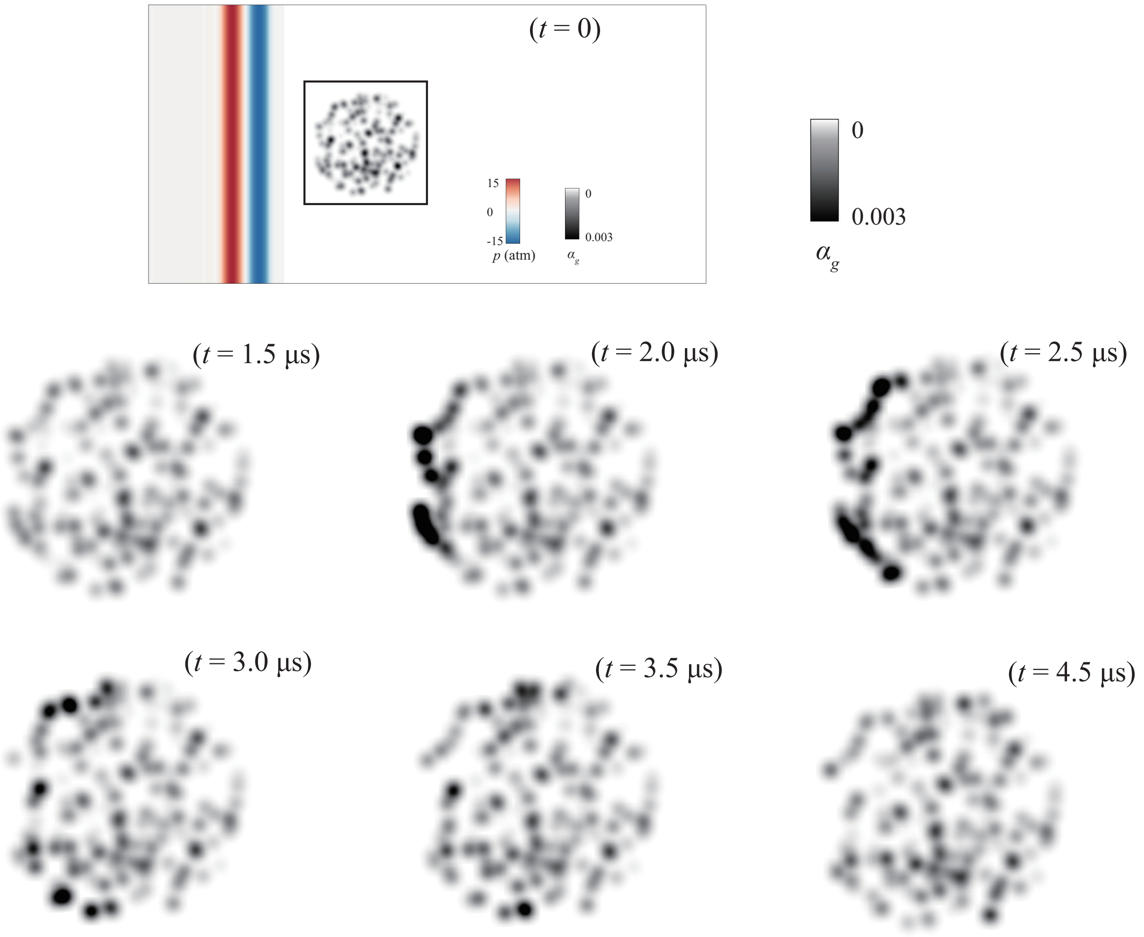

Fig. 5.10 Plots of α_g when the bubble cluster interacts with a sinusoidal pulse at 1.5 μs, 2.0 μs, 2.5 μs, 3.0 μs, 3.5 μs, and 4.5 μs.

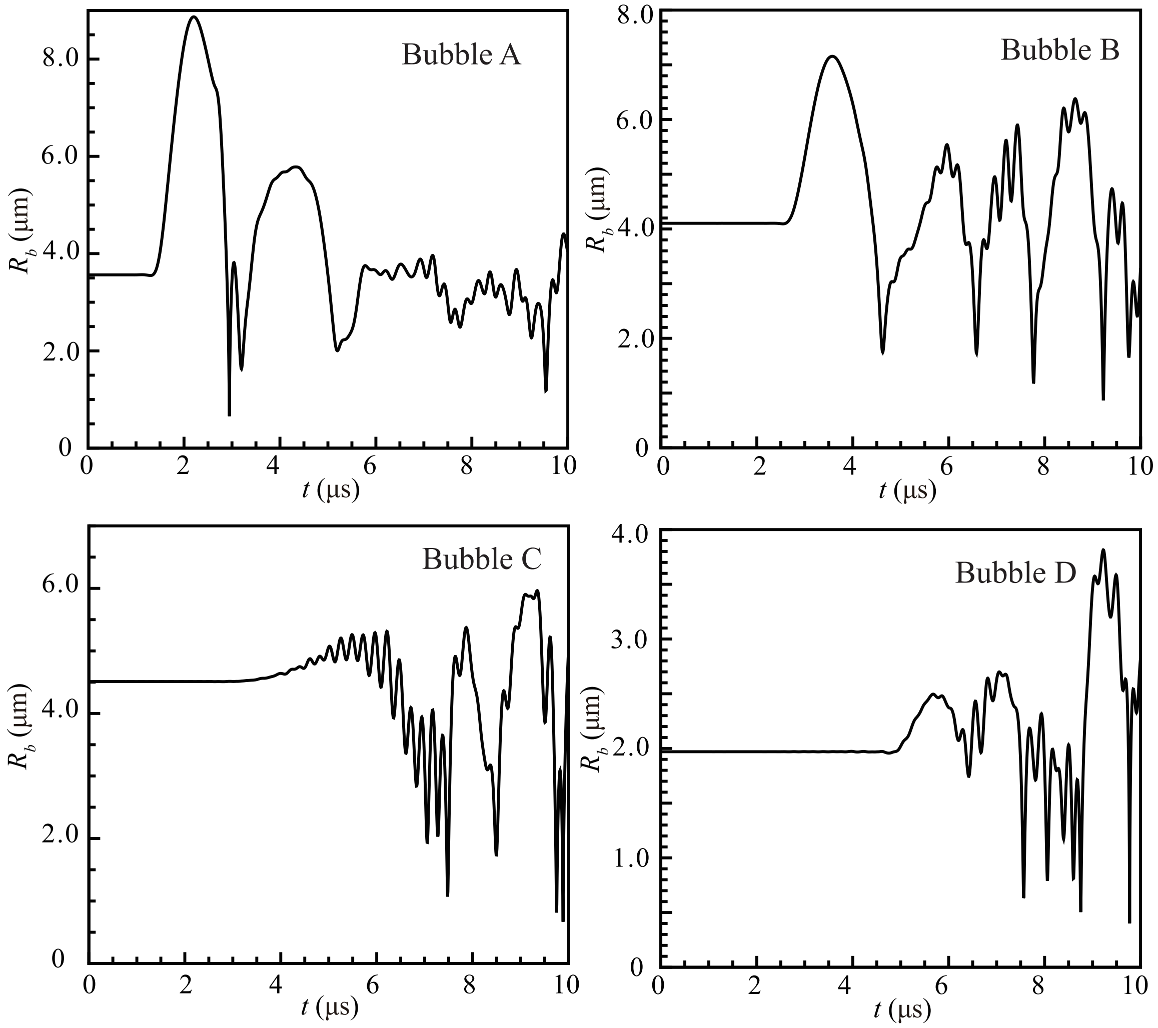

Fig. 5.11 Evolution of bubble radius R of Bubble A - D.

influence on the α_g, the time evolutions of radii for Bubbles A–D are plotted in Fig. 5.11. From Fig. 5.11, it's clear that the bubbles' radii are constant before the arrival of the pressure wave, which means the bubbles are in equilibrium with the carrier fluid. The negative pressure first reaches Bubble A, causing Bubble A to violently expand. This corresponds well with the larger volume fraction field at $t = 2.0$ μs in Fig. 5.10. The positive pressure wave that follows then condenses Bubble A; thus, the bubble becomes unstable, actively oscillating as a result. Similarly, Bubble B expands at first, then shrinks, and finishes by actively oscillating. However, Bubble C (at the cloud's center) and Bubble D (on the right) demonstrate no obvious expansion when the pressure wave arrives. This also corresponds well with the volume fraction field at $t = 3.0$ μs, 3.5 μs, and 4.5 μs in Fig. 5.10. As shown in Fig. 5.8, the pressure wave is reflected at the interface and absorbed; only a small amount of pressure successfully passes through the bubble cloud. In the end, all four bubbles actively oscillate as a result of the pressure wave until they return to a state of equilibrium with the carrier fluid.

5.5 3D Rayleigh collapse of a bubble cloud

5.5.1 Rayleigh collapse

The Rayleigh collapse is a typical transient behavior when a bubble passes through a rigid channel. It is considered to be the main reason for the erosion of rigid channels. Overpressurization from the background fluid results in the bubble's collapse. If the viscous effects and the surface tension are neglected, the temporal evolution of a spherical vapor bubble can be described by the equation

$$R\ddot{R} + \frac{3}{2}\dot{R}^2 = \frac{p_v - p_\infty}{\rho}. \tag{5.5}$$

The Rayleigh time, which is the approximate average collapse time for a single bubble, is

$$t_{\text{Rayleigh}} = 0.915 R_0 \sqrt{\frac{\rho}{p_\infty - p_v}}. \tag{5.6}$$

5.5.2 Results and discussions

A schematic of the initial setup is shown in Fig. 5.12. First, the spherical bubble cluster with N_0 = 200 spherical bubbles is placed into still water, the radii of which are initially randomly distributed between 100μm and 500μm. The average bubble radius is 308μm. The radius of the bubble cluster is $A_0 = 7.5$ mm. The 3D domain size is 25.6 mm × 25.6 mm × 25.6 mm, and the finest level of resolution is [256 × 256 × 256]. The center of the bubble cluster coincides with the center of the computational domain. All boundary conditions are outflow conditions. The velocity field is initialized as zero m/s and the temperature remains at 293 K. The viscosity and the non-condensible gas inside the bubbles is neglected. All the bubbles are vapor bubbles and the vapor pressure remains constant ($p_v = 2430$ pa). The initial bulk fluid overpressure is p_∞ = 10.0 atm. The initial, strong over-pressure induces the violent collapse of the cloud. To minimize the cost of computation, bubbles with an extremely small volume are marked "inactive," to signify their collapse, and the Lagrangian computation of the inactive bubbles will be terminated. Thus, in our collapse simulation, the cloud rebound will not be considered. The collapse time here refers to the time at which the bubble cloud meets the first collapse point. For the coupling scheme, the width of the Gaussian kernel function is initialized as $\sigma_0 = 6.0\,\mathrm{d}x$. Fig. 5.13 shows the iso-surfaces of the volume fraction $\alpha_g = 0.002$ (i.e. $\alpha_l = 0.998$) at six different points in time (t = 0 μs, 6 μs, 9 μs, 12 μs, 14 μs, and 16 μs). Meanwhile, the vapor bubbles are plotted in Fig. 5.13, which indicate the location and the volume of the bubbles. The collapse process happens non-symmetrically from outside to inside. At the beginning of the process until around t = 9 μs, the cloud collapses slowly. After that point, the rate of collapse increases considerably, and the bubble cloud collapse violently between 14 μs and 16 μs. The collapse qualitatively agrees with the first collapse of the simulation result in Ref. [31].

During the collapse, extremely high pressures are generated from the center of the bubble cloud. In Fig. 5.13, the slices of higher pressure region (the region greater than 10 atm) are plotted at each time instant. The higher pressure increases over time. At the end of the collapsing process, the extreme pressure reaches its maximum value of approximately 174 atm at the same time that the collapse rate reaches its maximum value. In Fig. 5.14, revolutions of the dimensionless active bubble

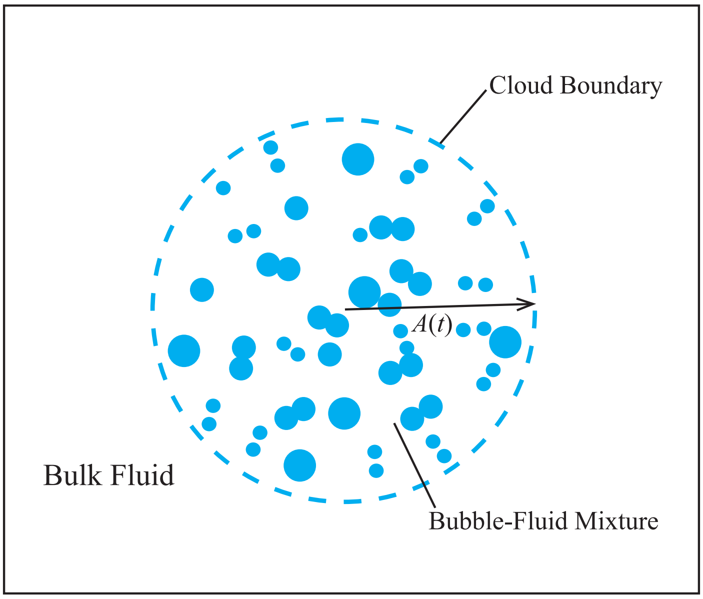

Fig. 5.12 Schematic of setup of the bubble cloud's Rayleigh Collapse. A spherical bubble cloud with N_0 vapor bubbles is submerged; $A(t)$ indicates the bubble cloud's radius.

number N_b/N_0 and the dimensionless averaged gas fraction β/β_0 ($\beta = \Sigma_{V_c}\alpha_g/V_c$) are shown. The vapor cloud collapse completely at about t = 14.5 μs.

To analyze the influence of the bubble initial number N_0 on the cloud's collapse time, we simulate N_0 = 300 and 400 under the same initial conditions as above. Fig. 5.15 and Fig. 5.16 provide snapshots of the collapse process at t = 0 μs, 6 μs, 9 μs, 12 μs, 13 μs, and 14 μs. In Fig. 5.17, the time changes of N_b/N_0 (N_0 = 400) and β/β_0 are shown. We can see, similar to N_0 = 200 in Fig. 5.14, that the collapse time of the bubble cloud with N_0 = 300/400 is also at around 14.5 μs. However, the larger bubble number induces greater pressure at the cloud's center. For N_0 = 300, the maximum pressure is roughly 226 MPa. For N_0 = 400, the maximum pressure is roughly 313 MPa. For the bubble cloud with N_0 = 400, the distribution of bubble radii during the collapse is analyzed according to their sizes. Fig. 5.18 shows the bubble size density distribution at t = 0 μs, 6 μs, 9 μs, 12 μs, 13 μs, and 14 μs. The first bar on the left indicates the density of the collapsed (inactive) vapor bubbles. Fig. 5.18 shows that the vapor bubbles become compressed all together due to the higher environmental pressure. As indicated in Eq. (5.6), as a bubble radius increases, its collapse time t_{Rayleigh} also increases. For a bubble cloud, we find there are two factors affecting the final collapse time: the bubble size distribution and the initial overpressurization. In the three above conditions of

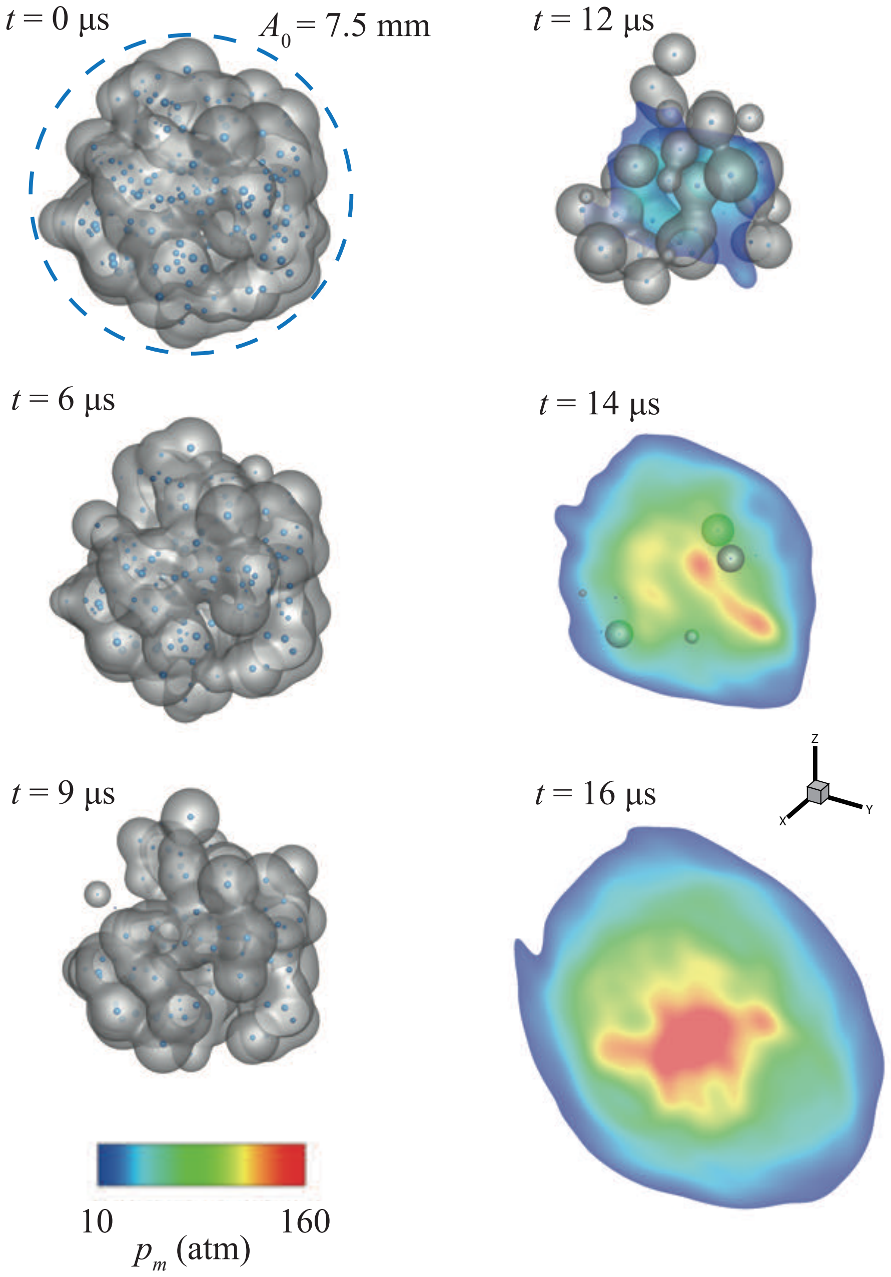

Fig. 5.13 Snapshots of the collapsing process of a bubble cloud with N_0 = 200 vapor bubbles (at t = 0 μs, 6 μs, 9 μs, 12 μs, 14 μs, and 16 μs). The distribution of the vapor bubbles is visualized both by the iso-surfaces of the volume fraction $\alpha_g = 0.002$ ($\alpha_l = 0.998$) and the Lagrangian spherical particles of the radius R. Cut-sections of the high pressure area (higher than 10 atm) at the center of the bubble cloud are also plotted, which indicate that the cloud's collapse induced violent pressures.

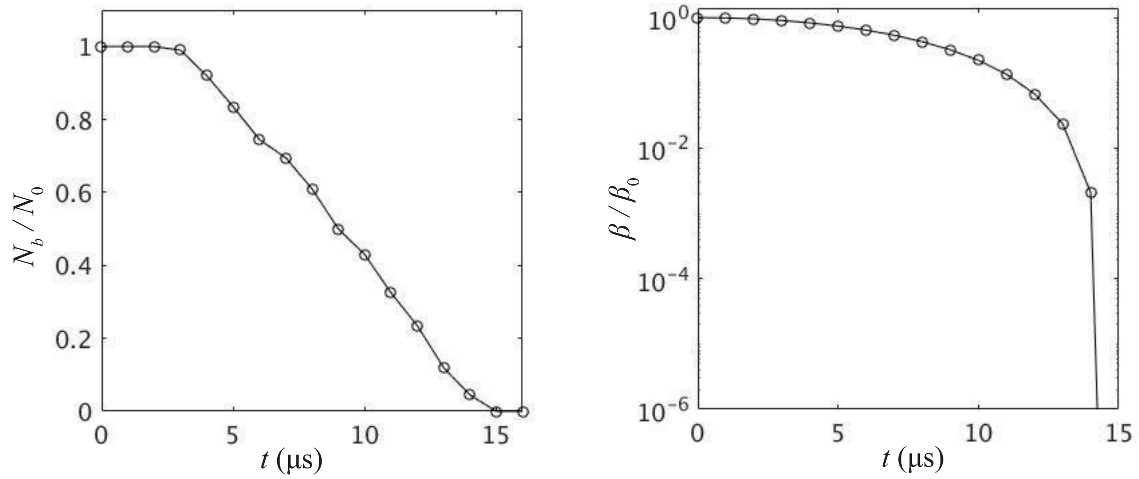

Fig. 5.14 Time change of the non-dimensional active bubble number N_b/N_0 (N_0 = 200) and the average gas fraction β/β_0, here $\beta = \Sigma_{V_c}\alpha_g/V_c$.

different initial bubble numbers, bubbles in the cloud follow the same initial size distribution, which means that the average bubble radii are same. When the bubble radius distribution keeps unchanged, the number of bubbles inside the cloud has no significant influence on the time instant when the cloud finally collapses; even the higher number of bubbles increases the average vapor volume fraction $\beta = \Sigma_{V_c}\alpha_g/V_c$. However, the larger bubble number induces greater pressure at the cloud's center because of a larger vapor void.

5.6 Summary

The LE two-way coupling model offers simultaneous simulations of the cavitating fluid and allows the tracking of the cavitation bubbles. Benchmark simulations were designed to validate this method in both 1D and 3D. This model was applied to simulate the pressure wave that traveled through a cylindrical bubble cloud. The pressure pulse inside the cavitation fluid induced the bubbles' vibration; conversely, the gas bubbles' vibration induced the pressure disturbances. The pressure wave induced by the oscillating bubbles was effectively predicted using this method. The shape of the pressure pulse in the fluid significantly changed as a result of the reflection at the cloud's boundary and the bubbles' oscillation when the gas void fraction was in the scale of 10^{-3}. In the 3D simulation of Rayleigh

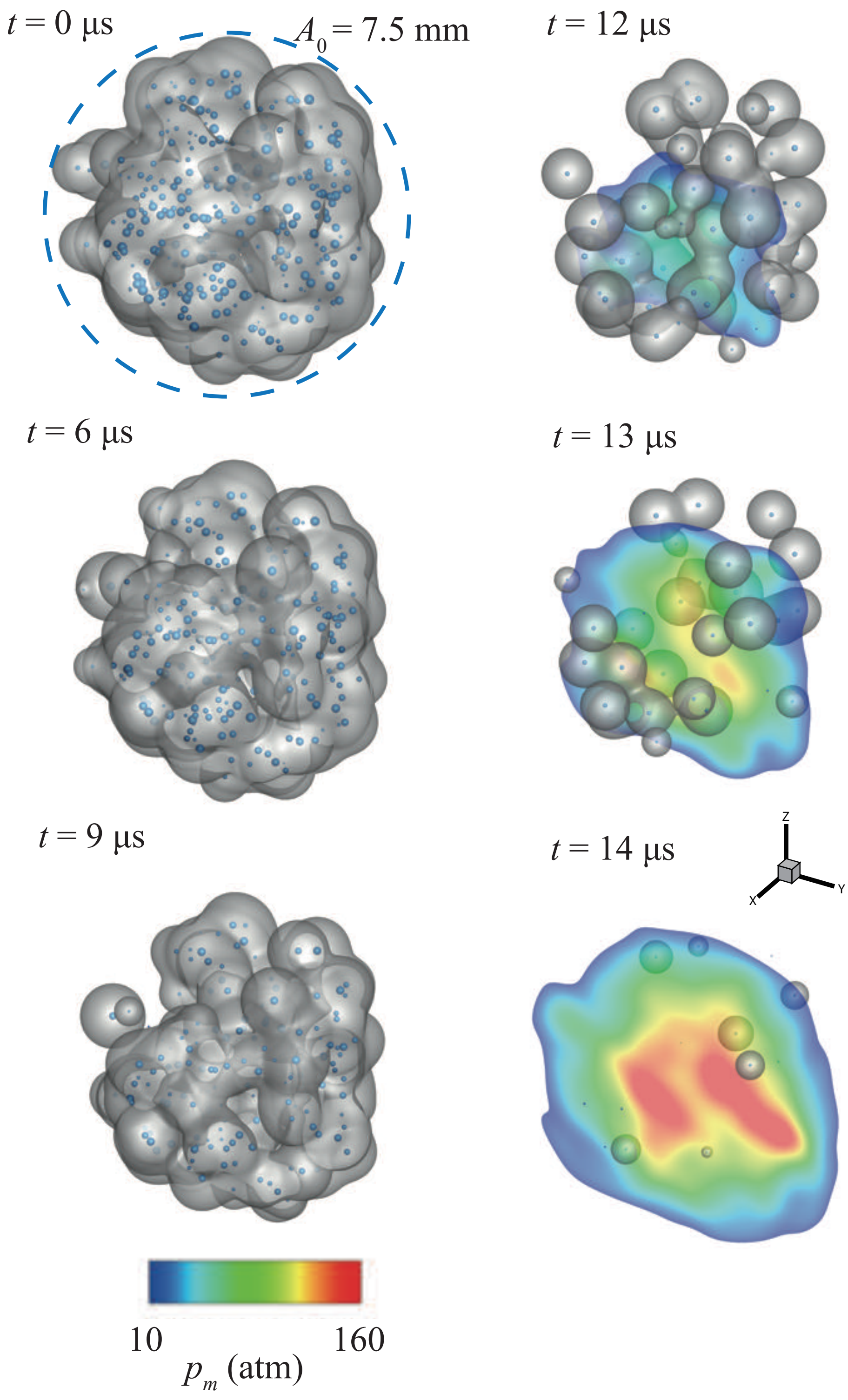

Fig. 5.15 Snapshots of the vapor bubble cloud collapse process with $N_0 = 300$ vapor bubbles ($t = 0$ μs, 6 μs, 9 μs, 12 μs, 13 μs, and 14 μs). Distribution of the vapor bubbles is visualized both by the iso-surfaces of the volume fraction $\alpha_g = 0.002$ ($\alpha_l = 0.998$) and the Lagrangian spherical particles of the radius R. Cut-sections of the extreme pressure area (higher than 10 atm) at the center of the bubble cloud are also plotted, which indicate the cloud collapse induced violent pressure.

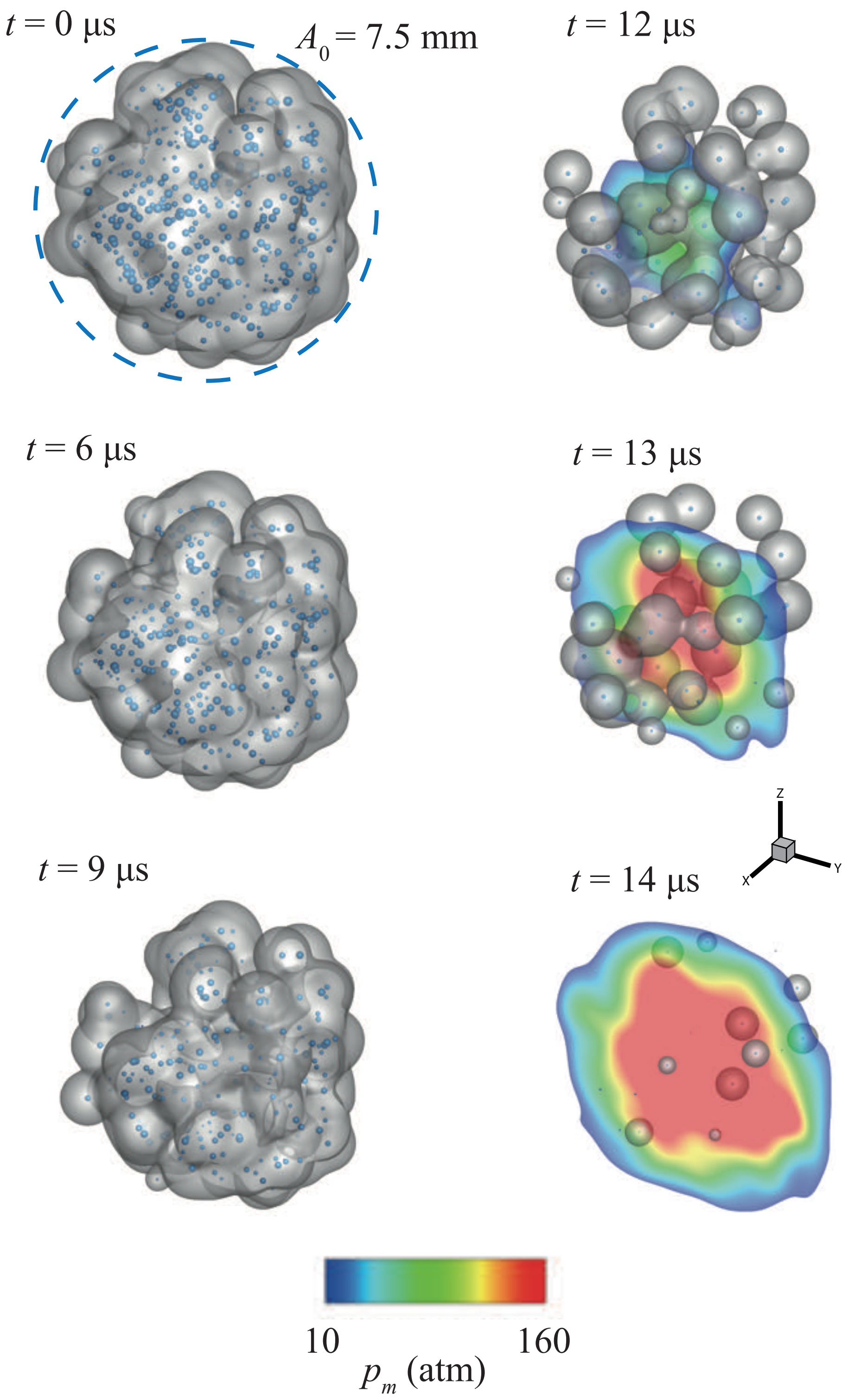
t = 0 μs
A0 = 7.5 mm
t = 12 μs
t = 6 μs
t = 13 μs
t = 9 μs
t = 14 μs
Z
X
Y
10
160
pm (atm)

Fig. 5.16 Snapshots of the vapor bubble cloud collapse process initially with $N_0 = 400$ vapor bubbles ($t = 0\ \mu$s, 6 μs, 9 μs, 12 μs, 13 μs, and 14 μs). Distribution of the vapor bubbles is visualized both by the iso-surface of the volume fraction $\alpha_g = 0.002$ ($\alpha_l = 0.998$) and the Lagrangian spherical particles of the radius R. Slices of the high pressure area (higher than 10 atm) at the center of the bubble cloud are also plotted, which indicate the cloud collapse induced violent pressure.

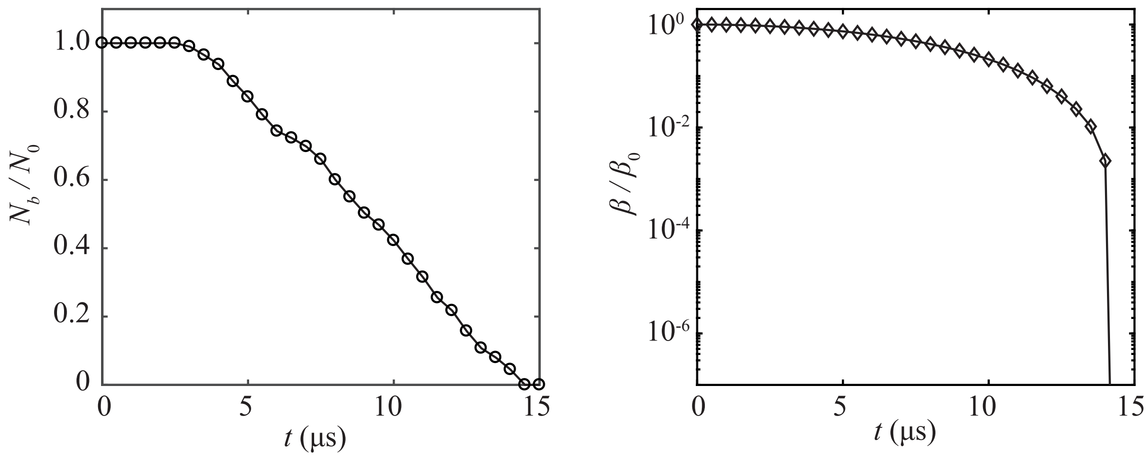

Fig. 5.17 Time change of the non-dimensional active bubble number N_b/N_0 (N_0 = 400) and the averaged gas fraction β/β_0 ($\beta = \Sigma_{V_c}\alpha_g/V_c$).

collapse of a bubble cloud, the number of bubbles comprising the cloud has no significant influence on the cloud's final collapse time if the bubble size distribution keeps the same. However, the larger number of bubbles causes the averaged vapor volume fraction to become much higher, thus inducing more violent, higher pressures.

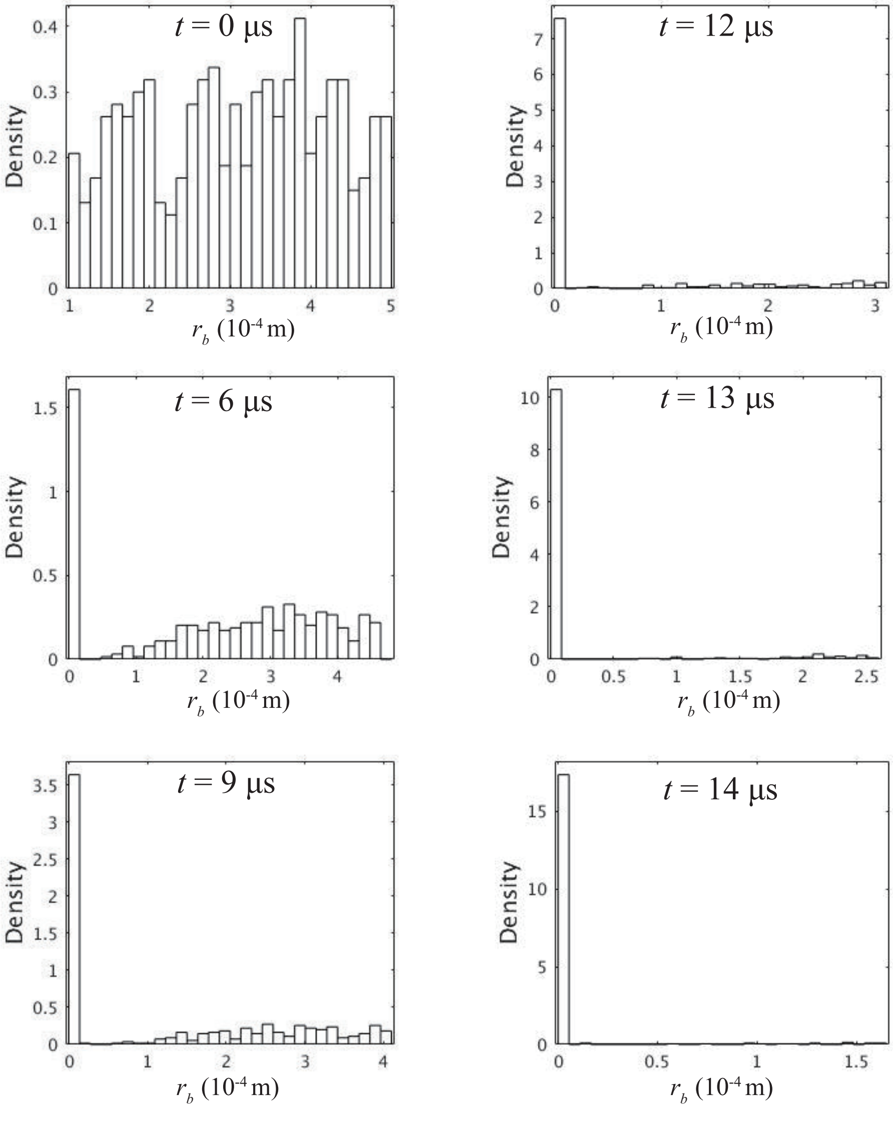

Fig. 5.18 The bubble distributions (radii density bar graphs) of the bubbles' radii at $t = 0$ μs, 6 μs, 9 μs, 12 μs, 13 μs, and 14 μs. The first bar on the left indicates the density of the collapsed vapor bubbles.

Chapter 6

Summary and conclusion

In recent years, dynamics of cavitation bubbles have been studied with the aim of reducing the destructive damage they cause in many engineering applications, for example erosions on the propellers [61, 108]. Cavitation bubble clouds can also be applied as a means to increase treatment efficiency when they are introduced as vehicles of medicine or drug delivery. A numerical study of cavitation offers the solution of the fluid in micro time- and space- scales to better detect the behaviors of the cavitation bubble cloud. In this thesis, flow cavitation was investigated using the LE coupling model with a particular focus on tracking the cavitation bubbles via Lagrangian tracking [23, 74, 111]. This model was developed to study the applications of cavitation flow (i.e., the homogeneous cavitation nucleation inside a microchannel, a cavitation bubble cloud and a sinusoidal pressure wave interaction, and the bubble cloud undergoes Rayleigh collapse).

In our model, the cavitation fluid is assumed to be a compressible fluid containing initially dispersed gas bubbles with radii ranging from several micrometers to millimeters in length. The LE model's complete system includes the Eulerian formulation of the cavitation fluid, Lagrangian tracking of each individual cavitation bubble, and an LE coupling scheme. Assuming that the fluid inside each computational cell is homogeneous and in equilibrium and that each computational cell has only one velocity and one pressure measurement, the governing equations of the Eulerian fluid follow the conservation law. To close the system, EOS or an isobaric closure is applied. All the bubbles are quite small, so we assume the surface tension is significant enough to maintain their spherical form. Thus, they are treated as dispersed Lagrangian particles, the dynamics of which are modeled by the spherical bubble dynamics equation, which considers the properties of the surrounding fluid. Also the bubble dynamic equation models how the carrier fluid influences the dispersed bubbles. Through two-way coupling, the bubbles barely affect the velocity or the momentum of the carrier liquid; however, they play a fundamental role in modeling the gas volume fraction and the pressure closure. The gas/vapor volume fraction is derived based on a Gaussian kernel function, which smoothens out the volume fraction and diffuses the isolated interfaces to prevent numerical oscillation. An isobaric closure is applied to derive the mixture's equilibrium pressure [1, 4].

First, we applied the LE one-way coupling model to simulate the homogeneous nucleation in a microchannel induced by shock-bubble interactions. A novel computational scheme for creating homogeneous cavitation nucleation was proposed applying the modified nucleation rate formula proposed by Blander and Katz [16], which provides a more accurate nucleation rate than does the classical nucleation theory. This scheme consists of four parts: Eulerian computation, bubble growth simulation, nucleation rate calculation, and bubble initialization. The two-dimensional axisymmetric two-phase equations were solved to compute gas bubble and bulk fluid evolution in the microchannel. Homogeneous nucleation within the microchannel was completed in three stages: the energy deposition stage, the nucleus generation stage, and the nucleus growth stage. The total nucleus number and nucleus distributions at different stages have been analyzed. We found that the nucleus cluster distributions fit well with a two-parameter Weibull probability density function, and the modified classical nucleation theory can model the homogeneous nucleation rate very effectively. Homogeneous nucleation is a result of the negative pressure-induced energy deposition rate and nuclei growth rate. The absolute minimum pressure at which nucleation can occur in a microchannel is about -76.0 MPa. In the end, simulations using different initial shock amplitudes were presented, through which we found that shock intensity has no significant influence on the time instant when the first nucleus is generated. However, larger shock intensities significantly increase the final total number of nuclei due to the larger energy deposition that results during the first stage of nucleation.

The LE two-way coupling scheme was developed based on our multi-resolution Eulerian solver. The gas volume fraction was modeled as a formulation of the sizes and locations of the gas bubbles. Benchmark simulations were used to validate our method in 1D and 3D contexts. The simulation of a cylindrical bubble cloud interacting with a pressure wave was carried out as one type of application.

The pressure pulse induced active bubble vibration, and this vibration induced pressure perturbation inside fluid. The pressure field induced by oscillating bubbles was effectively predicted by our method. We found that the shape of the pressure pulse significantly changes after it passes through the bubble cloud due to the reflection at the cloud's boundary and at the sub-grid interfaces. This finding differed from the results of the simulations in which the gas volume fraction is in the scale of 10^{-4} in Ref. [10, 36] because we have a larger gas volume fraction of 10^{-3}. In the end, we applied this model to simulate a 3D bubble cluster Rayleigh collapse. The number of bubbles inside the cloud has no notable influence on the cloud's final collapse time when the average bubble radius remains the same. With the average volume fraction increases, the extreme pressure induced from bubble collapse increases.

As a suggestion for potential future studies, a direct 3D simulation of homogeneous nucleation based on the LE two-way coupling model is proposed; this will offer a more accurate modeling of the nucleation process and an comparison with the LE one-way coupling model. Also, bubbly flow turbulence could be an important topic of investigation for future studies. Dispersed multiphase flows are often turbulent. In both experimental measurements and numerical simulations, the presence of dispersed bubbles increases the complexity of turbulence more significantly than a single phase turbulence does. At the same time, the influence of carrier phase turbulence on dispersed bubbles can be notable. Thus, improved LE models and bubble dynamics models that account for multiple factors are in high demand.

References

[1] Abgrall, R. (1996). How to prevent pressure oscillations in multicomponent flow calculations: a quasi conservative approach. *Journal of Computational Physics*, 125(1):150–160.

[2] Adams, N. A. and Schmidt, S. J. (2013). Shocks in cavitating flows. *Bubble dynamics and shock waves*, pages 235–256.

[3] Alehossein, H. and Qin, Z. (2007). Numerical analysis of rayleigh-plesset equation for cavitating water jets. *International Journal for Numerical Methods in Engineering*, 72(7):780–807.

[4] Allaire, G., Clerc, S., and Kokh, S. (2002). A five-equation model for the simulation of interfaces between compressible fluids. *Journal of Computational Physics*, 181(2):577–616.

[5] Amsden, A. A., Butler, T. D., and O'Rourke, P. J. (1987). The kiva-ii computer program for transient multidimensional chemically reactive flows with sprays. *SAE transactions*, pages 373–383.

[6] Ando, K., Colonius, T., and Brennen, C. E. (2011). Numerical simulation of shock propagation in a polydisperse bubbly liquid. *International Journal of Multiphase Flow*, 37(6):596–608.

[7] Ando, K., Liu, A. Q., and Ohl, C. D. (2012). Homogeneous nucleation in water in microfluidic channels. *Physical review letters*, 109(4):044501.

[8] Angélil, R., Diemand, J., Tanaka, K. K., and Tanaka, H. (2014). Bubble evolution and properties in homogeneous nucleation simulations. *Physical review E*, 90(6):063301.

[9] Apte, S. V., Mahesh, K., Moin, P., and Oefelein, J. C. (2003). Large-eddy simulation of swirling particle-laden flows in a coaxial-jet combustor. *International Journal of Multiphase Flow*, 29(8):1311–1331.

[10] Arora, M., Ohl, C.-D., and Lohse, D. (2007). Effect of nuclei concentration on cavitation cluster dynamics. *The Journal of the Acoustical Society of America*, 121(6):3432–3436.

[11] Ashokkumar, M. (2011). The characterization of acoustic cavitation bubbles–an overview. *Ultrasonics sonochemistry*, 18(4):864–872.

[12] Auton, T., Hunt, J., and Prud'Homme, M. (1988). The force exerted on a body in inviscid unsteady non-uniform rotational flow. *Journal of Fluid Mechanics*, 197:241–257.

[13] Avvaru, B. and Pandit, A. B. (2009). Oscillating bubble concentration and its size distribution using acoustic emission spectra. *Ultrasonics sonochemistry*, 16(1):105–115.

[14] Balachandar, S. and Eaton, J. K. (2010). Turbulent dispersed multiphase flow. *Annual Review of Fluid Mechanics*, 42:111–133.

[15] Batten, P., Clarke, N., Lambert, C., and Causon, D. M. (1997). On the choice of wavespeeds for the hllc riemann solver. *SIAM Journal on Scientific Computing*, 18(6):1553–1570.

[16] Blander, M. and Katz, J. L. (1975). Bubble nucleation in liquids. *AIChE Journal*, 21(5):833–848.

[17] Brennen, C. E. (2013). *Cavitation and bubble dynamics*. Cambridge University Press.

[18] Caflisch, R. E., Miksis, M. J., Papanicolaou, G. C., and Ting, L. (1985). Effective equations for wave propagation in bubbly liquids. *Journal of Fluid Mechanics*, 153:259–273.

[19] Calzavarini, E., Kerscher, M., Lohse, D., and Toschi, F. (2008). Dimensionality and morphology of particle and bubble clusters in turbulent flow. *Journal of Fluid Mechanics*, 607:13–24.

[20] Castro, M., Costa, B., and Don, W. S. (2011). High order weighted essentially non-oscillatory weno-z schemes for hyperbolic conservation laws. *J. Comput. Phys.*, 230:1766–1792.

[21] Caupin, F. and Herbert, E. (2006). Cavitation in water: a review. *Comptes Rendus Physique*, 7(9):1000–1017.

[22] Courant, R., Friedrichs, K., and Lewy, H. (1967). On the partial difference equations of mathematical physics. *IBM journal*, 11(2):215–234.

[23] Coussios, C. C. and Roy, R. A. (2008). Applications of acoustics and cavitation to noninvasive therapy and drug delivery. *Annu. Rev. Fluid Mech.*, 40:395–420.

[24] Darmana, D., Deen, N. G., and Kuipers, J. (2006). Parallelization of an euler–lagrange model using mixed domain decomposition and a mirror domain technique: Application to dispersed gas–liquid two-phase flow. *Journal of Computational Physics*, 220(1):216–248.

[25] Darmana, D., Deen, N. G., and Kuipers, J. A. M. (2005). Detailed modeling of hydrodynamics, mass transfer and chemical reactions in a bubble column using a discrete bubble model. *Chemical Engineering Science*, 60(12):3383–3404.

[26] Debenedetti, P. G. (1996). *Metastable liquids: concepts and principles*. Princeton University Press.

[27] Delale, C. F., Hruby, J., and Marsik, F. (2003). Homogeneous bubble nucleation in liquids: The classical theory revisited. *The Journal of chemical physics*, 118(2):792–806.

[28] Delale, C. F., Nas, S., and Tryggvason, G. (2005). Direct numerical simulations of shock propagation in bubbly liquids. *Physics of Fluids (1994-present)*, 17(12):121705.

[29] Delnoij, E., Lammers, F., Kuipers, J., and Van Swaaij, W. (1997). Dynamic simulation of dispersed gas-liquid two-phase flow using a discrete bubble model. *Chemical Engineering Science*, 52(9):1429–1458.

[30] Diemand, J., Angélil, R., Tanaka, K. K., and Tanaka, H. (2014). Direct simulations of homogeneous bubble nucleation: Agreement with classical nucleation theory and no local hot spots. *Physical review E*, 90(5):052407.

[31] Egerer, C. P., Schmidt, S. J., Hickel, S., and Adams, N. A. (2016). Efficient implicit les method for the simulation of turbulent cavitating flows. *Journal of Computational Physics*, 316:453–469.

[32] Elghobashi, S. and Truesdell, G. (1992). Direct simulation of particle dispersion in a decaying isotropic turbulence. *Journal of Fluid Mechanics*, 242:655–700.

[33] Felton, K. and Loth, E. (2001). Spherical bubble motion in a turbulent boundary layer. *Physics of Fluids*, 13(9):2564–2577.

[34] Ford, B. and Loth, E. (1998). Forces on ellipsoidal bubbles in a turbulent shear layer. *Physics of Fluids*, 10(1):178–188.

[35] Frenkel, Y. I. (1955). *Kinetic theory of liquids*. Dover.

[36] Fuster, D. and Colonius, T. (2011). Modelling bubble clusters in compressible liquids. *Journal of Fluid Mechanics*, 688:352–389.

[37] Gavaises, M. (2008). Flow in valve covered orifice nozzles with cylindrical and tapered holes and link to cavitation erosion and engine exhaust emissions. *International Journal of Engine Research*, 9(6):435–447.

[38] Gavaises, M., Papoulias, D., Andriotis, A., Giannadakis, E., and Theodorakakos, A. (2007). Link between cavitation development and erosion damage in diesel injector nozzles. Technical report, SAE Technical Paper.

[39] Gorokhovski, M. and Herrmann, M. (2008). Modeling primary atomization. *Annu. Rev. Fluid Mech.*, 40:343–366.

[40] Gottlieb, S., Shu, C.-W., and Tadmor, E. (2001). Strong stability-preserving high-order time discretization methods. *SIAM review*, 43(1):89–112.

[41] Gueyffier, D., Li, J., Nadim, A., Scardovelli, R., and Zaleski, S. (1999). Volume-of-fluid interface tracking with smoothed surface stress methods for three-dimensional flows. *Journal of Computational Physics*, 152(2):423–456.

[42] Han, L. H., Hu, X. Y., and Adams, N. A. (2014). Adaptive multi-resolution method for compressible multi-phase flows with sharp interface model and pyramid data structure. *Journal of Computational Physics*, 262:131–152.

[43] Harten, A., Engquist, B., Osher, S., and Chakravarthy, S. R. (1987). Uniformly high order accurate essentially non-oscillatory schemes, iii. *J. Comput. Phys.*, 71:231–303.

[44] Harten, A., Lax, P. D., and Leer, B. v. (1983). On upstream differencing and godunov-type schemes for hyperbolic conservation laws. *SIAM review*, 25(1):35–61.

[45] Hauptmann, M., Struyf, H., De Gendt, S., Glorieux, C., and Brems, S. (2013). Evaluation and interpretation of bubble size distributions in pulsed megasonic fields. *Journal of Applied Physics*, 113(18):184902.

[46] Herbert, E., Balibar, S., and Caupin, F. (2006). Cavitation pressure in water. *Physical Review E*, 74(4):041603.

[47] Hirt, C. W. and Nichols, B. D. (1981). Volume of fluid (vof) method for the dynamics of free boundaries. *Journal of computational physics*, 39(1):201–225.

[48] Hsiao, C.-T., Ma, J., and Chahine, G. L. (2017). Multiscale tow-phase flow modeling of sheet and cloud cavitation. *International Journal of Multiphase Flow*, 90:102–117.

[49] Hu, X. Y. and Adams, N. A. (2006). A multi-phase sph method for macroscopic and mesoscopic flows. *Journal of Computational Physics*, 213(2):844–861.

[50] Hu, X. Y., Khoo, B. C., Adams, N. A., and Huang, F. L. (2006). A conservative interface method for compressible flows. *Journal of Computational Physics*, 219(2):553–578.

[51] Iida, Y., Ashokkumar, M., Tuziuti, T., Kozuka, T., Yasui, K., Towata, A., and Lee, J. (2010a). Bubble population phenomena in sonochemical reactor: I estimation of bubble size distribution and its number density with pulsed sonication–laser diffraction method. *Ultrasonics sonochemistry*, 17(2):473–479.

[52] Iida, Y., Ashokkumar, M., Tuziuti, T., Kozuka, T., Yasui, K., Towata, A., and Lee, J. (2010b). Bubble population phenomena in sonochemical reactor: Ii. estimation of bubble size distribution and its number density by simple coalescence model calculation. *Ultrasonics sonochemistry*, 17(2):480–486.

[53] Jiang, G. S. and Shu, C. W. (1995). Efficient implementation of weighted eno schemes. Technical report, DTIC Document.

[54] Jiang, G. S. and Shu, C.-W. (1996). Efficient implementation of weighted eno schemes. *J. Comput. Phys.*, 126(1):202–228.

[55] Johnsen, E. and Colonius, T. (2006). Implementation of weno schemes in compressible multi-component flow problems. *Journal of Computational Physics*, 219(2):715–732.

[56] Johnsen, E., Larsson, J., Bhagatwala, A. V., Cabot, W. H., Moin, P., Olson, B. J., Rawat, P. S., Shankar, S. K., Sjögreen, B., Yee, H., et al. (2010). Assessment of high-resolution methods for numerical simulations of compressible turbulence with shock waves. *Journal of Computational Physics*, 229(4):1213–1237.

[57] Jones, S. F., Evans, G. M., and Galvin, K. P. (1999). Bubble nucleation from gas cavities?a review. *Advances in colloid and interface science*, 80(1):27–50.

[58] Kalikmanov, V. I. (2013). Classical nucleation theory. In *Nucleation theory*, pages 17–41. Springer.

[59] Keller, J. B. and Miksis, M. (1980). Bubble oscillations of large amplitude. *The Journal of the Acoustical Society of America*, 68(2):628–633.

[60] Kwak, H. Y. and Lee, S. (1991). Homogeneous bubble nucleation predicted by a molecular interaction model. *Journal of heat transfer*, 113(3):714–721.

[61] Lauer, E., Hu, X., Hickel, S., and Adams, N. A. (2012a). Numerical investigation of collapsing cavity arrays. *Physics of Fluids*, 24(5):052104.

[62] Lauer, E., Hu, X. Y., Hickel, S., and Adams, N. A. (2012b). Numerical modelling and investigation of symmetric and asymmetric cavitation bubble dynamics. *Computers & Fluids*, 69:1–19.

[63] Lauterborn, W. and Kurz, T. (2010). Physics of bubble oscillations. *Reports on Progress in Physics*, 73(10):106501.

[64] Lee, J., Ashokkumar, M., Kentish, S., and Grieser, F. (2005). Determination of the size distribution of sonoluminescence bubbles in a pulsed acoustic field. *Journal of the American Chemical Society*, 127(48):16810–16811.

[65] LeVeque, R. J. (2002). *Finite volume methods for hyperbolic problems*, volume 31. Cambridge university press.

[66] Lezzi, A. and Prosperetti, A. (1987). Bubble dynamics in a compressible liquid. part 2. second-order theory. *Journal of Fluid Mechanics*, 185:289–321.

[67] Lohse, D. (2002). Sonoluminescence: Inside a micro-reactor. *Nature*, 418(6896):381.

[68] Loth, E. (2000). Numerical approaches for motion of dispersed particles, droplets and bubbles. *Progress in energy and combustion science*, 26(3):161–223.

[69] Lu, J., Fernández, A., and Tryggvason, G. (2005). The effect of bubbles on the wall drag in a turbulent channel flow. *Physics of Fluids*, 17(9):095102.

[70] Lyu, X., Pan, S., Hu, X., and Adams, N. A. (2018). Numerical investigation of homogeneous cavitation nucleation in a microchannel. *Physical Review Fluids*, 3(6):064303.

[71] Ma, J., Hsiao, C.-T., and Chahine, G. L. (2018). Numerical study of acoustically driven bubble cloud dynamics near a rigid wall. *Ultrasonics sonochemistry*, 40:944–954.

[72] Ma, J. S., Chahine, G. L., and Hsiao, C. T. (2015). Spherical bubble dynamics in a bubbly medium using an euler–lagrange model. *Chemical Engineering Science*, 128:64–81.

[73] Maeda, K. and Colonius, T. (2018). Eulerian-lagrangian method for simulation of cloud cavitation. *Journal of Computational Physics*, 371:994–2017.

[74] Matsumoto, Y., Allen, J. S., Yoshizawa, S., Ikeda, T., and Kaneko, Y. (2005). Medical ultrasound with microbubbles. *Experimental thermal and fluid science*, 29(3):255–265.

[75] Mihatsch, M. S., Schmidt, S. J., and Adams, N. A. (2015). Cavitation erosion prediction based on analysis of flow dynamics and impact load spectra. *Physics of Fluids*, 27(10):103302.

[76] Monaghan, J. J. (1982). Why particle methods work. *SIAM Journal on Scientific and Statistical Computing*, 3(4):422–433.

[77] Mudholkar, G. S. and Srivastava, D. K. (1993). Exponentiated weibull family for analyzing bathtub failure-rate data. *IEEE Transactions on Reliability*, 42(2):299–302.

[78] Nigmatulin, R., Khabeev, N., and Nagiev, F. (1981). Dynamics, heat and mass transfer of vapour-gas bubbles in a liquid. *International Journal of Heat and Mass Transfer*, 24(6):1033–1044.

[79] Ohl, C. D., Arora, M., Dijkink, R., Janve, V., and Lohse, D. (2006). Surface cleaning from laser-induced cavitation bubbles. *Applied physics letters*, 89(7):074102.

[80] Ohl, S. W., Klaseboer, E., and Khoo, B. C. (2015). Bubbles with shock waves and ultrasound: a review. *Interface Focus*, 5(5):20150019.

[81] Örley, F., Trummler, T., Hickel, S., Mihatsch, M., Schmidt, S., and Adams, N. (2015). Large-eddy simulation of cavitating nozzle flow and primary jet break-up. *Physics of Fluids*, 27(8):086101.

[82] O'Rourke, P. J. (1981). Collective drop effects on vaporizing liquid sprays. Technical report, Los Alamos National Lab., NM (USA).

[83] O'Rourke, P. J. (1985). The kiva computer program for multidimensional chemically reactive fluid flows with fuel sprays. In *Numerical Simulation of Combustion Phenomena*, pages 74–89. Springer.

[84] Osher, S. and Sethian, J. A. (1988). Fronts propagating with curvature-dependent speed: algorithms based on hamilton-jacobi formulations. *Journal of computational physics*, 79(1):12–49.

[85] Pirozzoli, S. (2011). Numerical methods for high-speed flows. *Annual Review of Fluid Mechanics*, 43:163–194.

[86] Plesset, M. S. (1949). The dynamics of cavitation bubbles. *Journal of applied mechanics*, 16:277–282.

[87] Price, D. J. (2012). Smoothed particle hydrodynamics and magnetohydrodynamics. *J. Comput. Phys.*, 231:759–794.

[88] Prosperetti, A. and Lezzi, A. (1986). Bubble dynamics in a compressible liquid. part 1. first-order theory. *Journal of Fluid Mechanics*, 168:457–478.

[89] Pruppacher, H. R., Klett, J. D., and Wang, P. K. (1998). Microphysics of clouds and precipitation.

[90] Qin, Z., Bremhorst, K., Alehossein, H., and Meyer, T. (2007). Simulation of cavitation bubbles in a convergent–divergent nozzle water jet. *Journal of Fluid Mechanics*, 573:1–25.

[91] Quinto-Su, P. A. and Ando, K. (2013). Nucleating bubble clouds with a pair of laser-induced shocks and bubbles. *Journal of Fluid Mechanics*, 733:R3.

[92] Quirk, J. J. and Karni, S. (1996). On the dynamics of a shock–bubble interaction. *Journal of Fluid Mechanics*, 318:129–163.

[93] Rayleigh, L. (1917). Viii. on the pressure developed in a liquid during the collapse of a spherical cavity. *The London, Edinburgh, and Dublin Philosophical Magazine and Journal of Science*, 34(200):94–98.

[94] Rider, W. J. (1999). An adaptive riemann solver using a two-shock approximation1. *Computers & fluids*, 28(6):741–777.

[95] Roe, P. L. (1981). Approximate riemann solvers, parameter vectors, and difference schemes. *Journal of computational physics*, 43(2):357–372.

[96] Saurel, R. and Abgrall, R. (1999). A multiphase godunov method for compressible multifluid and multiphase flows. *Journal of Computational Physics*, 150(2):425–467.

[97] Shen, V. K. and Debenedetti, P. G. (2001). Density-functional study of homogeneous bubble nucleation in the stretched lennard-jones fluid. *The Journal of Chemical Physics*, 114(9):4149–4159.

[98] Shen, V. K. and Debenedetti, P. G. (2003). A kinetic theory of homogeneous bubble nucleation. *The Journal of chemical physics*, 118(2):768–783.

[99] Shu, C.-W. (1988). Total-variation-diminishing time discretizations. *SIAM Journal on Scientific and Statistical Computing*, 9(6):1073–1084.

[100] Shu, C. W. and Osher, S. (1988). Efficient implementation of essentially non-oscillatory shock-capturing schemes. *Journal of Computational Physics*, 77(2):439–471.

[101] Shu, C. W. and Osher, S. (1989). Efficient implementation of essentially non-oscillatory shock-capturing schemes, ii. *J. Comput. Phys.*, 83:32–78.

[102] Singh, R. N. and Sharma, S. (2012). Development of suitable photobioreactor for algae production–a review. *Renewable and Sustainable Energy Reviews*, 16(4):2347–2353.

[103] Sridhar, G. and Katz, J. (1995). Drag and lift forces on microscopic bubbles entrained by a vortex. *Physics of Fluids*, 7(2):389–399.

[104] Stride, E. and Coussios, C. (2010). Cavitation and contrast: the use of bubbles in ultrasound imaging and therapy. *Proceedings of the Institution of Mechanical Engineers, Part H: Journal of Engineering in Medicine*, 224(2):171–191.

[105] Subramaniam, S. (2013). Lagrangian–eulerian methods for multiphase flows. *Progress in Energy and Combustion Science*, 39(2-3):215–245.

[106] Swegle, J. W., Hicks, D. L., and Attaway, S. W. (1995). Smoothed particle hydrodynamics stability analysis. *Monthly Notices of the Royal Astronomical Society*, 116:123–134.

[107] Thomas, P. A. and Couchman, H. M. P. (1992). Simulating the formation of a cluster of galaxies. *MNRAS*, 257:11?1.

[108] Tiwari, A., Pantano, C., and Freund, J. B. (2015). Growth-and-collapse dynamics of small bubble clusters near a wall. *Journal of Fluid Mechanics*, 775:1–23.

[109] Toro, E. F. (2013). *Riemann solvers and numerical methods for fluid dynamics: a practical introduction*. Springer Science & Business Media.

[110] Turnbull, D. and Fisher, J. C. (1949). Rate of nucleation in condensed systems. *The Journal of Chemical Physics*, 17(1):71–73.

[111] Vlaisavljevich, E., Lin, K. W., Warnez, M. T., Singh, R., Mancia, L., Putnam, A. J., Johnsen, E., Cain, C., and Xu, Z. (2015). Effects of tissue stiffness, ultrasound frequency, and pressure on histotripsy-induced cavitation bubble behavior. *Physics in medicine and biology*, 60(6):2271.

[112] Wang, Q. and Squires, K. D. (1996). Large eddy simulation of particle-laden turbulent channel flow. *Physics of Fluids*, 8(5):1207–1223.

[113] Wang, Z. J., Fidkowski, K., Abgrall, R., Bassi, F., Caraeni, D., Cary, A., Deconinck, H., Hartmann, R., Hillewaert, K., Huynh, H. T., et al. (2013). High-order cfd methods: current status and perspective. *International Journal for Numerical Methods in Fluids*, 72(8):811–845.

[114] Wilhelmsen, Ø., Bedeaux, D., Kjelstrup, S., and Reguera, D. (2014). Thermodynamic stability of nanosized multicomponent bubbles/droplets: The square gradient theory and the capillary approach. *The Journal of chemical physics*, 140(2):024704.

[115] Williams, F. A. (1958). Spray combustion and atomization. *The Physics of Fluids*, 1(6):541–545.

[116] Zhong, X. and Wang, X. (2012). Direct numerical simulation on the receptivity, instability, and transition of hypersonic boundary layers. *Annual Review of Fluid Mechanics*, 44:527–561.